

# **Influence of Low-speed Aerodynamic Performance on Airport Community Noise**

by

Andrew March

B.S. Mechanical Engineering  
Cornell University, 2005

SUBMITTED TO THE DEPARTMENT OF AERONAUTICS AND ASTRONAUTICS  
IN PARTIAL FULFILLMENT OF THE REQUIREMENTS FOR THE DEGREE OF

MASTER OF SCIENCE IN AERONAUTICS AND ASTRONAUTICS  
AT THE  
MASSACHUSETTS INSTITUTE OF TECHNOLOGY

MAY 2008

© 2008 Massachusetts Institute of Technology. All rights reserved.

The author hereby grants to MIT permission to reproduce  
and to distribute publicly paper and electronic  
copies of this thesis document in whole or in part.

Signature of Author.....  
Department of Aeronautics and Astronautics  
May 2008

Certified by.....  
Ian Waitz  
Jerome C. Hunsaker Professor and Department Head  
Aeronautics and Astronautics  
Thesis Supervisor

Certified by.....  
Karen Willcox  
Associate Professor of Aeronautics and Astronautics

Accepted by.....  
Prof. David L. Darmofal  
Associate Department Head  
Chair, Committee on Graduate Students



**Influence of Low-speed Aerodynamic Performance on Airport Community Noise**  
by  
Andrew March

Submitted to the Department of Aeronautics and Astronautics  
on May 23, 2008 in Partial Fulfillment of the  
Requirements for the Degree of Master of Science in  
Aeronautics and Astronautics  
At the Massachusetts Institute of Technology

**ABSTRACT**

Properly assessing proposed aviation policies requires a thorough trade study of noise, emissions, fuel consumption, and cost. Aircraft low-speed aerodynamic performance is an important driver of all these impacts, and this thesis presents the development of an aerodynamic tool capable of accurately estimating key low-speed performance characteristics using aircraft geometry information typical of that available in the preliminary phase of aircraft design. The goal of this thesis is to use the low-speed aerodynamic estimates to present the sensitivity of aircraft noise to aircraft configuration and operational procedures, and then to identify improved procedures to reduce the cost, fuel use, and noise of current aircraft.

The low-speed aerodynamic method developed in this work is comparable to aircraft manufacturer initial design tools. It requires about fifteen seconds on a modern computer and has been developed to a sufficient level of accuracy through a calibration study using Boeing flight test data, NASA wind tunnel results, and an empirically-tuned Lockheed method. The low-speed method is generally capable of predicting a drag polar, drag as a function of lift, to within one-percent. It also determines the changes of the drag polar due to high-lift devices, both slat and flap deployment, to within about three-percent. In addition, the method contains correlations to predict the variations of lift with angle of attack and the maximum lift coefficient; these predictions have errors around ten-percent and five-percent, respectively. The estimates produced by the method are of appropriate fidelity to properly model aircraft flight trajectories for fuel burn and noise estimates within larger environmental impact assessment models.

The results of simulations of the mandated takeoff and landing noise certification procedure show that noise is reduced insignificantly by small modifications to the airframe.

This is largely because, for the current aircraft fleet, engine noise dominates both takeoff and landing noise, and only methods to reduce the required thrust or increase the aircraft altitude will significantly decrease noise. For landing, significant reductions in noise, on the order of 1-2%, were found by increasing the approach speed, which decreases required thrust, and by steepening the approach path, which keeps the aircraft higher above the ground when outside the airport boundaries. The results of an optimization study estimating the Pareto Frontier of departure procedures for a 747-200 aircraft show that compared to the standard departure at maximum takeoff weight, a reduction in time to climb of two minutes, in fuel consumption of 1,300 lbm, and in land area exposed to a sound level 55 EPNdB of 100 square miles can be mutually achieved.

Thesis Supervisor:

Ian Waitz

Title:

Jerome C. Hunsaker Professor and Head of the  
Aeronautics and Astronautics Department

## **ACKNOWLEDGEMENTS**

There are many people that helped me with my research and I would like to thank them. Most importantly, I would like to thank my two advisors Professor Waitz and Professor Willcox. Without them none of this would have been possible. They are both the best advisors a graduate student could want, and I was privileged to have them both. Professor Waitz arranged my project and set me out on the right foot. He was always there for a nice pat on the back when I struggled or advice when I needed it. Prof. Willcox always went out of her way to make sure my research was going well, was my voice when I needed an agent, and was the reason I came to MIT.

Another member in our research group, Dr. Hileman was instrumental in my work on aircraft noise. Jim volunteered to help me and contributed immense of amounts of time to teach me about aircraft noise. He was always available to answer questions, to chat about work, and to suggest worthwhile analyses to supplement results. Jim never asked for anything more than turning on the coffee pot and was the motivation for our office happy hour.

There are many people in my lab that deserve special recognition as well. Anuja greatly helped me to prepare for the PhD program. Without her, quals would have been considerably worse and I probably would not have known where to begin. Dr. Stu Jacobson coordinated my work with Volpe and the FAA. He made sure I had the software I needed and would tell me who the proper point of contact was. He was always there for a smile when I went to the water fountain and would always share in my excitement when I made my code work. Chris Kish helped me with noise impacts and to validate my noise contour predictions. Phil Spindler gave me immeasurable amounts of computer help and was always available for questions even after he graduated. Chris Sequiera helped me when I got to MIT and did not know where anything was, and Elza was always there for a laugh about Montreal bagels. I also want to thank my officemate Pearl for putting up with my shenanigans for a year and just being a happy face in a dingy room. Tim, Julien, Doug, Tudor and Mina complimented the camaraderie in our office nicely.

The trajectory optimization study in this thesis could not have been done without the help of some people at Volpe: Eric Boeker, David Senzig, and Paul Gerbi, as well as Eric Dinges with ATAC. They were all essential to my ability to use the Integrated Noise Model for predictions, and a purpose for which it was never intended. Whether it was information about how the software worked, what the bit order was in a binary file, or source code, they were always extremely helpful. On the MIT side, Rhea Liem and Sonja Wogrin helped me to set up the optimization and debug the code as part of a class project for 16.888 Multidisciplinary System Design Optimization. They were a great help, and I am positive that this study would not have been completed without them.

I would like to thank my good friend and officemate, Bastien, and his wife and good friend Adeline. Bastien was there to help me with math when I needed it and to shoot rubber bands at me when I was stressed out doing work. He and Adeline were always available for a drink or a good chat. Also, Jim and Melissa were among the nicest people I have ever met. Jim would answer any request for food or a drink with Boolean algebra and Melissa would always drive us home. I will miss all four of you and know that we will stay in touch wherever in the world we end up.

Most importantly, I would like to thank my fiancée Michelle. She moved across the country for me twice and even agreed to drive six-thousand miles from LA to Boston, via Banff, to get to MIT. She always gave me my space when I had a lot of work to do, and came close when the work got to me. Whenever I needed an editor, or help with chores, or had to write a sensitive email, she was there. MIT would have been far more challenging without her.

I would finally like to thank the Federal Aviation Administration, the National Aeronautics and Space Administration, and Transport Canada for funding PARTNER. Their funds enable a great array of valuable research. Similarly, I would like to thank the National Science Foundation for my fellowship, which allowed me to attend graduate school.

# CONTENTS

<b>CHAPTER 1: INTRODUCTION.....</b>	<b>21</b>
1.1. PARTNER .....	22
1.2. LOW-SPEED AERODYNAMICS.....	23
1.3. NOISE.....	25
1.4. ORGANIZATION OF THE THESIS .....	28
<b>CHAPTER 2: MODELING FOR PERFORMANCE ESTIMATION.....</b>	<b>31</b>
2.1. AIRCRAFT PARAMETERIZATION .....	31
2.2. AIRFOIL PARAMETERIZATION .....	34
2.2.1. <i>Main Lifting Element</i> .....	34
2.2.2. <i>Tail Lifting Surfaces</i> .....	35
2.2.3. <i>Airfoil Parameter List</i> .....	35
<b>CHAPTER 3: LOW-SPEED AERODYNAMICS ESTIMATION METHOD.....</b>	<b>37</b>
3.1. HIGH-LEVEL OVERVIEW .....	37
3.2. CLEAN CONFIGURATION DRAG POLAR .....	39
3.2.1. <i>Profile Drag</i> .....	39
3.2.2. <i>Induced Drag</i> .....	43
3.2.3. <i>Excrescence Drag</i> .....	43
3.2.4. <i>Interference Drag</i> .....	44
3.2.5. <i>Off-Design Drag</i> .....	48
3.3. METHOD RESULTS – FLAPS UP .....	51
3.3.1. <i>777-200ER Comparison with Delta Drag Method</i> .....	56
3.4. DRAG POLARS FOR HIGH-LIFT DEVICES DEPLOYED .....	57
3.4.1. <i>Drag Components from Clean Configuration</i> .....	58
3.4.2. <i>Vortex Drag Term</i> .....	58
3.4.3. <i>Flap Profile Drag</i> .....	62
3.4.4. <i>Slat Drag</i> .....	63
3.4.5. <i>Landing Gear Deployment Drag</i> .....	64
3.5. METHOD RESULTS – FLAPS DEPLOYED.....	66
3.6. LIFT v ANGLE OF ATTACK AND $C_{LMAX}$ FOR CLEAN CONFIGURATION .....	68
3.7. LIFT v ANGLE OF ATTACK AND $C_{LMAX}$ PREDICTIONS FOR HIGH-LIFT DEVICES .....	71
3.7.1. <i><math>C_{Lmax}</math> Data for Current Aircraft</i> .....	71
3.7.2. <i>Computing <math>C_{Lmax}</math></i> .....	72
3.7.3. <i>Computing <math>\Delta C_{Lmax}</math> due to Trailing-Edge Flaps</i> .....	73
3.7.4. <i>Computing <math>\Delta C_{Lmax}</math> due to Leading-Edge Slats</i> .....	75
3.7.5. <i><math>C_{Lmax}</math> Prediction Results</i> .....	77
3.7.6. <i>Predicting <math>C_L</math> v Angle of Attack</i> .....	78
3.7.7. <i><math>C_L</math> v Angle of Attack Results</i> .....	80
3.8. METHOD LIMITATIONS/KNOWN ISSUES .....	82
<b>CHAPTER 4: TRAJECTORY MODELING .....</b>	<b>85</b>

4.1. METHODOLOGY--TAKEOFF .....	85
4.1.1. Engine Thrust Prediction.....	87
4.1.2. Takeoff Rotation.....	89
4.1.3. Takeoff Method Validation .....	90
4.1.4. Takeoff Method Results.....	92
4.2. METHODOLOGY--FLIGHT .....	93
4.3. VALIDATION, INM RESULTS .....	96
<b>CHAPTER 5: NOISE ESTIMATION .....</b>	<b>101</b>
5.1. AIRCRAFT NOISE ESTIMATION .....	101
5.2. PREDICTING GROUND LEVEL NOISE .....	107
<b>CHAPTER 6: NOISE SENSITIVITIES.....</b>	<b>109</b>
6.1. LOW-SPEED AERODYNAMIC SENSITIVITIES .....	109
6.2. DEPARTURE NOISE METHODOLOGY.....	110
6.3. DEPARTURE NOISE SENSITIVITIES.....	112
6.4. APPROACH NOISE METHODOLOGY .....	114
6.5. APPROACH NOISE SENSITIVITIES .....	115
<b>CHAPTER 7: TRAJECTORY OPTIMIZATION .....</b>	<b>119</b>
7.1. PROBLEM SETUP .....	120
7.2. OPTIMIZATION METHOD .....	122
7.3. RESULTS .....	124
7.4. MAINTENANCE COSTS.....	131
<b>CONCLUSION .....</b>	<b>135</b>
<b>APPENDIX A: AIRCRAFT GEOMETRIES .....</b>	<b>137</b>
A.1. NASA TN D-5971 [19] .....	137
A.2. BOEING 727-100 [62].....	138
A.3. BOEING 737-700 .....	139
A.4. BOEING 747-100 [62].....	140
A.5. NASA TP 1580 [37] .....	141
A.6. NACA L50F20 [63].....	142
A.7. NACA L8H20 [64].....	143
<b>REFERENCES.....</b>	<b>145</b>

## LIST OF FIGURES

FIGURE 2.1: WIREFRAME MODEL SHOWING THE APPROXIMATE DETAIL OF THE AIRCRAFT USED IN THE LOW-SPEED AERODYNAMIC MODEL.....	31
FIGURE 3.1 – PRESENTATION OF A FLOW CHART OF THE LOW-SPEED AERODYNAMICS METHODOLOGY, WHICH HAS BEEN COLOR CODED TO SHOW THE SOURCE OF THE METHOD. BLUE INDICATES WORK THAT IS PREDOMINANTLY CREATED IN THIS THESIS, GREEN INDICATES WORK THAT IS LARGELY FROM OTHER SOURCES, BUT MODIFIED TO FIT THIS FRAMEWORK, AND RED INDICATES A RESULT.....	38
FIGURE 3.2: FIGURE SHOWING THE RELATIVE MAGNITUDES OF THE DIFFERENT COMPONENTS OF DRAG FOR BOTH A CLEAN AND HIGH-LIFT CONFIGURATION USING THE LOW-SPEED AERODYNAMIC MODEL AND PUBLIC GEOMETRY FOR A BOEING 777-200.....	39
FIGURE 3.3 WIREFRAME SKETCH OF NASA TN D-5971 WIND TUNNEL MODEL [19].	42
FIGURE 3.4 WIREFRAME SKETCH OF A BOEING 737-700.....	42
FIGURE 3.5 EXCRESCENCE DRAG AS A FUNCTION OF AIRCRAFT TOTAL WETTED AREA AND A TECHNOLOGY FACTOR [22].	44
FIGURE 3.6 COMPARISON BETWEEN ORIGINAL ENGINE INTEGRATION SCHEMES AND COMPUTATIONALLY DERIVED INTEGRATION SCHEMES WITH SIMILAR INTERFERENCE DRAG [23].	45
FIGURE 3.7 SKETCH OF THE WING DOWNWASH GOING PAST THE TAIL OF THE FUSELAGE AND THE CAUSE OF UPSWEEP DRAG.	47
FIGURE 3.8 SCHEMATIC OF THE AFT FUSELAGE PLANFORM AREA USED TO COMPUTE FUSELAGE UPSWEEP DRAG, $S_p$ .	48
FIGURE 3.9 INCREMENTAL DRAG COEFFICIENT AS A FUNCTION OF $C_L-C_{LDESIGN}$ AND WING SWEEP.	49
FIGURE 3.10 THE EFFECT OF THE $\Delta C_D$ v $\Delta C_L$ CURVES WHEN APPLIED TO THE DRAG POLARS PREDICTED BY THE VORTEX LATTICE METHOD.	51
FIGURE 3.11 COMPARISON BETWEEN WIND TUNNEL RESULTS AND PREDICTIONS FOR THE MODEL OF NASA TN D-5971 [19].	53
FIGURE 3.12 COMPARISON BETWEEN BOEING 727-100 FLIGHT TEST DATA AND THE PREDICTIONS OF THE LOW-SPEED AERODYNAMICS MODEL.	53
FIGURE 3.13 COMPARISON BETWEEN BOEING 737-700 FLIGHT TEST RESULTS AND LOW-SPEED AERODYNAMICS METHOD PREDICTIONS.	54
FIGURE 3.14 COMPARISON OF BOEING 747-100 FLIGHT TEST DATA AND THE PREDICTIONS OF THE LOW-SPEED AERODYNAMICS PREDICTIONS.	54
FIGURE 3.15 COMPARISON OF NACA RM L50F20, 47.7° SWEEP WING AND THE PREDICTED DRAG POLAR. THE SHARP RISE OF THE DRAG PREDICTION IS CLEAR NEAR STALL, AND IT IS QUITE EVIDENT THAT IT IS NOT PHYSICAL REPRESENTATION OF STALL.	55
FIGURE 3.16 COMPARISON OF NACA RM L8H20, 51.3° SWEEP WING AND THE PREDICTED DRAG POLAR. AS IN FIGURE 3.15, THERE IS A SHARP DRAG RISE IN THE PREDICTED POLAR THAT IS AN UNPHYSICAL STALL REPRESENTATION.	55
FIGURE 3.17 COMPARISON OF THE PREDICTED DRAG POLAR AND THE DRAG POLAR PREDICTED BY THE DELTA DRAG METHOD [7] FOR THE BOEING 777-200ER AT MACH 0.3 AND 10,000FT ALTITUDE BASED ON PUBLICLY AVAILABLE GEOMETRY.	57
FIGURE 3.18 GEOMETRIC DEFINITIONS FOR FUSELAGE INTERFERENCE EFFECTS ON FLAPS.	59

FIGURE 3.19: FLAP EFFECTIVENESS EMPIRICAL FUNCTION FOR DOUBLE-SLOTTED FLAPS FROM TORENBEEK [9].	61
FIGURE 3.20: RAW $C_{D_{FLAP}}$ TO BE USED IN EQUATION 3.20.	62
FIGURE 3.21: SAMPLE CURVE OF $C_{D_{FLAP}}$ v FLAP DEFLECTION FOR AN AIRCRAFT WITH $30^{\circ}$ OF SWEEP AND A FLAP CHORD FRACTION OF 0.25. COMPARED TO RESULTS FROM SCHAUFELLE [10] AND ESDU [32],[34].	63
FIGURE 3.22: LANDING GEAR DRAG COEFFICIENT PREDICTION [10].	65
FIGURE 3.23 PREDICTED DRAG POLARS FOR THE 727-100 FOR 5 DIFFERENT FLAP SETTINGS. LINES REPRESENT FLIGHT TEST DATA AND OVERLAID ASTERISKS REPRESENT THE PREDICTIONS...	66
FIGURE 3.24 PREDICTED DRAG POLARS FOR THE 737-700 FOR 5 DIFFERENT FLAP SETTINGS. LINES REPRESENT FLIGHT TEST DATA AND OVERLAID ASTERISKS REPRESENT THE PREDICTIONS...	67
FIGURE 3.25 PREDICTED DRAG POLARS FOR THE 747-100 FOR 3 DIFFERENT FLAP SETTINGS. LINES REPRESENT FLIGHT TEST DATA AND OVERLAID ASTERISKS REPRESENT THE PREDICTIONS...	67
FIGURE 3.26 PREDICTED DRAG POLARS FOR NASA TM-1580, A SUBSONIC COMMERCIAL TRANSPORT WIND TUNNEL MODEL. LINES REPRESENT THE WIND TUNNEL TEST DATA AND OVERLAID ASTERISKS REPRESENT THE PREDICTIONS [37].	68
FIGURE 3.27: SCHAUFELLE'S METHOD OF PREDICTING $C_{L_{MAX}}$ FOR A CLEAN WING. LEFT, $C_{L_{MAX-TIP}}$ AS A FUNCTION OF WINGTIP THICKNESS TO CHORD RATIO, CENTER, RATIO OF AIRPLANE $C_{L_{MAX}}$ TO $C_{L_{MAX-TIP}}$ AS A FUNCTION OF WING SWEEP, AND RIGHT, THE RATIO OF $C_{L_{MAX}}$ TO $C_{L_{MAX-LOW-SPEED}}$ AS A FUNCTION OF MACH NUMBER [10].	69
FIGURE 3.28: COMPARISON OF THE PREDICTED LIFT CURVE FOR THE 737-700 AND FLIGHT TEST DATA AT LOW SPEED.	70
FIGURE 3.29: COMPARISON OF THE PREDICTED LIFT CURVE AND WIND TUNNEL DATA FOR A NASA MODEL AT $M=0.55$ [19].	71
FIGURE 3.30: EMPIRICAL FUNCTION FOR $K_{T1}$ USED IN PREDICTING THE ADDITIONAL MAXIMUM LIFT OF A TRAILING EDGE FLAP.	74
FIGURE 3.31: EMPIRICAL FUNCTION OF THE SLAT DEFLECTION ANGLE FOR THE PARAMETER $K_L$ MODIFIED FROM REFERENCE [31].	76
FIGURE 3.32: COMPARISON BETWEEN PREDICTED MAXIMUM LIFT COEFFICIENT AND THE MAXIMUM LIFT COEFFICIENT CONTAINED IN THE INTEGRATED NOISE MODEL FOR THE BOEING 737-700.	77
FIGURE 3.33: PLOT SHOWING THE PERCENT ERROR FOR THE MAXIMUM LIFT COEFFICIENT PREDICTIONS FOR MANY COMMERCIAL AIRCRAFT CONFIGURATIONS AS A FUNCTION OF FLAP DEFLECTION ANGLE.	78
FIGURE 3.34: COMPARISON OF THE PREDICTED LIFT CURVE AND FLIGHT TEST DATA FOR THE 737-700 IN BOTH THE TAKEOFF AND LANDING CONFIGURATION.	81
FIGURE 3.35: COMPARISON OF THE PREDICTED LIFT CURVE AND WIND TUNNEL DATA FOR THE MODEL OF NASA TP-1580 IN BOTH THE TAKEOFF AND LANDING CONFIGURATION.	81
FIGURE 4.1: FORCES USED FOR TAKEOFF SIMULATION.	86
FIGURE 4.2: GROUND EFFECT, RATIO OF INDUCED DRAG IN GROUND EFFECT TO FAR-FIELD INDUCED DRAG. THE ABCISSA, $h/B$ , IS THE HEIGHT OF THE WING ABOVE THE GROUND PLANE DIVIDED BY THE WING SPAN [26].	87
FIGURE 4.3: COMPARISON OF ESTIMATED FAR25 RUNWAY LENGTH REQUIREMENT FOR THE BOEING 777-200 WITH THE GE90-90B ENGINE AND VALUES PUBLISHED BY BOEING. THE RED ASTERISKS ARE THE ESTIMATES AND THE BLUE LINES ARE THE PUBLISHED DATA [51].	92

FIGURE 4.4: COMPARISON OF ESTIMATED FAR25 RUNWAY LENGTH REQUIREMENT FOR THE BOEING 747-100 WITH THE GE90-90B ENGINE AND VALUES PUBLISHED BY BOEING. THE RED ASTERISKS ARE THE ESTIMATES AND THE BLUE LINES ARE THE PUBLISHED DATA [52].	93
FIGURE 4.5: FREE-BODY DIAGRAM OF AN AIRCRAFT IN FLIGHT.....	94
FIGURE 4.6: COMPARISON OF THE TRAJECTORY COMPUTED WITH THE FULL SIMULATION AND THE LINEAR MODEL COMPARED TO THE DATA CONTAINED IN THE INM FOR THE BOEING 777-200. ....	98
FIGURE 4.7: COMPARISON OF THE FULL AND LINEAR SIMULATION METHOD AND THE TRAJECTORY DATA FOR THE BOEING 747-200 CONTAINED IN THE INM. ....	98
FIGURE 5.1: DEPARTURE NOISE-POWER-DISTANCE CURVE FOR THE BOEING 777-200 WITH GE90-90B ENGINES. THRUST LEVEL IS CORRECTED THE NET THRUST PER ENGINE, SO THE TOTAL THRUST WILL ACTUALLY BE TWICE THE NUMBER SHOWN AS THE 777 HAS TWO ENGINES. ....	102
FIGURE 5.2: COMPARISON OF THE ATMOSPHERIC ABSORPTION OF NOISE FROM SAE-AIR-1845 AND FAR A36 [53], [60]. ....	104
FIGURE 5.3: COMPARISON OF TAKEOFF AIRFRAME NPD PREDICTION FROM ANOPP AND THE TAKEOFF NPD WITH 31,000 LBF OF THRUST PER ENGINE CONTAINED IN THE INM. THE MAXIMUM A-WEIGHTED SOUND EXPOSURE, $L_A$ MAX IS SHOWN IN BLUE, AND THE SOUND EXPOSURE LEVEL, SEL, IS SHOWN IN RED. THE AIRCRAFT CONFIGURATION FOR THE BOEING 777-200 IS SLATS TAKEOFF, AND FLAPS FIVE-DEGREES.....	105
FIGURE 5.4: COMPARISON OF TAKEOFF AIRFRAME NPD PREDICTION FROM ANOPP AND THE LANDING NPD WITH 12,000 LBF OF THRUST PER ENGINE CONTAINED IN THE INM. THE MAXIMUM A-WEIGHTED SOUND EXPOSURE, $L_A$ MAX IS SHOWN IN BLUE, AND THE SOUND EXPOSURE LEVEL, SEL, IS SHOWN IN RED. THE AIRCRAFT CONFIGURATION FOR THE BOEING 777-200 IS SLATS LANDING, FLAPS THIRTY-DEGREES, AND LANDING GEAR DEPLOYED. ....	106
FIGURE 6.1: SCHEMATIC SHOWING THE TAKEOFF NOISE CERTIFICATION POINTS.....	111
FIGURE 6.2: ESTIMATES OF FLYOVER AND SIDELINE NOISE FOR THE BOEING 777-200 WITH VARIOUS CUTBACK ALTITUDES, AND A COMPARISON TO THE ACTUAL CERTIFICATION NOISE VALUES. ....	112
FIGURE 6.3: TORNADO PLOT OF TAKEOFF NOISE SENSITIVITIES. AN IMPORTANT NOTE IS THAT THE MACH NUMBER IN THE FIGURE IS NOT THE MACH NUMBER FLOWN, IT IS THE MACH NUMBER AT WHICH THE DRAG POLAR WAS COMPUTED. ....	113
FIGURE 6.4: SCHEMATIC OF APPROACH NOISE CERTIFICATION POINT.....	114
FIGURE 6.5: TORNADO PLOT OF APPROACH NOISE SENSITIVITIES. NOTE: MACH NUMBER IN THE SENSITIVITY IS THE MACH NUMBER AT WHICH THE DRAG POLAR IS COMPUTED AND NOT THE MACH NUMBER AT WHICH THE APPROACH IS FLOWN. ....	115
FIGURE 6.6: CHANGES IN APPROACH NOISE DUE TO INCREASING THE APPROACH SPEED. ....	117
FIGURE 7.1: TYPICAL OPERATIONAL COST BREAKDOWN FOR A BOEING 747-200 USED FOR PASSENGER SERVICE IN 2006, AND THE PROJECTED COST BREAKDOWN FOR 2008 [65]. ....	120
FIGURE 7.2: SCHEMATIC SHOWING DIVISIONS OF THE DEPARTURE TRAJECTORY ENABLING THE PARAMETERIZATION OF THE TRAJECTORY FOR OPTIMIZATION. ....	122
FIGURE 7.3: PLOTS COMPARING THE TRAJECTORIES FOR MINIMUM TIME TO CLIMB, MINIMUM FUEL BURN, AND MINIMUM NOISE FOR A 747-200 WITH A TAKEOFF WEIGHT OF 725,000 LBM. ..	127
FIGURE 7.4: PLOTS OF THE NOISE CONTOURS FOR EACH OF THE TRAJECTORIES CORRESPONDING TO MINIMUM TIME TO CLIMB, MINIMUM FUEL BURN, AND MINIMUM NOISE. THE CONTOUR BANDS CORRESPOND TO 55, 60, 65, 70, 75, 80, AND 85 EPNDB.....	128

FIGURE 7.5: PLOTS SHOWING THE TRAJECTORIES FOR MINIMUM TIME TO CLIMB, MINIMUM FUEL BURN, AND MINIMUM NOISE EXPOSURE AREA FOR A BOEING 747-200 WITH A TAKEOFF WEIGHT OF 550,000 LBM..... 130

FIGURE 7.6: ESTIMATED CHANGE IN TURBINE INLET TEMPERATURE CAUSED BY REDUCING THE TAKEOFF POWER FOR THE JT9D-7A ENGINE FOR HOT-DAY SEA-LEVEL STATIC CONDITIONS [67]..... 132

## LIST OF TABLES

TABLE 2.1 WING GEOMETRIC PARAMETER LIST. ....	32
TABLE 2.2 FLAP AND SLAT GEOMETRIC PARAMETER LIST. ....	32
TABLE 2.3 FUSELAGE GEOMETRIC PARAMETER LIST. ....	33
TABLE 2.4 HORIZONTAL TAIL GEOMETRIC PARAMETER LIST. ....	33
TABLE 2.5 VERTICAL TAIL GEOMETRIC PARAMETER LIST. ....	33
TABLE 2.6 AIRCRAFT ENGINE GEOMETRIC PARAMETER LIST. ....	33
TABLE 2.7 OTHER LOW-SPEED AERODYNAMIC MODEL PARAMETERS. ....	34
TABLE 2.8 NACA 6-SERIES AIRFOIL, PARAMETER DEFINITION [17]. ....	34
TABLE 2.9 AIRFOIL PARAMETER LIST. ....	35
TABLE 3.1 PROFILE DRAG COMPARISON BETWEEN WIND TUNNEL MEASUREMENTS AND "FRICTION.F" FOR THE MODEL IN NASA TN D-5971 [19]. ....	42
TABLE 3.2 PROFILE DRAG COMPARISON BETWEEN METHOD IN SHEVELL AND "FRICTION.F". ....	43
TABLE 3.3 WING QUARTER-CHORD SWEEP ANGLE FOR TEST CASE AIRCRAFT. ....	49
TABLE 3.4: COMPARISON BETWEEN PUBLISHED VALUES OF $C_{LSTALL}$ AND THE $C_{LMAX}$ VALUES COMPUTED FROM THE INTEGRATED NOISE MODEL DATABASE IN THE LANDING CONFIGURATION FOR VARIOUS BOEING AIRPLANES [38]. ....	72
TABLE 3.5: 777-200ER FLAP DETENTS AND BOUNDS ON CORRESPONDING FLAP DEFLECTION ANGLES [42]. ....	83
TABLE 3.6: 737-400 FLAP DETENTS AND BOUNDS ON FLAP DEFLECTION ANGLES [43]. ....	83
TABLE 4.1: DEFINITION OF PARAMETERS IN INM THRUST LAPSE MODEL [45]. ....	88
TABLE 4.2: SAMPLE REGRESSION COEFFICIENTS FOR USE IN INM THRUST LAPSE MODEL FOR GE90-90B ENGINE. ....	88
TABLE 4.3: DETAILED CLIMB PROCEDURES FOR BOEING 777-200 AND BOEING 747-200 AIRCRAFT AT MAXIMUM TAKEOFF WEIGHT CONTAINED IN THE INM. ....	97
TABLE 4.4: COMPARISON OF TOTAL HORIZONTAL DISTANCE COVERED WHEN THE AIRCRAFT REACHES 10,000' FOR THE BOEING 777-200. THE PERCENT DIFFERENCE BETWEEN THE LINEAR MODEL AND THE FULL SIMULATION IS 8.07%. ....	99
TABLE 4.5: COMPARISON OF TOTAL HORIZONTAL DISTANCE COVERED WHEN THE AIRCRAFT REACHES 10,000' FOR THE BOEING 747-200. THE PERCENT DIFFERENCE BETWEEN THE LINEAR MODEL AND THE FULL SIMULATION IS 3.76%. ....	99
TABLE 6.1: COMPARISON OF 777-200 CERTIFICATION NOISE AND ESTIMATES FROM THE NOISE PREDICTION METHODOLOGY [61]. ....	112
TABLE 7.1: INM STANDARD DEPARTURE FOR BOEING 747-200 FIGURES OF MERIT. ....	124
TABLE 7.2: POINTS ALONG THE PARETO FRONT FOR BOEING 747-200 DEPARTURE TRAJECTORIES WITH A TAKEOFF WEIGHT OF 725,000 LBM. POINTS IN BOLD REPRESENT THE ANCHOR POINTS OF THE TRAJECTORIES. ....	125
TABLE 7.3: PARETO FRONT FOR TAKEOFF DEPARTURES OF A BOEING 747-200 WITH A TAKEOFF WEIGHT OF 550,000 LBM, POINTS IN BOLD REPRESENT THE ANCHOR POINTS. ....	129
TABLE 7.4: RESULTS OF FLYING THE SAME DEPARTURE PROCEDURE WITH AN AIRCRAFT OF DIFFERENT TAKEOFF WEIGHTS. ....	130
TABLE 7.5: RESULTS PREDICTING THE OBJECTIVE FUNCTION VALUES AT ANOTHER TAKEOFF WEIGHT USING A LINEAR APPROXIMATION. ....	131
TABLE 7.6: ESTIMATED OPTIMAL DE-RATE FOR DIFFERENT AIRCRAFT FLIGHT LENGTHS AND FUEL PRICES. ....	133



## NOMENCLATURE

### *Constants*

$g$	gravitational constant	$= 32.174 \text{ ft/s}^2$
$\gamma$	ratio of specific heats	$= 1.4$

### *General Variables*

$a$	lift curve slope, or acceleration
$b$	span
$AR$	aspect ratio
$C^*$	Chapman-Rebesin constant
$C_D$	total drag coefficient
$C_{Dp}$	profile drag
$C_{De}$	excrescence drag
$C_{Dflap}$	flap profile drag
$C_{Dgear}$	landing gear drag
$C_{Dind}$	induced drag
$C_{Dint}$	interference drag
$C_{Dslat}$	slat drag
$C_F$	skin friction coefficient
$C_L$	lift coefficient
$C_{Ldesign}$	aircraft design lift coefficient
$C_{Lmax}$	maximum lift coefficient
$C_{Lstall}$	lift coefficient at stall
$C_{L^*}$	lift coefficient at which nonlinear effects begin
$c$	chord
$c'$	effective chord
$c_{ds}$	empirical function of fuselage geometry used to compute upsweep drag
$D$	drag or fuselage diameter
$d$	diameter
$E$	engine thrust data regression coefficient
$F$	engine thrust data regression coefficient, or endurance
$FF$	form factor
$F_g$	ground force
$F_r$	rolling friction force
$G$	empirical function for upsweep drag,
$G_A$	engine thrust data regression coefficient
$G_B$	engine thrust data regression coefficient
$H$	empirical correction for downwash relative to aft-fuselage
$H_C$	engine thrust data regression coefficient
$h$	height of wing above fuselage centerline or altitude
$J_p$	empirical trailing edge additional lift factor
$K$	empirical factor to compute flap vortex drag
$K_s$	empirical function of leading edge device deflection angle
$K_l$	empirical function of leading edge device deflection angle
$K_{t1}$	empirical function of trailing edge flap deflection angle

$K_\delta$	empirical function of flap deflection angle
$k$	factor accounting for non-circular fuselage profile
$L, l$	reference length, body length
$M$	Mach number
$N$	empirical function of Reynolds number
$Pr$	Prandtl number
$r$	recovery factor
$R$	range
$Re$	Reynolds number
$S, S_{ref}$	planform area
$S_w$	wetted area
$S_p$	upswept fuselage planform area
$T$	thrust
$T_c$	temperature at the airplane
$T_e$	boundary layer edge temperature
$T_{t4}$	turbine inlet temperature
$t$	time
$V$	velocity
$V_{EF}$	takeoff balanced field speed
$V_r$	takeoff rotation speed
$V_s$	stall speed
$V_1$	takeoff reference speed, engine out decision speed
$V_2$	takeoff reference speed, minimum controllable airspeed
$W$	fuselage width or airplane weight
$W_{inc}$	wing angle of incidence at fuselage
$Y1$	span fraction of the start of the inboard flap
$y$	distance between top of nacelle and bottom of wing

### *Symbols*

$\alpha$	aircraft angle of attack
$\alpha^*$	aircraft angle of attack at which nonlinear effects start
$\beta$	fuselage upsweep angle
$\gamma$	flight path angle
$\Delta$	change in
$\Delta C_D$	off-design drag
$\Delta C_{L0}$	additional lift at zero angle of attack due to flap deployment
$\Delta s$	fictitious span change for flap fuselage interference
$\delta$	flap or slat deflection angle or the ambient pressure ratio
$\delta_0$	empirical function of flap deflection angle
$\varepsilon$	downwash angle
$\eta$	efficiency
$\theta$	ambient temperature ratio
$\Lambda$	sweep angle
$\mu$	viscosity or friction coefficient
$\mu_p$	empirical function of taper ratio

$\rho$	density
$\tau$	thickness
$\Phi$	empirical function of flap span
$\Psi$	empirical function of slat span

*Subscripts*

clean	flaps up and slats up
D	drag
f	flap
i	inboard, relating to flaps or slats
L	lift
n	net
o	outboard, relating to flaps or slats
le	leading edge
tip	wingtip
te	trailing edge
x	horizontal direction
y	vertical direction
0.25c	quarter chord
2D	for the airfoil, two dimensional flow field



## List of Acronyms

AC – Advisory Circular  
AGL – Above Ground Level  
ANOPP – Aircraft Noise Prediction Program  
APMT – Aviation Environmental Portfolio Management Tool  
AVL – Athena Vortex Lattice  
BWB – Blended-Wing-Body  
CAROC – Cash Airplane Related Operating Costs  
CFD – Computational Fluid Dynamics  
EDS – Environmental Design Space  
EPNL – Effective Perceived Noise Level  
ESDU – Engineering Sciences Data Unit  
FAA – Federal Aviation Administration  
FAR – Federal Aviation Regulation  
GA – Genetic Algorithm  
ICAO – International Civil Aviation Organization  
INM – Integrated Noise Model  
 $L_A$ Max – Maximum A-weighted Sound Exposure  
MIT – Massachusetts Institute of Technology  
NPD – Noise Power Distance Curve  
NACA – National Advisory Council for Aeronautics  
NASA – National Aeronautics and Space Administration  
PARTNER – Partnership for AiR Transportation Noise and Emissions Reduction  
PASS – Program for Aircraft Synthesis Studies  
PNLTM – Maximum Tone Corrected Perceived Noise Level  
PSO – Particle Swarming Optimization  
SAE – Society of Automotive Engineers  
SAI – Silent Aircraft Initiative  
SEL – Sound Exposure Level  
SFC – Specific fuel consumption  
SQP – Sequential Quadratic Programming  
VOLPE – Volpe National Transportation Systems Center, United States Department of Transportation



## CHAPTER 1: Introduction

On February 27<sup>th</sup> 2008 protestors scaled the roof of the British Houses of Parliament, hung banners and threw paper airplanes. On April 14<sup>th</sup> 2008 they staged a repeat performance at the Scottish Parliament. The protests were against the expansion of Heathrow airport because of the aircraft noise. These instances of aircraft noise protests are not isolated and occur whenever an airport tries to change flight paths or increase capacity. Why would protestors go to such lengths to protest a policy change that has such positive impacts on travel and commerce? This is because aviation noise is a disruptive nuisance. Defining annoyance as a feeling of resentment, displeasure, discomfort, dissatisfaction or offense which occurs when an environmental factor interferes with a person's thoughts, feelings or activities, studies have shown that aviation noise is more annoying to its surrounding community than other transportation noise sources even when they are at the same level [1].

Further, there are considerable health and welfare impacts from aviation noise. It has been shown to cause hypertension, ischaemic heart disease, sleep disturbance, and poor school performance. The studies showing the causation of disease and school performance are corrected for the socio-economic variations typical of airport communities. Aviation noise has also been linked to hormonal changes, deterioration of the immune system, decreased birth weight, psychiatric disorders, negative effects on psycho-social well-being, and decreased general performance [1]. Exposure to aviation noise is quite widespread; there are over 10,000 commercial airports in the world with large populations surrounding them. As a point of reference, within only the states of New York, New Jersey, and Philadelphia, over 1.3 million people are exposed to a Day-Night-Level of 55 dB [2]. This means aviation noise affects people of all socio-economic groups in ways that can have significant impacts on their health, well-being, and happiness.

On the other hand, commercial aircraft have been getting quieter, and in the United States, even with increased air traffic, there has been a 95% reduction in the number of people exposed to aircraft noise compared to thirty-five years ago [3]. However, the technological improvement for reducing noise has slowed and further noise reductions will cause an increase in fuel burn and operating costs [4]. For example, modifications late in the design process for

the Airbus A380 produced a 1-2dB noise reduction but at an estimated fuel burn increase of 1-2% [5]. It is also projected that the trend of decreasing noise exposure rates will end shortly as most of the louder aircraft, certified in the 1970s are largely retired [4].

With the detrimental effects of aviation noise and the financial benefit to aircraft operators for flying so fuel burn and not noise is minimized, it has been necessary to impose regulations mandating noise certification standards. A challenge in assessing further increases in noise certification stringency is that current aircraft have a service life of about thirty years [4], so changes occur slowly and are thus subject to uncertainties in future market conditions. Another challenge is that reducing noise may increase other pollutants and cause other environmental impacts. For instance, increasing fuel burn means increased carbon dioxide emissions, which adds to global warming and climate change, and more particulate matter, which degrades air quality. Accordingly, there are numerous interdependencies among aviation impacts, so reducing one harmful effect of aviation could produce other more harmful effects.

### **1.1. PARTNER**

In the light of the interaction of aviation impacts, the Federal Aviation Administration (FAA), Transport Canada, and National Aeronautics and Space Administration (NASA) have been working with researchers from the Partnership for AiR Transportation Noise and Emissions Reduction (PARTNER) and others to develop a suite of tools to analyze, in an integrated way, the important environmental and financial impacts of aviation policies. The goal is to determine what the best course of action should be for aviation policy makers. Two of the tools PARTNER is leading the development of are the Aviation Environmental Portfolio Management Tool (APMT) and the Environmental Design Space (EDS). APMT is the scenario analysis tool which uses estimates of the aircraft environmental impacts, operating costs, and purchase prices to determine the future makeup of the United States or world aircraft fleet and the environmental and the financial prognosis of the industry over time. The EDS is an aircraft technology analysis tool that estimates aircraft performance, environmental impact, operating costs and purchase price.

EDS is a framework to perform aircraft system level trades and technology forecasting. In order to assess these trades EDS integrates a collection of NASA simulation modules, for instance, an engine performance prediction module, a noise estimation module, and a flight simulation module. The flight simulation module simulates an entire aircraft mission from taxi-out, through takeoff, climb, cruise, descent, landing, and taxi-in, and includes aircraft performance estimates for the cruise segment. However, the simulation module does not estimate the aircraft performance changes for when flaps and slats are deployed so a separate method is required to do that [6]. In early versions of EDS this method was to interpolate and scale performance data obtained for general commercial aircraft configurations from NASA and the FAA. This low-fidelity method to estimate low-speed performance caused EDS to have some poor results.

## **1.2. Low-Speed Aerodynamics**

An essential aspect of aircraft performance is low-speed aerodynamics, which determines all of the aircraft's flight characteristics near the ground where noise and local air quality are directly impacted. Low-speed aerodynamics are frequently characterized with two parameters: lift-to-drag ratio and maximum lift coefficient. The former determines the thrust required and fuel burn to meet a climb gradient. The latter determines the approach speed, a driver of approach noise, as well as the takeoff and landing field length, which in turn determines the airports an airplane can use. EDS needs to have the same level of accuracy as an aircraft manufacturer's conceptual design tool. With this level of accuracy, EDS will be capable of simulating the trade studies conducted while an aircraft manufacturer decides to produce a new product.

The low-speed aerodynamic estimation tool has similar prediction capabilities as a collection of previously existing tools. A Lockheed drag build-up scheme called the Delta Method has been shown to estimate incompressible (compressible if more configuration information is known) cruise configuration aircraft drag polars [7]. The Delta Method has a limitation imposed because it is calibrated for all types of aircraft; for instance, it is capable of predicting drag polars for commercial aircraft and supersonic fighter configurations. With the generality of configuration capabilities, the method only accurately predicts the drag polar near the cruise

lift coefficient, for instance near  $C_L=0.5$  for commercial aircraft. Otherwise, near the maximum lift coefficient or at low lift coefficients the Delta Method under predicts drag by up to 18%. The main reason this method cannot be used in EDS is that it cannot estimate drag polars for aircraft high-lift configurations, or the full lift-curve, lift as a function of angle of attack. Both of these missing components are essential for the aircraft low-speed aerodynamic estimates. Another aerodynamic prediction tailored exclusively for commercial transonic aircraft configurations, like those studied in EDS, was developed by Paterson [8]. This method is also missing the high-lift drag polar and lift-curve capabilities; however, the drag prediction methods are quite similar to what is currently used in aircraft preliminary design. The problem with the method is its age. When produced in 1973 the accuracy was very good; however, many components of the method, such as the engine interference drag, show their age because the engines considered all have a bypass ratio of zero. The current commercial fleet is predominantly high-bypass ratio engines, with bypass ratios generally between five and ten.

One of the most modern publicly available drag build-up methods is in Torenbeek [9]. The method has drag polar build-up methods for both cruise configuration and high-lift configurations and computes the change in the lift-curve caused by flap-deployment. The methods in Torenbeek are purely empirical, with some exceptions for simple flap theory, and there is limited information for cruise configuration lift-curves. A good reference for lift-curve prediction is contained in Schaufele [10]. Schaufele gives a simple method to estimate lift-curves for both the clean and high-lift configurations, as well as to predict the maximum lift coefficient.

The method presented in this thesis is largely an integration of the methods discussed previously. The main differences are that the induced drag prediction uses a full vortex-lattice method, many of the components have been updated and improved relative to the methods developed in last twenty years, there are some new empirical corrections added to improve predictions, and there is a significant amount of validation done on the estimates. The vortex-lattice method enables considerable improvement in the estimates of induced drag when compared with either Torenbeek's [9] or Schaufele's [10] empirical fits. This improves the prediction of both the drag polar and the lift-curves. The methods updated over the past twenty

years largely come from the Engineering Sciences Data Unit (ESDU) and improve the excrescence and upsweep drag predictions, as well as characteristics of the flaps and slats. The ESDU methods contain data on considerably more modern aircraft and enable a much better prediction of the current commercial fleet. An empirical correction that is unique to this method is the additive drag which is caused by flying at other than the wing's design lift coefficient. This enables a more accurate prediction of the drag at low lift coefficients and near the maximum lift coefficients. The true improvement of this method over the existing work discussed is the level of validation. The method has been compared against a collection of NASA wind tunnel results, proprietary Boeing flight test results, the maximum lift information contained in the FAA's Integrated Noise Model, and the previous methods discussed herein. The estimates of the low-speed aerodynamic model are at least as good as all of the methods discussed and are at the same level of accuracy as manufacturer initial design tools.

### **1.3. Noise**

The goal of this thesis is to determine the influence of low-speed aerodynamic performance on noise and to suggest ways that aircraft noise can be mitigated within the current aircraft fleet. A multidisciplinary study by Antoine, Kroo, Willcox and Barter [5] used a multi-objective genetic algorithm to optimize aircraft designs for minimum cost, fuel burn, noise, and nitrogen oxide emissions. The study showed the minimum noise aircraft has a larger wing planform area, considerably higher aspect ratio, considerably less wing sweep, larger horizontal tail area, and larger, more powerful engines with a higher bypass ratio than the minimum cost aircraft. This study used the Program for Aircraft Synthesis Studies, PASS, for low-speed aerodynamics. The basis of PASS is a vortex-lattice code, as with the low-speed estimates of low-speed prediction method discussed herein; however, the level of validation done on the empirical predictions of high-lift and maximum lift coefficients is unknown. The major difference between this work and the work herein is that the Antoine, Kroo, Willcox and Barter study attempted to find the global optimum aircraft configuration for aircraft cost and noise. This study attempts to determine the local sensitivity of noise to an aircraft's configuration, representative of small changes to the current fleet that can reduce noise. The results of the two

studies will be qualitatively compared to show consistency of the trends of aircraft configuration on reduced noise.

There is a collection of papers from the Silent Aircraft Initiative (SAI) that aimed to design an airplane capable of producing an imperceptible level of noise outside of an airport boundary [11]-[13]. The SAI uses a blended-wing-body (BWB) configuration so the aircraft are quite different from the traditional tube and wing aircraft studied in this thesis. The aerodynamic predictions use Athena Vortex Lattice, which is the same vortex lattice code used in the low-speed estimates in the analysis herein. The remaining predictions for maximum lift coefficient and flap and slat deflection are considerably different, necessarily so because of the BWB configurations. For a BWB the maximum lift coefficient is affected by dominating three-dimensional flow effects around the center body, and the airfoil shapes of the BWB must change because of pitching moments and stability. Whereas, for the tube and wing, maximum lift coefficient is mostly affected by the wingtip airfoils and the main lifting surface geometry does not have to change because the horizontal tail can overcome pitching moment variations. The BWB configuration completely changes the noise methodology used as well. With the considerably better aerodynamic performance, the takeoff noise optimization done by the SAI is largely to minimize the jet noise and not to vary the aerodynamic configuration. Similarly, for landing, the optimization is to vary the approach path and not the airframe. The difference between these publications and the analysis in this thesis is that in this thesis the aerodynamic configuration is varied whereas in the publications the engine placement is varied. Also, a study in this thesis attempts to determine the tradeoff between optimizing a departure trajectory for minimum time to climb, minimum fuel burn, and minimum noise as opposed to only optimizing for minimum noise. For approach, this study only studies configuration sensitivities. The SAI work mostly studies approach procedures, such as displacing the threshold, flying different speeds and different flight path angles. Some local sensitivity studies are presented herein to determine similarities and differences between the current fleet and the BWB configuration used by the SAI.

Other previous work at the Massachusetts Institute of Technology by John-Paul Clarke studied single event noise abatement procedures for the 737-200 [14]. These studies are not

optimizations and do not attempt to measure the trades between noise, time and fuel burn that are conducted in this work. For approach Clarke studies three procedures, the standard three degree glide slope approach, a decelerating approach where the aircraft speed is continually reduced while flying the three degree glide slope, and a vertically segmented approach where the aircraft flies a steep decent and then intercepts the three degree glide slope at a lower altitude. The three approaches are such that the last five hundred feet of the decent are the same. Clarke found that the segmented approach reduced 60 dB noise exposure area by 55% and the decelerating approach reduced 60 dB noise exposure area by 58%. For departure Clarke studied the impacts of a collection of single event departures including: a de-rated takeoff thrust, an enroute climb speed increase, a thrust cutback that starts at 800 feet and ends at 2,000 feet, and a 60% thrust cutback that starts at 800 feet but ends at a variable altitude. All of those isolated changes are compared to the standard departure contained in the Integrated Noise Model for the 737-200. Clarke found that the takeoff de-rate and the increased enroute climb speed, defined as the speed flown after an altitude of 3,000 feet, purely increased the noise exposure. However, for any application of a cutback, Clarke was able to reduce the land area exposed to peak noise levels, such as noise levels over 80 dB, but the total land area exposed to moderate noise levels, such as over 60 dB, will only increase. Clarke then tested two isolated changes to the ICAO departure procedure which is also contained in the INM and compared those to the standard INM procedure. Clarke showed that the ICAO procedure, and some isolated changes to it, including varying the transition altitude to enroute climb and climb thrust reduction could reduce the noise exposure when compared to the standard INM departure. The essential differences between Clarke's work and the work in this thesis is that this work will present the sensitivities of noise to low-speed aerodynamics and the aircraft configuration; for takeoff, it will show the trades between fuel burn, time to climb and noise. The departure trajectories computed herein will be optimized assuming the pilot is allowed to make up to four control inputs during the climb to 10,000 feet. These optimized trajectories will also determine the benefits of various flap settings for departure and will attempt to determine the best departure trajectory that a pilot can fly for minimum noise, fuel burn, and time to climb.

Another project called NOISHHH developed by Visser and Wijnen seeks to optimize departure trajectories for minimum population noise exposure [15], [16]. The papers present results for minimum fuel burn and minimum number of awakenings for three dimensional departure trajectories. This work is quite similar to the departure flight path optimization study conducted herein. Both of these studies use the same noise software, the Integrated Noise Model. A major difference between the studies is that Visser and Wijnen minimize population exposure, which can be done by flying around people or over them quietly, and in this work land area exposure is minimized. Both metrics are valuable, but minimizing exposed land area would be more useful in a global sense as some airports are in densely populated areas and the only way to reduce population impact is to minimize the amount of land affected. The other, much smaller differences are: the aircraft used, the 737-300 versus the 747-200 here; the trajectory computations are made with a slightly a different algorithm; and the optimization method used in Visser and Wijnen's work is nonlinear programming which requires a weighting of each objective so a single objective optimization is solved. Conversely, the analysis herein uses a Pareto optimal, multi-objective, genetic algorithm. Accordingly, a collection of unique points along the Pareto front are found by Visser that will miss any concave portions of the Pareto front, but the entire Pareto front is computed here. The results from both methods will be compared in Chapter 7.

#### **1.4. Organization of the Thesis**

The second chapter of this document will discuss how an airplane is parameterized for the low-speed aerodynamic estimates and the approximations made in modeling. The third chapter will present the low-speed aerodynamic model and all of the methods contained within it. The conclusion of the third chapter will present results and validation of the low-speed method and discuss its applicability. The fourth chapter will serve as the transition chapter between low-speed aerodynamics and noise. It will discuss trajectory modeling, why the trajectory is dependent on the low-speed aerodynamics, and the reasons the trajectories are important for noise considerations. The method to predict aircraft noise will then be presented in Chapter 5. The trajectory estimation and noise prediction methods will then be used to compute a sensitivity study of the noise to the low-speed aerodynamics. The trajectories used will

represent the noise certification procedures for a commercial aircraft takeoff and landing, and this will be presented in Chapter 6. Chapter 7 will present a capabilities demonstration and show an optimization study that estimates the Pareto front of optimal departure trajectories in terms of fuel burn, noise exposure, and time to climb for the Boeing 747-200. A conclusion summarizing the entire thesis will then be presented.



## CHAPTER 2: Modeling for Performance Estimation

The aircraft are parameterized in a way that is standard for aircraft preliminary design. The parameters are generally high-level and represent quantities that can be easily translated into performance. For instance, the planform area and the aspect ratio are important for predicting climb performance and induced drag, they also define most of the aircraft's wing geometry. This chapter defines all of the aircraft and flow parameters used for low-speed aerodynamic predictions. There are sixty parameters in total, and the approximate level of detail used in the low-speed model is shown in Figure 2.1.

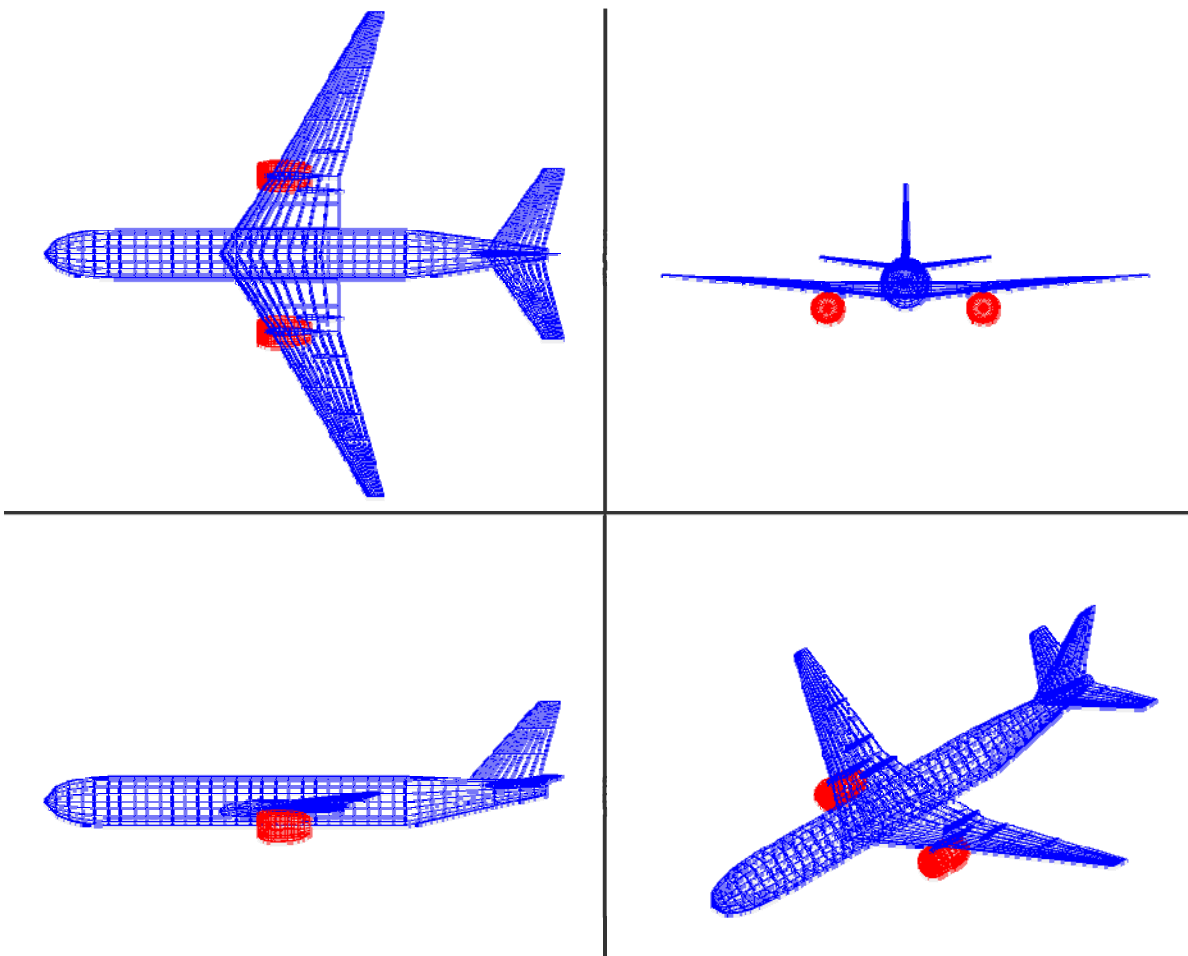


**Figure 2.1: Wireframe model showing the approximate detail of the aircraft used in the low-speed aerodynamic model.**

### 2.1. Aircraft Parameterization

The geometric parameters for the main wing are listed and explained in Table 2.1. The following table, Table 2.2, will detail all of the parameters that define the aircraft flap and slat

settings. The airplane fuselage parameters are defined in Table 2.3. The following tables, Table 2.4 and Table 2.5 define the aircraft horizontal tail and vertical tail respectively. The configuration parameters defining the aircraft engines are given in Table 2.6. Table 2.7 will then present the remaining parameters for low-speed analysis. A final section of this chapter will present the airfoil parameterization and rationale behind it.

<b>Geometric Parameters for the Main Lifting Surface</b>	
$\alpha_w, W_{inc}$	Incidence angle of the wing, degrees.
$\Lambda_{1/4}, SWEEP$	Quarter-chord sweep angle, degrees.
DIH	Wing dihedral (or anhedral), degrees.
SW	Wing planform area.
$\lambda, TR$	Wing taper ratio, tip chord/root chord
Y2	Spanwise location of wing trapezoidal breakpoint, also where the engine is located, fraction of span.
Wstart	Vertical location of the main wing at the aircraft centerline, negative if the wing is below the centerline, in aircraft length units.
CGW	Lengthwise location of the wing, measured from fictional point where leading edges of the wings would intersect on the aircraft centerline.

**Table 2.1 Wing geometric parameter list.**

<b>Geometric Parameters for Flaps and Slats</b>	
Y0	Spanwise beginning of inboard trailing edge flaps, fraction of span.
Y1	Spanwise end of inboard trailing edge flaps, fraction of span.
X1	Chord fraction of inboard trailing edge flap at Y1, X0 is computed from X1 because the trailing edge is assumed perpendicular to the fuselage, fraction of chord.
X2	Chord fraction at the spanwise beginning of the outboard trailing edge flap, located at Y3, fraction of chord.
Y3	Spanwise beginning of outboard trailing edge flaps, fraction of span.
X3	Chord fraction at the spanwise end of the outboard trailing edge flap, located at Y4, fraction of chord.
Y4	Spanwise end of outboard trailing edge flaps, fraction of span.
X4	Chord fraction at the spanwise beginning of the leading edge flap or slat, located at Y5, fraction of chord.
Y5	Spanwise beginning of leading edge flap or slat, fraction of span.
X5	Chord fraction at the spanwise end of the leading edge flap or slat, located at Y6, fraction of chord.
Y6	Spanwise end of leading edge flap or slat, fraction of span.
$\delta_f$	Trailing edge flap deflection, degrees.
$\delta_s$	Leading edge flap deflection, degrees.

**Table 2.2 Flap and slat geometric parameter list.**

<b>Geometric Parameters for the Fuselage</b>	
WD	Maximum fuselage depth/height, aircraft length scale units.
WF	Maximum fuselage width, aircraft length scale units.
XL	Length of the fuselage, aircraft length scale units.
Wtail	Final diameter of the fuselage trailing edge as a fraction of the maximum fuselage height, fraction of WD.
Wflat	Location where the nose of the fuselage becomes cylindrical, fraction of XL.
Wflat2	Location where the tail of the fuselage transitions from cylindrical, fraction of XL.
Wbend	Fuselage centerline upsweep angle, degrees.

**Table 2.3 Fuselage geometric parameter list.**

<b>Geometric Parameters for the Horizontal Tail</b>	
HTinc	Horizontal tail angle of incidence, degrees.
ARHT	Horizontal tail aspect ratio.
SWPHT	Quarter-chord sweep angle, degrees.
HTDIH	Horizontal tail dihedral (or anhedral), degrees.
SHT	Horizontal tail planform area.
TRHT	Horizontal tail taper ratio.
HTstart	Vertical location of the horizontal tail above the aircraft centerline, in aircraft length units.

**Table 2.4 Horizontal tail geometric parameter list.**

<b>Geometric Parameters for the Vertical Tail</b>	
ARVT	Vertical tail aspect ratio.
SWPVT	Quarter-chord sweep angle, degrees.
HTDIV	Vertical tail dihedral (or anhedral), degrees.
SVT	Vertical tail planform area.
TRVT	Vertical tail taper ratio.

**Table 2.5 Vertical tail geometric parameter list.**

<b>Geometric Parameters for Aircraft Engines</b>	
Edia	Engine fan diameter, aircraft length scale units.
ELen	Engine maximum length, aircraft length scale units.
NacT	Nacelle thickness, aircraft length scale units.

**Table 2.6 Aircraft engine geometric parameter list.**

<b>Other Model Parameters</b>	
GearDown	Boolean variable indicating whether or not the landing gear is deployed.
Re L	Reynolds number per foot *10 <sup>-6</sup> .
Mach	Mach number used for skin friction coefficients.

**Table 2.7 Other low-speed aerodynamic model parameters.**

## **2.2. Airfoil Parameterization**

### *2.2.1. Main Lifting Element*

The airfoils used for the main lifting element in the low-Speed aerodynamics tool are all NACA 6-series; however, only three of the six parameters for a NACA 6-series airfoil are used. NACA 6-series airfoils were selected for this tool because of the flexibility in their geometry and that they can be used on aircraft with transonic cruise speeds. NACA 6-series airfoils can represent highly aft-loaded airfoils with good transonic properties, they can be made to mimic NACA 4-series airfoils, or they can represent other more complicated airfoils by allowing fractional parameters. The 6-series airfoils are accordingly a good choice for airfoil modeling as they enable a large variety of airfoils to be parameterized with a small number of parameters. The parameters for a complete NACA 6-series airfoil are listed with an example in Table 2.8.

<b>NACA 65<sub>2</sub>-212 a=0.8</b>	
6	Specifies the airfoil as a NACA 6-series airfoil
5	Location of minimum C <sub>p</sub> in tenths of the chord
2	Half-width of low-drag bucket in tenths of C <sub>L</sub>
2	Airfoil design lift coefficient in tenths.
12	Thickness to chord ratio of the airfoil in hundredths.
0.8	Percentage of the airfoil with laminar flow, degree of aft loading.

**Table 2.8 NACA 6-Series Airfoil, parameter definition [17].**

Using an early variant of the low-speed aerodynamics tool, a design space study was conducted on an aircraft where all of the airfoil parameters for a NACA 6-series airfoil were varied. The only portions of the tool affected by the airfoil are the vortex lattice method for induced drag and the skin friction method used for profile drag; both methods are discussed in chapter 3. It

was found that for the vortex lattice method only the airfoil design lift coefficient, airfoil thickness to chord ratio, and laminar flow fraction changed any of the results. For the skin friction method, the only parameter that had any impact was the thickness to chord ratio. Therefore, the only parameters used in this method for the airfoils are the design lift coefficient, thickness to chord ratio, and percentage of laminar flow. The remaining parameters are a NACA 63<sub>2</sub>-\*\*\* airfoil.

### 2.2.2. Tail Lifting Surfaces

In the low-speed aerodynamics tool the tail surfaces are parameterized by only the thickness to chord ratio of the airfoil. Accordingly, they are treated as NACA 4-Series symmetric airfoils. This means the NACA 4-series designations would be 00\*\*. It would be a trivial modification to include NACA 6-series airfoils or complete airfoil profiles for the tail surfaces.

### 2.2.3. Airfoil Parameter List

<b>Airfoil Parameter List</b>	
C11	Design lift coefficient of the main wing at wing root.
A1	Airfoil percentage aft loading at the wing root.
TOC1	Thickness to chord ratio of the main wing at the wing root.
C12	Design lift coefficient of the main wing at trapezoidal break, Y2.
A2	Airfoil percentage aft loading at trapezoidal break, Y2.
TOC2	Thickness to chord ratio of the main wing at trapezoidal break, Y2.
C13	Design lift coefficient of the main wing at wing tip.
A3	Airfoil percentage aft loading at the wing tip.
TOC3	Thickness to chord ratio of the main wing at the wing tip.
HTTOC	Horizontal tail thickness to chord ratio.
VTTOC	Vertical tail thickness to chord ratio.

**Table 2.9 Airfoil parameter list.**



## CHAPTER 3: Low-Speed Aerodynamics Estimation Method

The goal of the Low-Speed Aerodynamics Estimation is to predict the drag polars, lift curves, and maximum lift coefficients of subsonic commercial transport aircraft quickly and with accuracy similar to a manufacturer preliminary design trade study. The speed of the prediction must be such that the entire United States fleet, or about 5,000 aircraft types, can be predicted in a weekend's time. That sets an upper bound on the solution time of about 20 seconds. The level of accuracy desired would be similar to computational fluid dynamics, but with less than a hundredth of the solution time required. Accordingly, a collection of physics-based and empirical methods have been combined to predict aircraft low-speed performance.

The chapter will be divided into five sections, (1) a summary of the method and relative importance of its components, (2) a detailed explanation of the method to estimate the clean configuration, or flaps up and slats up drag polar, (3) a similar explanation for the high-lift drag polar, (4) an explanation of the method to estimate the maximum lift coefficient and the lift curves, and lastly, (5) a discussion of modeling pitfalls and suggestions for achieving accurate predictions. Each section discussing an estimation method, for instance, clean drag polars, high-lift drag polars, maximum lift coefficient, and lift curve estimation will have a self-contained validation section.

### **3.1. High-Level Overview**

The method is structured so an airplane geometry can be manipulated and analyzed to estimate three key outputs, clean configuration drag polars, high-lift configuration drag polars, and lift curves. The information flow of the entire method is shown in Figure 3.1.

# Low Speed Aero Flow Chart

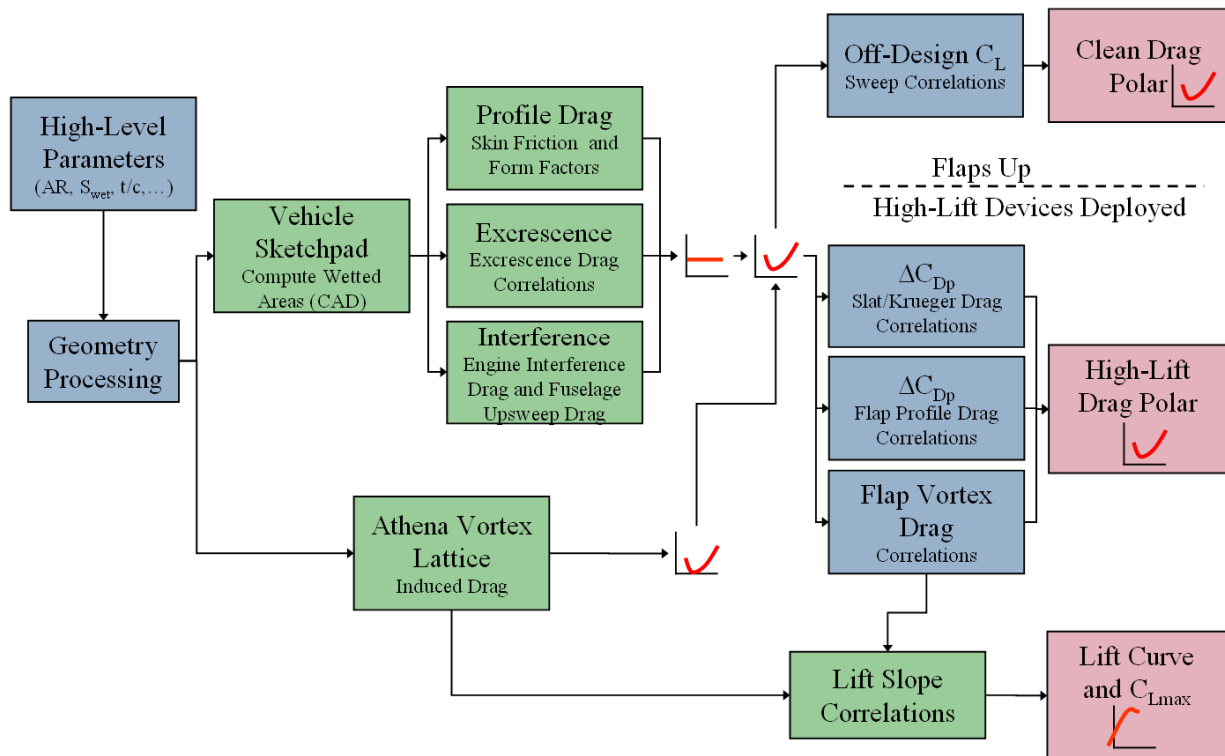


**Figure 3.1 – Presentation of a flow chart of the low-speed aerodynamics methodology, which has been color coded to show the source of the method. Blue indicates work that is predominantly created in this thesis, green indicates work that is largely from other sources, but modified to fit this framework, and red indicates a result.**

Another important piece of information is the relative magnitudes of the different components of drag. This information is shown for both a clean and high-lift configuration of a Boeing 777-200 in Figure 3.2. For a clean configuration the profile drag and induced drag account for up to ninety percent of the drag, and the remaining components of drag are empirical correction terms. For the high-lift configuration, slat drag, profile drag, induced drag and slat drag are all important terms, and the remaining portion of drag is also an empirical correction.

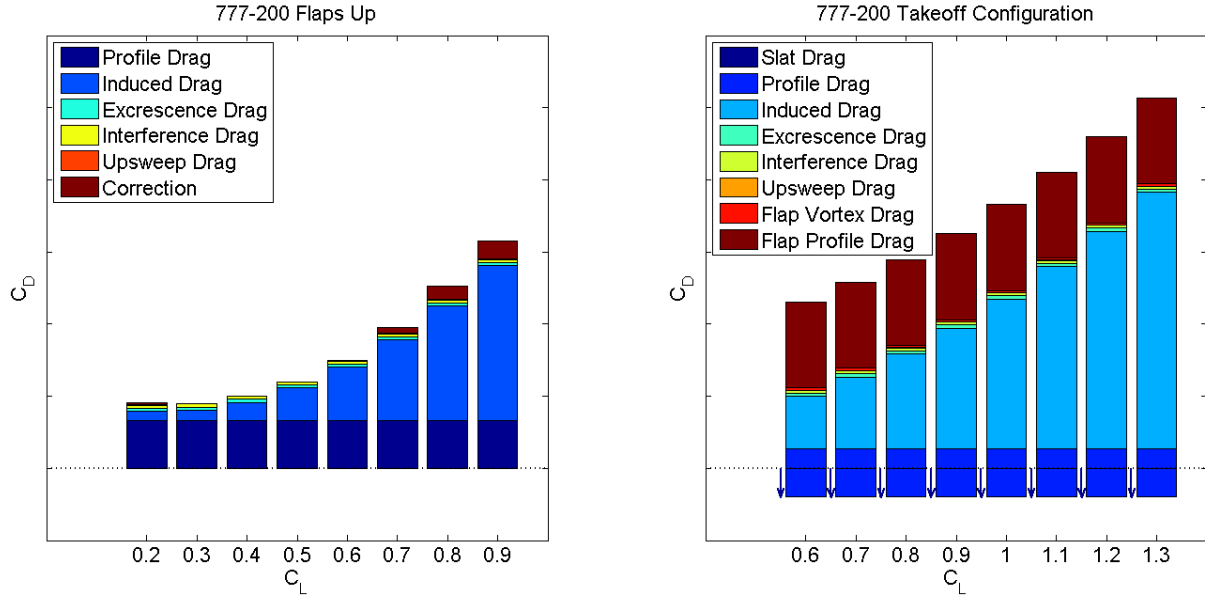


**Figure 3.2:** Figure showing the relative magnitudes of the different components of drag for both a clean and high-lift configuration using the low-speed aerodynamic model and public geometry for a Boeing 777-200.

### 3.2. Clean Configuration Drag Polar

The clean configuration drag polar is defined as the sum of five components of drag, profile drag, induced drag, excrescence drag, interference drag and off-design drag. The computation of the total aircraft drag coefficient is shown in Equation 3.1.

$$C_D = C_{Dp} + C_{Dind} + C_{De} + C_{Dint} + \Delta C_D \tag{3.1}$$

#### 3.2.1. Profile Drag

Profile drag is the drag due to skin friction and form drag due to boundary layer growth. Both phenomena have been well captured by empirical relationships, and the profile drag predictions can be considered one of the most accurate parts of this method. The skin friction drag will be treated as an empirical skin friction coefficient multiplied by the wetted area of a component divided by a reference area, and the pressure drag will be modeled as a form factor multiplying the skin friction drag. Equation 3.2 shows the complete formula for the profile drag.

$$C_{Dp} = C_F \frac{S_W}{S_{Ref}} FF \quad 3.2$$

The code used to predict the profile drag is called “Friction.f” and is produced by W.H Mason at Virginia Tech. A brief theoretical summary of the code will be given herein; however, for a more in-depth discussion of the theory in “Friction.f” the reader is urged to see the user’s guide [18].

### Skin Friction Drag

Skin friction drag is the force caused by the molecules of air sliding along the surface of the aircraft. The skin friction drag coefficient,  $C_F$ , is a weighted sum of the laminar skin friction and turbulent skin friction coefficients based on the fraction of the reference length exposed to each type of flow, the equation to compute the skin friction is presented in Equation 3.3.

$$C_F = C_{F_{turbulent}} \left|_l - \left( \frac{x_{transition}}{l} \right) \left[ C_{F_{turbulent}} \left|_{x_{transition}} - C_{F_{laminar}} \left|_{x_{transition}} \right. \right] \quad 3.3$$

For cases with fixed transition, such as the wind tunnel models  $x_{transition}$  should be set to the appropriate location; however, for commercial aircraft  $x_{transition}$  can be approximated quite accurately as zero.

The laminar skin friction coefficient assumes flat plate Blasius flow corrected for compressibility. For Blasius flow, the skin friction coefficient is only a function of the Reynolds number, but in this model there is compressibility correction,  $C^*$ , the Chapman-Rebesin constant, see Equation 3.4. The Reynolds number used for this method is the standard definition with a reference density, velocity, length, and viscosity as presented in Equation 3.5. The assumptions of the method are that air has a Prandtl number of 0.72, a recovery factor of the square root of the Prandtl number,  $Pr^{1/2}$ , a specific heat ratio,  $\gamma=1.4$ , and a boundary layer edge temperature of  $T_e=390$  °R.

$$C_F = 2 \left( \frac{0.664 \sqrt{C^*}}{\sqrt{\text{Re}}} \right) \quad 3.4$$

$$\text{Re} = \frac{\rho_{\text{Ref}} V_{\text{Ref}} L_{\text{Ref}}}{\mu_{\text{Ref}}} \quad 3.5$$

The turbulent skin friction coefficient estimation procedure is substantially more complicated. It involves solving an implicit nonlinear system of equations that include the Reynolds number and compressibility effects. A thorough description of the method is left to reference [18]. The assumptions for turbulent flow are that the recovery factor,  $r=0.88$ , and the boundary layer edge temperature is  $T_e=400^\circ\text{R}$ .

### Form Drag

Form drag is the force caused by the boundary layer wake behind the body; it is essentially a remnant of the boundary layer momentum thickness. The boundary layer momentum thickness is correlated to the skin friction coefficient (by the integral boundary layer equations), which means that the form drag is closely related to the skin friction drag. For the skin friction drag only the body's wetted area matters as it is the friction of the air molecules sliding past. However, form drag includes effects of the boundary layer momentum thickness which means that it is also a function of the body's thickness. Accordingly, the form factor will be an empirical function of the thickness to chord ratio for a planar aircraft component, and will be an empirical function of the fineness ratio, ratio of the diameter to length, for a body of revolution. The empirical function for a planar form factor is shown in Equation 3.6, and the empirical function for the form factor of an axisymmetric body is shown in Equation 3.7.

$$FF_{\text{planar}} = 1 + 2.7 \frac{\tau}{c} + 100 \left( \frac{\tau}{c} \right)^4 \quad 3.6$$

$$FF_{\text{body}} = 1 + 1.5 \left( \frac{d}{l} \right)^{1.5} + 7 \left( \frac{d}{l} \right)^3 \quad 3.7$$

## Profile Drag Verification

The profile drag methodology was tested with two cases, NASA wind tunnel tests of a subsonic commercial transport [19], and the Boeing 737-700. In addition, the method was compared with an alternative method from Shevell [20]. A wireframe diagram of the wind tunnel model is shown in Figure 3.3, and a wireframe model of the 737-700 is shown in Figure 3.4.

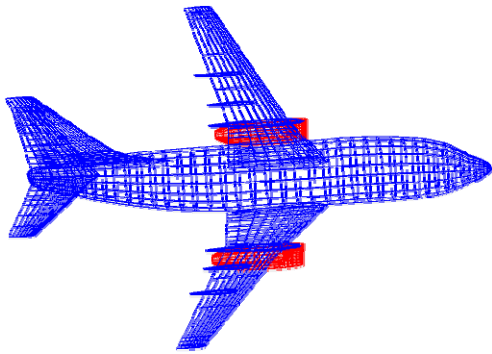


Figure 3.3 Wireframe sketch of NASA TN D-5971 wind tunnel model [19].

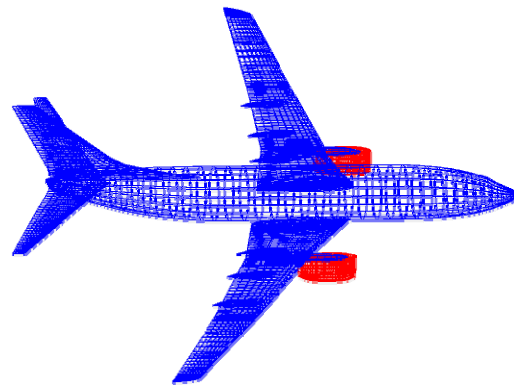


Figure 3.4 Wireframe sketch of a Boeing 737-700.

The wind tunnel measurements and correlations agreed almost perfectly. The worst case error was 2 drag counts or 1.13%. The complete results are in Table 3.1.

Mach No.	$C_{Dp}$	"Friction.F" $C_{Dp}$	Nominal Error	%Error
0.550	0.02113	0.02114	0.0000	0.047%
0.725	0.02035	0.02058	0.0002	1.130%
0.775	0.02015	0.02019	0.0000	0.199%
0.850	0.01983	0.01988	0.0000	0.252%

Table 3.1 Profile drag comparison between wind tunnel measurements and "Friction.f" for the model in NASA TN D-5971 [19].

The method in Shevell only contains data for Mach 0.5, so only one comparison is made. However, again the total error is 2 drag counts which is 1.05% error. The complete results of the comparison are in Table 3.2.

Mach No.	$C_{Dp}$	"Friction.F" $C_{Dp}$	Nominal Error	%Error
0.500	0.02100	0.02122	0.0002	1.048%

**Table 3.2 Profile drag comparison between method in Shevell and "Friction.f".**

The profile drag predictions for the 737-700 also have a similar error of 1.58%. Thus, for the comparisons done it appears that the correlations in “Friction.f” are accurate to within 1.6% or better for the types of aircraft examined in this thesis.

### 3.2.2. Induced Drag

The induced drag is computed using Athena Vortex Lattice, AVL, written by Mark Drela and Harold Youngren [21]. The geometry of the lifting surfaces is translated and imported to AVL. AVL then computes the lift and induced drag at the Trefftz Plane. Vortex lattice methods assume potential flow and that lift is always linearly proportional to angle of attack, so at low angles of attack they are quite accurate; however, at high angles of attack their predictions break down.

### 3.2.3. Excrescence Drag

Excrescence Drag will be defined as the drag due to “all deviations from a smooth external surface,” such as, antennas, air-conditioners, rivets, skin-waviness, sheet metal joints, etc. The definition is based on an ESDU document, reference [22], which defines all of the components of excrescence drag, and then correlates the total aircraft excrescence drag to the total aircraft wetted area. This is the selected approach for the low-speed aerodynamic estimates. An alternative approach is to simply increase the profile drag by 6% [20]. Validation cases show the ESDU method more accurate than the 6% profile drag increase.

The excrescence drag model was validated with Boeing flight test results for the 737-700 and 777-200. For the 737-700, the excrescence drag prediction is off by 8.9% which is 0.9% of total drag. For the 777-200, the excrescence drag prediction is off by 4.0% which is 0.2% of total drag.

The excrescence drag levels from reference [22] are shown in Figure 3.5. They are interpreted herein as ‘Historic Aircraft’, ‘Current Aircraft’, and ‘Presumed Future Minimum’ which is slightly different from the definitions given in the reference. However, each curve is the product of the excrescence drag coefficient and the aircraft wetted area, so division by the aircraft reference area is necessary to convert to an actual drag coefficient. The drag levels are interpolated using a technology factor, where 0 is historic (circa 1960), 1 is current technology (circa 2000), and 2 is the presumed future minimum (asymptotic minimum). Therefore, any technology factor between 0 and 2 will result in an interpolation between two of those curves.

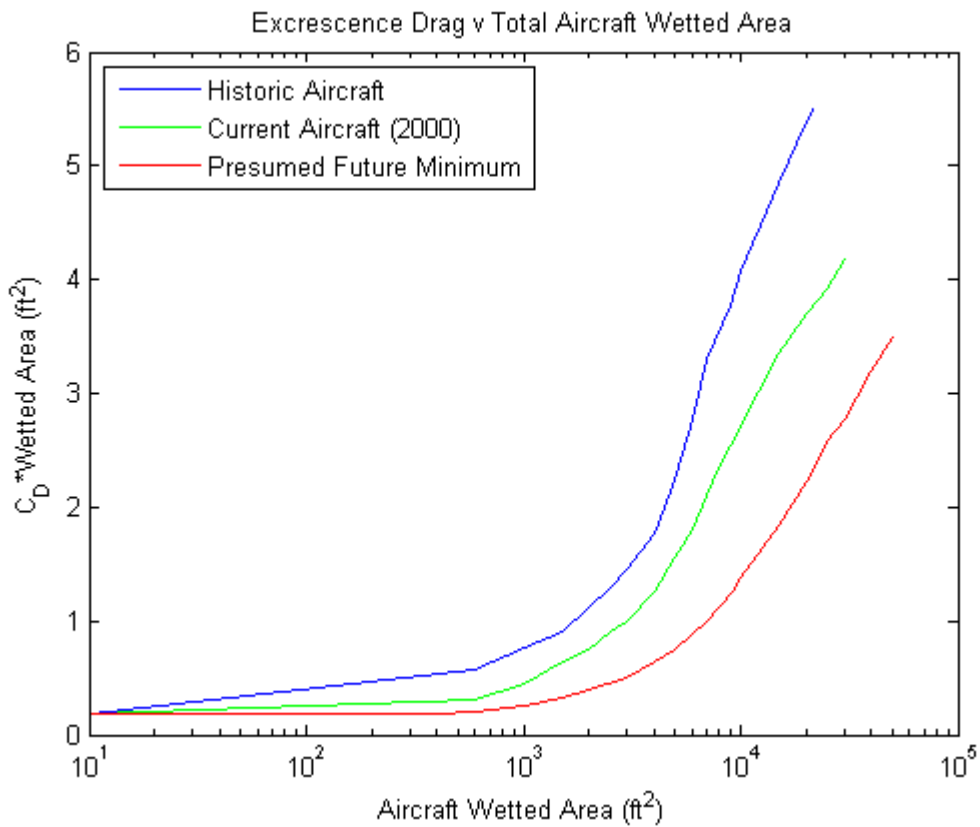


**Figure 3.5** Excrescence drag as a function of aircraft total wetted area and a technology factor [22].

### 3.2.4. Interference Drag

Interference drag is separated into two components, Engine-Nacelle-Pylon-Wing interference and fuselage upsweep drag.

### Engine-Nacelle-Pylon-Wing Interference

Engine-Nacelle-Pylon-Wing Interference is to account for any effects of scrubbing between the high velocity jet from the engine exhaust, or the free-stream flow being entrained into the jet, and the aircraft wing or pylon. At high-speed the interference will also include the compressibility effects of a virtual streamtube between the pylon and fuselage and between the wing and the engine. It seems apparent that a method for predicting interference drag in this region should be a function of the engine size, distance between the nacelle and the wing, and the distance between the engine intake and wing leading edge. Before computational fluid dynamics (CFD) it appears this was the case, as reference [8], has a correlation for interference drag that is a function of these geometric parameters. However, the results in that paper are considerably dated as all of the engines in the study are for zero bypass ratio engines. A more recent study by Tinoco and Chen states that because of CFD the past correlations for interference drag based on geometry and engine parameters are all invalid. Redesigns of old aircraft from those correlations were done to show that previous techniques to restrict engines from being too close to the wing to prevent high interference drag were no longer appropriate. The past aircraft designed with those design correlations could be retrofitted with new close-coupled layouts with a similar drag penalty [23].

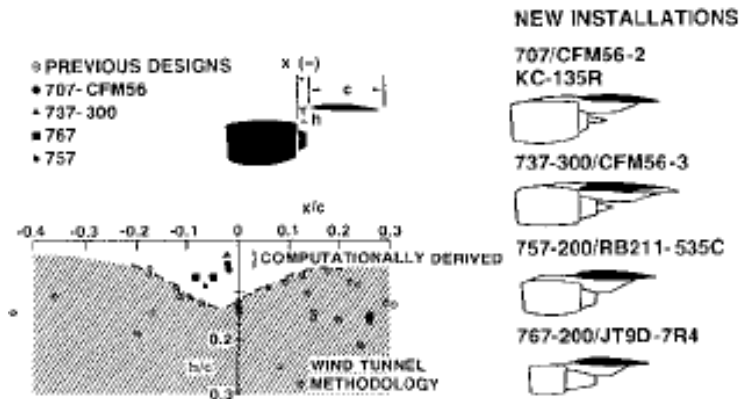


**Figure 3.6 Comparison between original engine integration schemes and computationally derived integration schemes with similar interference drag [23].**

A more recent study by Berry discusses the engine airframe integration of the Boeing 777 and some of the factors involved. It is clear that the geometric position of the engine both vertically

and laterally with respect to the wing, and the bypass ratio are important parameters. The largest effect of the bypass ratio is to increase the amount of the pylon scrubbed by high-velocity flow as well as to decrease the velocity of the jet from the engine. The article recommends CFD as the primary tool to design or to analyze engine integration methods and to use supplemental wind tunnel testing [24].

An exhaustive search for a proper low-fidelity technique to predict this type of interference drag proved unfruitful. The current method employed is a correlation created from wind tunnel tests of external stores underneath a wing contained in Hoerner [26]. The function only has one of the expected parameters, which is the ratio of distance between the bottom of the wing and the top of the nacelle,  $y$ , to the diameter of the nacelle,  $d$ . The correlation is shown in Equation 3.8.

$$C_{D_{\text{int}}} = 0.147 \left( \frac{y}{d} \right) \pi \left( \frac{d}{2} \right)^2 \frac{1}{S_{\text{Ref}}} \quad 3.8$$

### **Fuselage Upsweep Drag**

Fuselage upsweep drag is the additional drag caused by the downwash of the wing deflecting the flow along the aft portion of the fuselage. The minimum fuselage drag occurs when the flow along the aft portion of the fuselage is aligned with the fuselage axis, but because of takeoff and landing constraints the aft portion of the fuselage is swept upward so the aircraft can have a higher rotation angle when close to the ground. The upsweep of the fuselage causes the flow past the aft fuselage to not be aligned with the fuselage axis. In the drag model discussed in this thesis, upsweep drag and induced drag are the only two drag components that vary with lift. Upsweep drag varies with lift because as lift increases the angle of the downwash also increases. In Figure 3.7, the red line corresponds to the fuselage mean line, and the black lines are to sketch the approximate downwash.

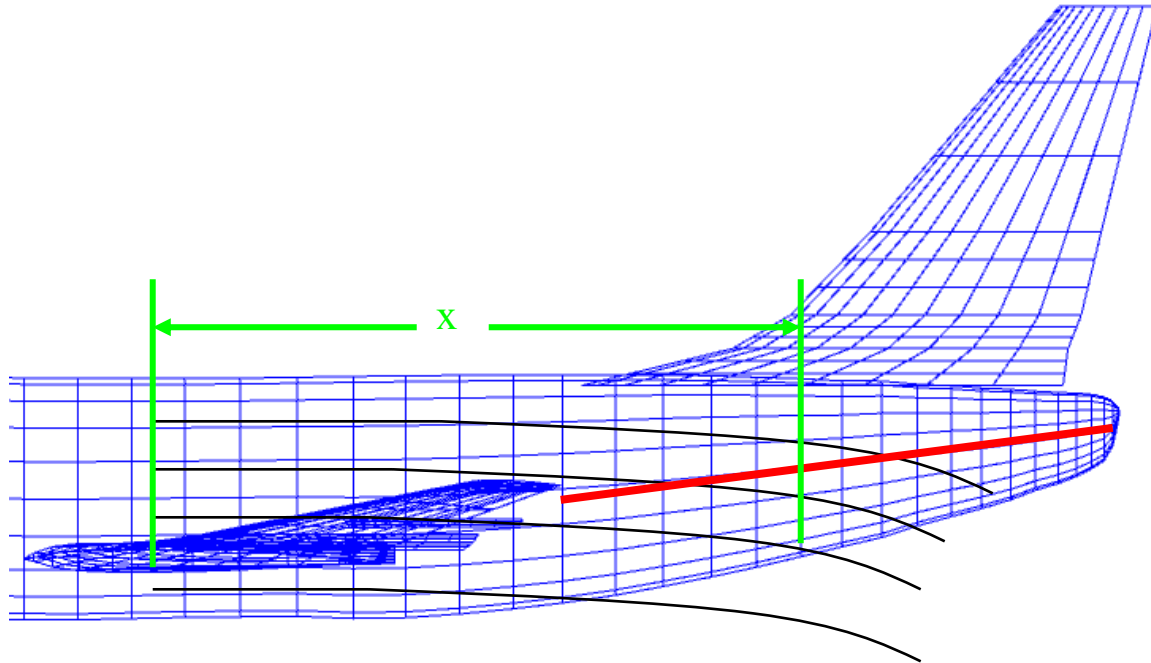


**Figure 3.7 Sketch of the wing downwash going past the tail of the fuselage and the cause of upsweep drag.**

The methodology for computing fuselage upsweep drag is taken from ESDU [27], and the reader is urged to see that document for complete details, as only a short outline will be provided here. The first part of the method is to compute the local downwash angle in the region of the fuselage upsweep. Although the vortex lattice method may provide a good estimate of local downwash, the ESDU method contains an empirical prediction which was selected to maintain consistency. The downwash angle relative to the fuselage is based on the standard method to compute the downwash angle for a wing, the lift curve slope divided by pi and the aspect ratio multiplied by the angle of attack. However, for the downwash relative to the fuselage, there is an empirical correction  $H$  based on the wing sweep and the distance between the wing and upswept fuselage. The formula for the local downwash angle is shown in Equation 3.5. The remainder of the method is to define a function,  $G$ , which is a function of the angle of attack, fuselage centerline upsweep angle, and the downwash angle, given in Equation 3.10. The difference between the function  $G$  evaluated at zero upsweep,  $\beta=0$ , and the upsweep angle,  $\beta$ , multiplied by a collection of empirical corrections is the upsweep drag. The two empirical corrections account for a non-circular fuselage profile,  $k$ , and cross-flow behind the fuselage,  $c_{ds}$ . The derivation and empirical fits for those two corrections are left to the reference. Also, the fuselage upsweep drag is referenced to the aft fuselage planform area,  $S_p$ ,

which is shown in Figure 3.8. It is necessary to convert the reference area to the standard reference, the wing planform area. Accordingly, Equation 3.11 shows the complete formula to compute fuselage upsweep drag, using the function  $G$ , empirical correction factors, and conversion to the correct reference area.

$$\varepsilon = \frac{2Ha}{\pi AR} \alpha \quad 3.9$$

$$G(\alpha, \beta, \varepsilon) = \frac{\sin|\alpha - \beta| \cdot \sin^2(\alpha - \beta - \varepsilon)}{\cos \beta} \quad 3.10$$

$$C_{D_{\text{int}}} = [G(\alpha, \beta, \varepsilon) - G(\alpha, 0, \varepsilon)] k c_{ds} \frac{S_p}{S} \quad 3.11$$

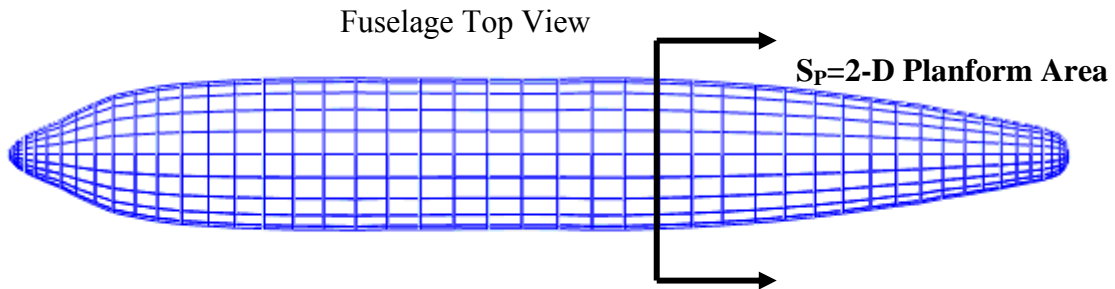


Figure 3.8 Schematic of the aft fuselage planform area used to compute fuselage upsweep drag,  $S_p$ .

### 3.2.5. Off-Design Drag

The vortex lattice code produces a solution in which the lift coefficient is linearly related to the angle of attack. For small angles of attack, the vortex lattice predictions and the flight test data show excellent correlation; however, the predictions and flight test data diverge rapidly at only a couple of degrees angle of attack. Dr. Liebeck [25] recommended adding in empirical corrections to the drag polar as a function of  $C_L - C_{L_{\text{design}}}$  and wing sweep.

The empirical correction curves are based on wind tunnel data and flight test data for six aircraft. The aircraft geometries are in Appendix A: Aircraft Geometries, but the sweep angles are shown in Table 3.3.

Aircraft	Sweep
NASA TN D-5971	26.3°
Boeing 727-100	32°
Boeing 737-700	~25°
Boeing 747-100	37.5°
NACA L50F20	47.7°
NACA L8H20	51.3°

Table 3.3 Wing quarter-chord sweep angle for test case aircraft.

The correction curves are selected such that each aircraft is interpolated between two of the constant sweep curves. Accordingly, each curve will affect two models so there should be some implicit consistency due to this procedure. For aircraft with sweep less than thirty degrees, the thirty degree sweep curve should still be applied. The empirically determined curves are plotted in Figure 3.9.

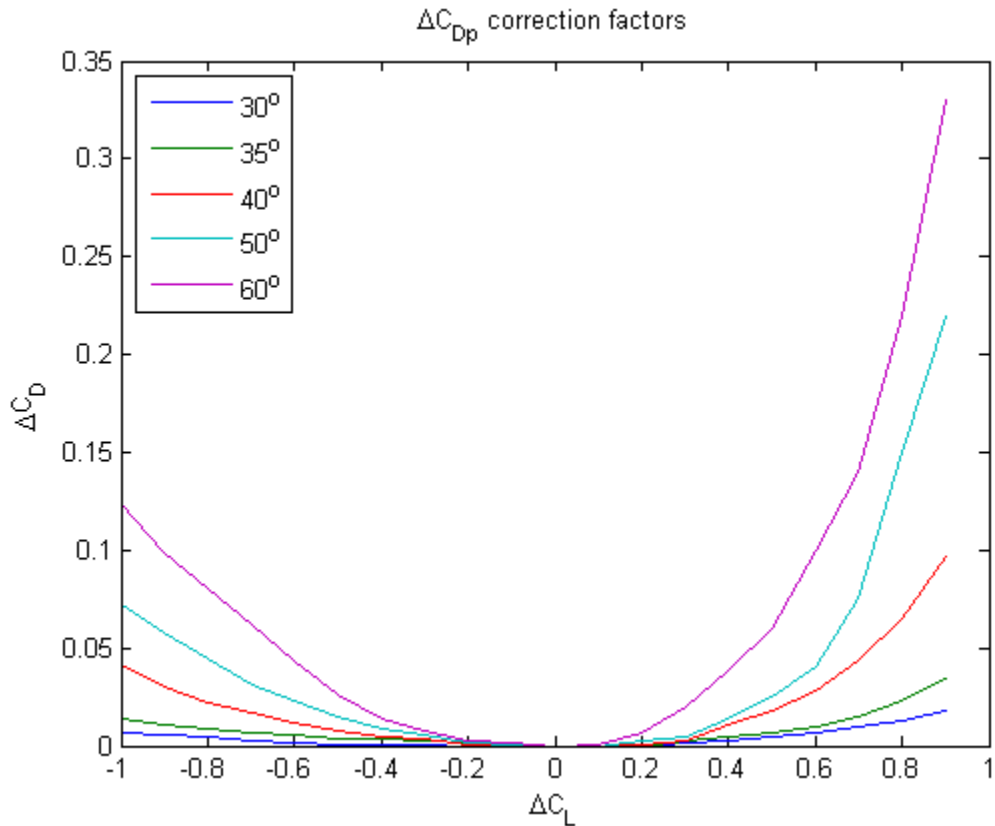
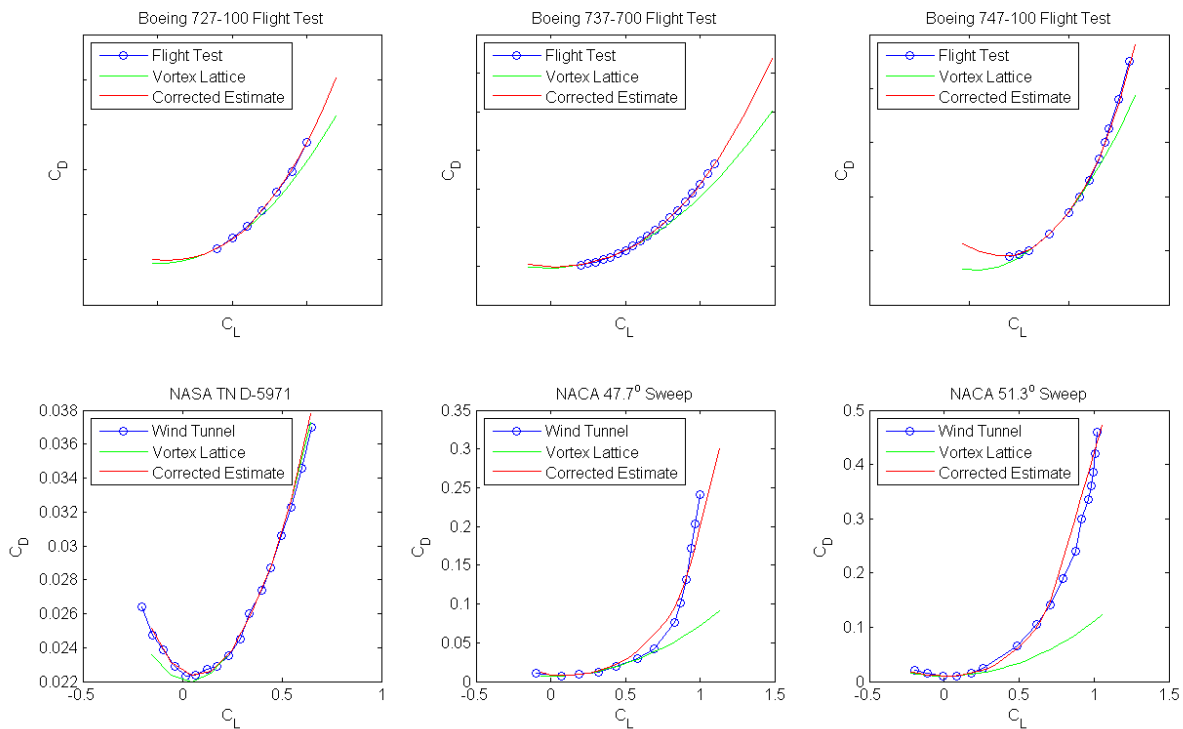


Figure 3.9 Incremental drag coefficient as a function of  $C_L - C_{Ldesign}$  and wing sweep.

The parameter  $C_{L_{design}}$  is 0.4 for all of the full-aircraft configurations. For a single lifting element configuration the design lift coefficient should be the lift coefficient at which the minimum drag occurs. For the two NACA single lifting element test cases used in this thesis, the entire wing used a constant NACA 6-series airfoil, so  $C_{L_{design}}$  is known a priori because of the airfoil definition. Therefore, the procedure for choosing  $C_{L_{design}}$  should be 0.4 for aircraft with a wing and tail or the lift coefficient of minimum drag for a single lifting surface configuration.

Figure 3.10 shows the effect of adding the off-design drag to the potential flow induced drag computed by the vortex lattice method. For angles of attack where  $C_L$  is approximately linear with angle of attack, between  $C_L=0.2$  and  $C_L=0.6$ , the vortex lattice prediction is quite good. However, as viscous effects increase the linear relationship between lift and angle of attack no longer holds and the vortex lattice method underestimates the drag. The off-design drag is applied using cubic spline interpolation, which does allow for extrapolation. The effect of the extrapolation is that approximations of drag above  $C_L=C_{L_{design}}+0.9$ , is a drag prediction which shows rapid growth along a cubic polynomial. This is an artificial stall mechanism, meaning there will be a rapid drag rise with increasing lift; however, it is purely numerical and is not a physical representation of stall. This is evident on both of the drag polars for the NACA single lifting surface models, the two results on the bottom right of Figure 3.10, where the estimated drag grows sharply at high  $C_L$ , but not in the same manner as the wind tunnel result.



**Figure 3.10** The effect of the  $\Delta C_d$  v  $\Delta C_L$  curves when applied to the drag polars predicted by the vortex lattice method.

### 3.3. Method Results – Flaps Up

Six validation cases were used to determine the validity of this method for clean aircraft: a comparison between wind tunnel results for the NASA TN D-5971 model discussed previously; wind tunnel test results two single lifting element highly swept wings; and comparisons between flight test results for the Boeing 727-100, Boeing 737-700, and the Boeing 747-100. In addition, a comparison of the drag polar for the 777-200ER predicted by this method and a purely empirical method called the Delta Drag Method [7] was undertaken to compare the predictions of methods with similar cruise-configuration fidelity.

For clean airplanes, the results of this method are very good over the validated range of the  $\Delta C_d$  v  $\Delta C_L$  curves as shown in Figure 3.9. For complete aircraft, this range should be considered between  $C_L = -0.4$  and  $C_L = 1.0$ , but for a single lifting surface, tail-less airplane, the

range should be considered between  $C_L=-0.4$  and  $C_L=0.7$ . Within these ranges the drag prediction should be within approximately 1% of the actual aircraft drag.

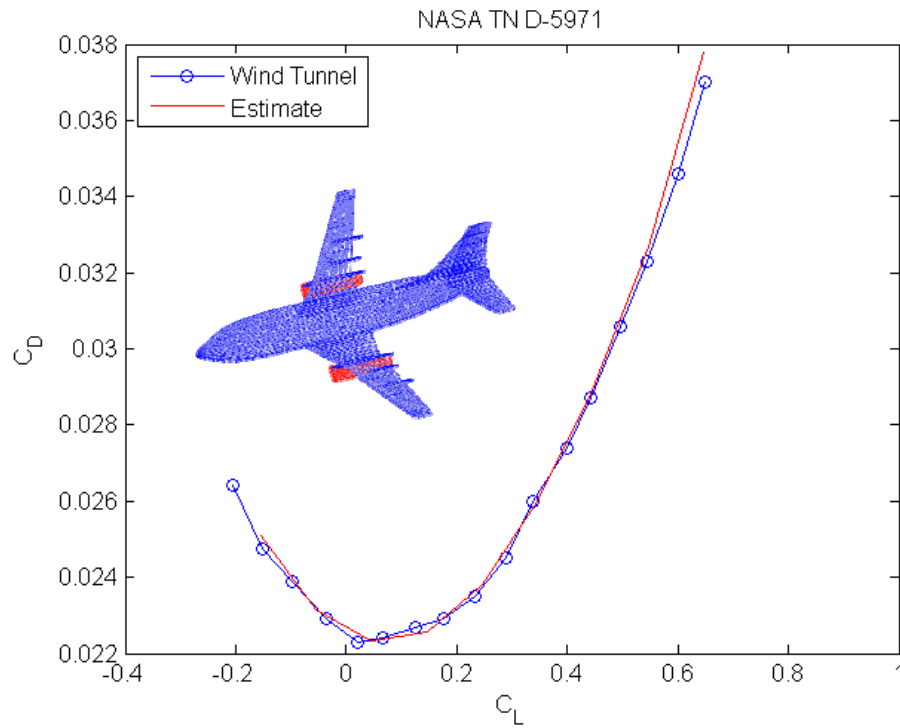


Figure 3.11 Comparison between wind tunnel results and predictions for the model of NASA TN D-5971 [19].

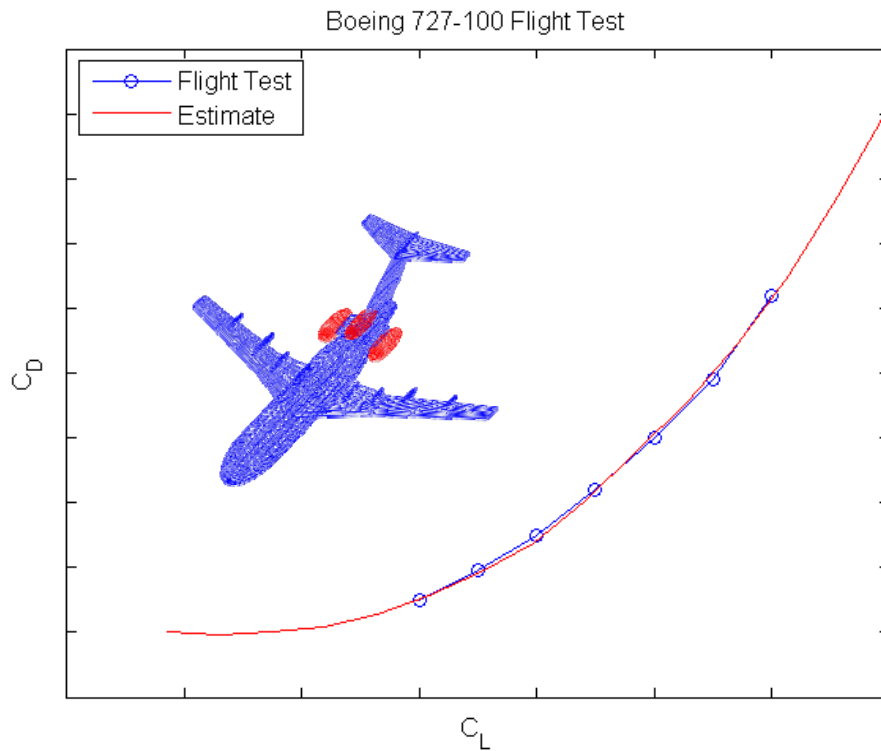
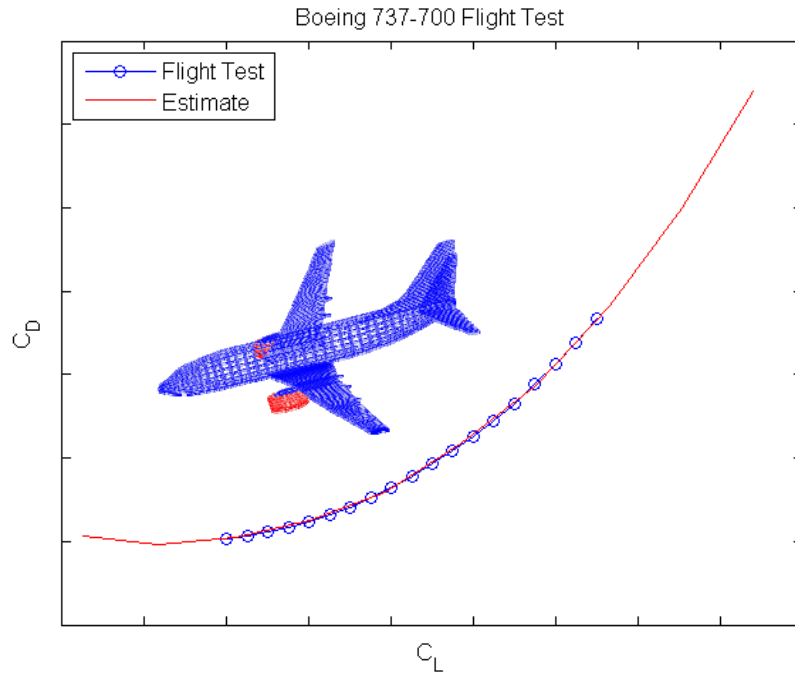
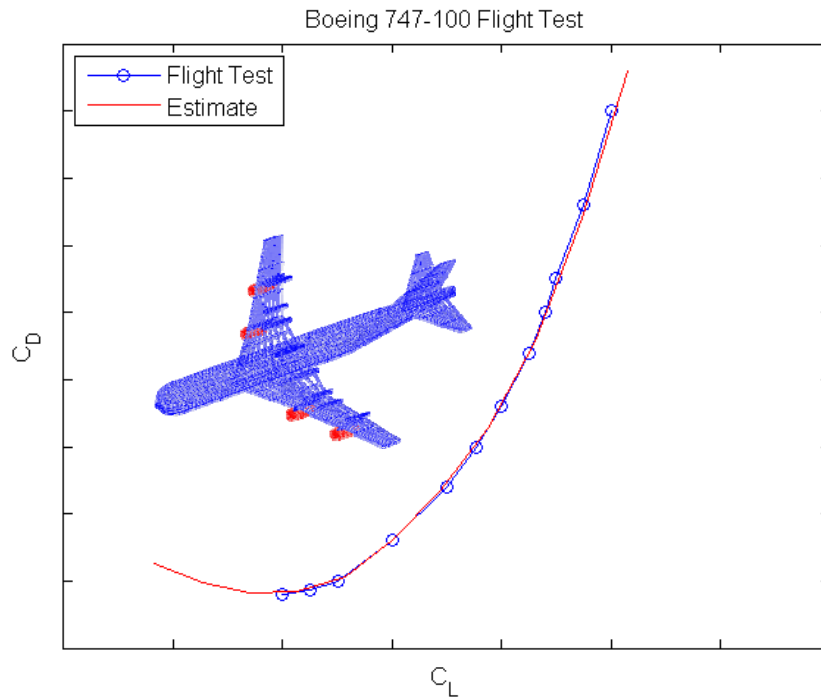


Figure 3.12 Comparison between Boeing 727-100 flight test data and the predictions of the low-speed aerodynamics model.



**Figure 3.13 Comparison between Boeing 737-700 flight test results and low-speed aerodynamics method predictions.**



**Figure 3.14 Comparison of Boeing 747-100 flight test data and the predictions of the low-speed aerodynamics predictions.**

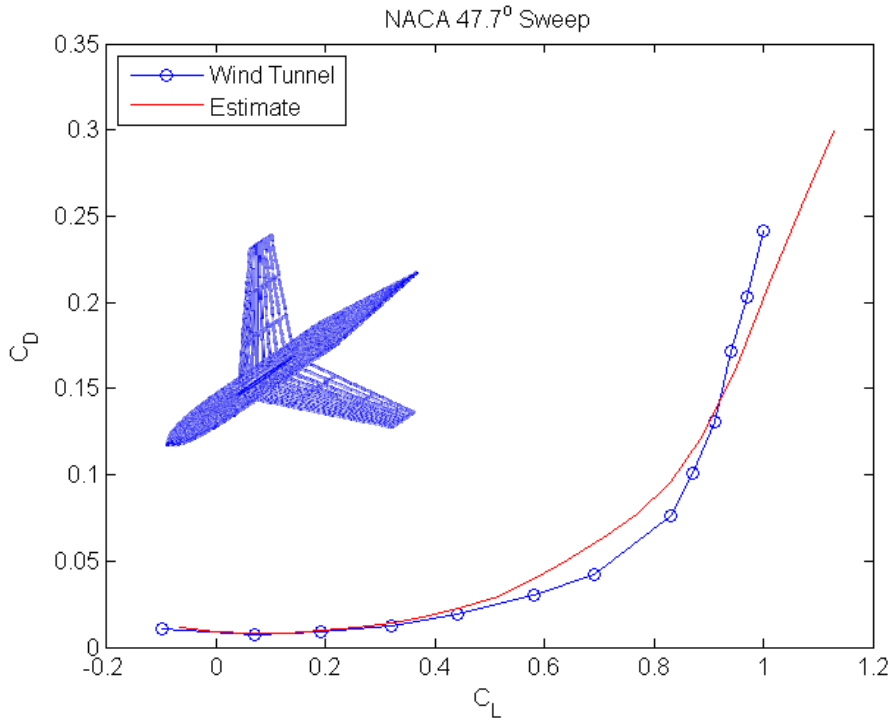


**Figure 3.15 Comparison of NACA RM L50F20, 47.7° swept wing and the predicted drag polar. The sharp rise of the drag prediction is clear near stall, and it is quite evident that it is not physical representation of stall.**

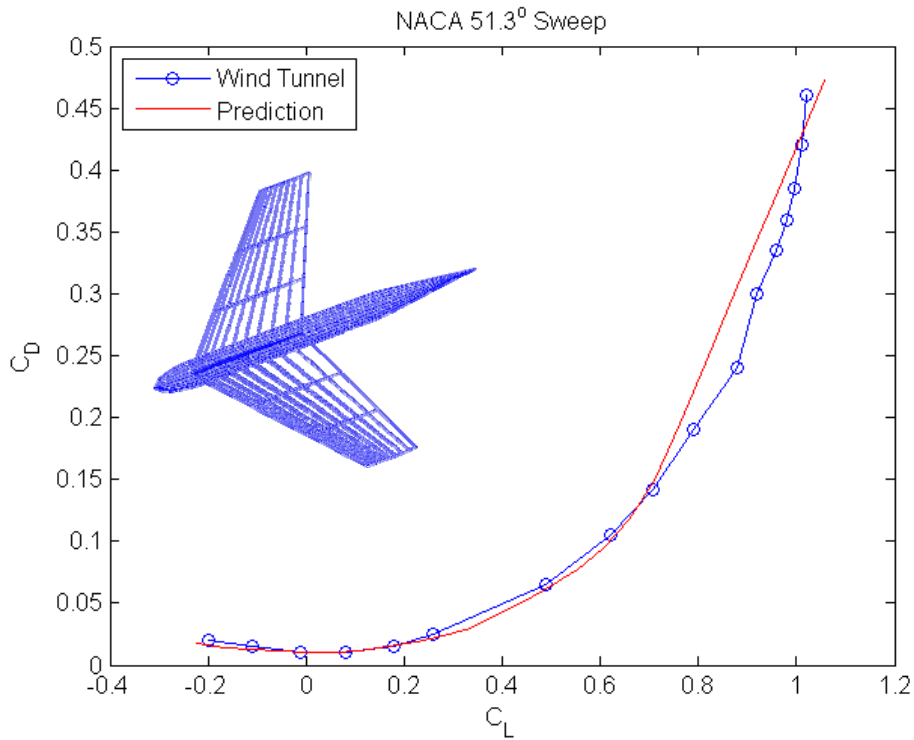


**Figure 3.16 Comparison of NACA RM L8H20, 51.3° swept wing and the predicted drag polar. As in Figure 3.15, there is a sharp drag rise in the predicted polar that is an unphysical stall representation.**

### *3.3.1. 777-200ER Comparison with Delta Drag Method*

It is important to note that the drag polars and the geometry for the Boeing 777-200ER are not from the Boeing Company, and the predictions herein are based on publicly available geometry and information. There are known uncertainties in the geometric data used, and these results are intended as a comparison between two methods and not to accurately estimate the drag polar for the 777-200ER.

The Delta Method is a purely empirical method based on a database of preceding aircraft. The method was developed in 1978 by Lockheed for NASA. The method has similar profile drag correlations as the method discussed here; however, the remainder of the method is largely different. The drag buildup is separated into different components, and the induced drag is treated as if the aircraft has an elliptical lift distribution with a separate empirical correction term added. For complete details of the Delta Method the reader is encouraged to see reference [7].

The accuracy of the Delta Drag Method for commercial transport aircraft is unknown as the documentation only states that the Lockheed L-1011 TriStar was used in the aircraft database. All flight test and wind tunnel comparisons in the literature are for supersonic or military aircraft. The estimates of the two methods are shown in Figure 3.17, and they are the same near the cruise lift coefficient,  $C_L=0.5$ . However, at lift coefficients away from the cruise lift coefficient the Delta Method predicts drag up to 18% less than this method.

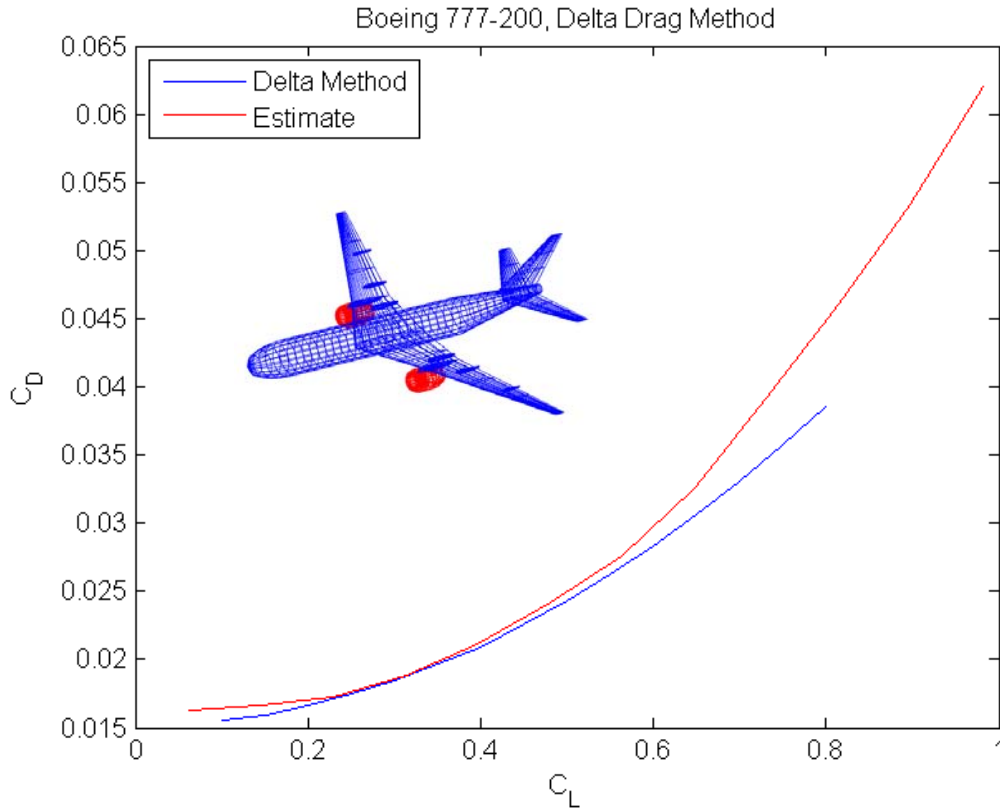


**Figure 3.17 Comparison of the predicted drag polar and the drag polar predicted by the Delta Drag Method [7] for the Boeing 777-200ER at Mach 0.3 and 10,000ft altitude based on publicly available geometry.**

### 3.4. Drag Polars for High-Lift Devices Deployed

The high-lift devices accounted for in this method are both leading-edge slats and trailing-edge flaps. The high-lift drag polars are computed using the same method as for clean aircraft except the off-design drag term is removed, and four additional terms are added. The four new terms correspond to (1) a flap vortex drag term,  $K^2 \Delta C_{L0}^2$ , (2) a flap profile drag term, (3) a slat drag term, and (4) a landing gear drag term. The method is shown in Equation 3.12, and each of the new drag components will be discussed in this section.

$$C_D = C_{Dp} + C_{Dind} + C_{De} + C_{Dint} + K^2 \Delta C_{L0}^2 + C_{Dflap} + C_{Dslat} + C_{Dgear} \quad 3.12$$

### 3.4.1. Drag Components from Clean Configuration

The initial components of the high-lift drag polar are all the same as for the clean configuration, so the profile drag, induced drag, excrescence drag, and interference drag all carry over. The only drag component that does not carry over from the clean configuration is the  $\Delta C_D$  term that is correlated to wing sweep. This means that the only term in the high-lift drag prediction that varies with lift is the induced drag. Accordingly, in violation of common practice, the high-lift drag polars have a higher Oswald Efficiency Factor than the clean drag polars. This means the drag polars rise less sharply with lift than do the clean configuration drag polars.

### 3.4.2. Vortex Drag Term

The  $K^2 \Delta C_{L0}^2$  term is computed in two parts. The  $\Delta C_{L0}^2$  is the additional lift generated at zero angle of attack due to flap and slat deployment. This term assumes that the flaps and slats are full span. The  $K^2$  term is a correction which adjusts for part-span flaps and slats.

The first effect to account for when computing  $K$  is the interference between the fuselage and the flaps. The method to do this is to fictitiously decrease the span fraction for the inboard edge of the inboard trailing edge flap, or to decrease the variable  $Y1$ .  $Y1$  is increased or decreased by an amount  $\Delta s$  which is an empirical function of the fraction of the fuselage height that the wing is above the fuselage centerline (value is negative if the wing is below the centerline), and the fraction of the wing span occupied by the fuselage, and is computed with Equation 3.13. The geometric ratios used in Equation 3.13 are presented in Figure 3.18. The fictitiously modified span fraction of the flap,  $b_i$  is computed in Equation 3.14 as the sum of inboard span fraction and the fictitious span change [29].

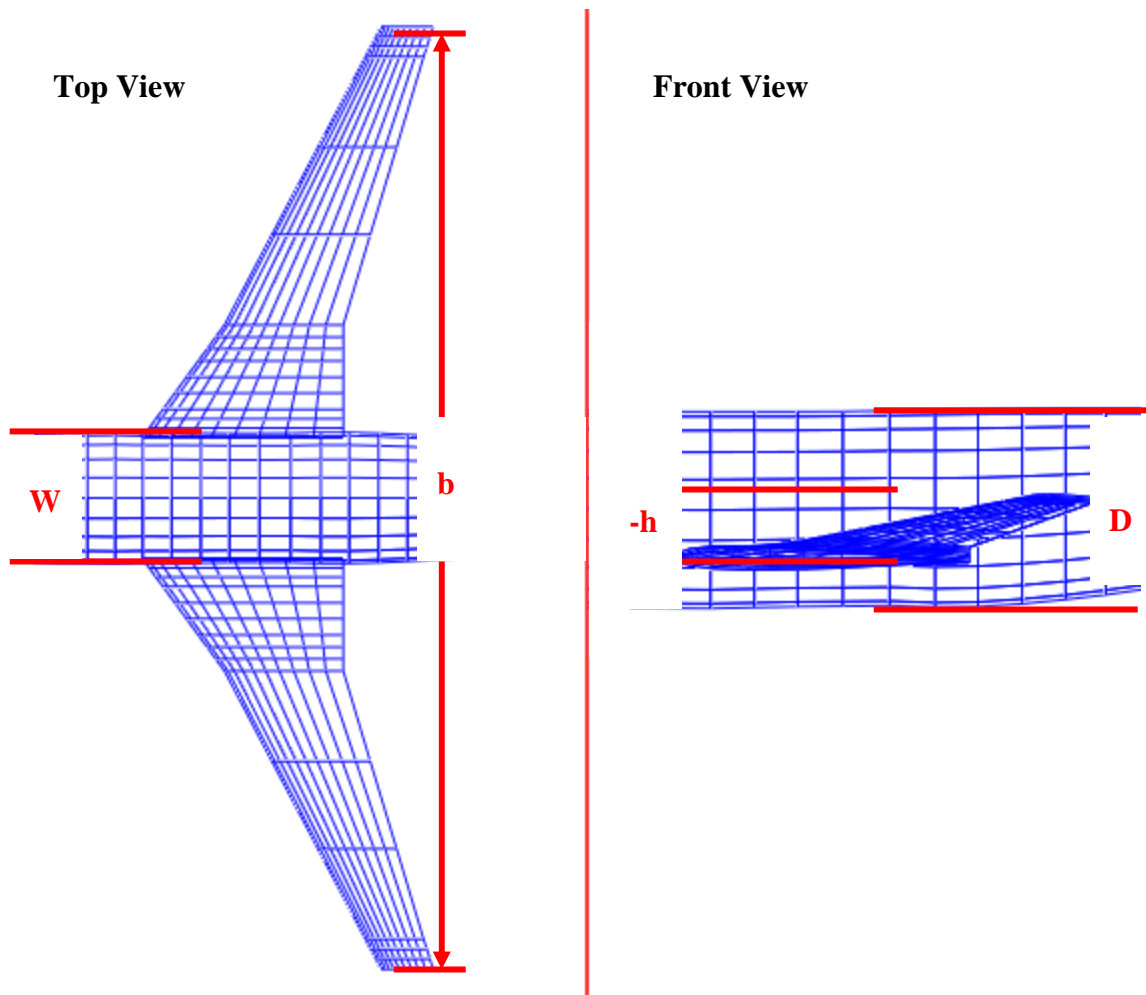


Figure 3.18 Geometric definitions for fuselage interference effects on flaps.

$$\Delta s = \left[ 0.25 + 0.3 \left( \frac{h}{D} \right) \right] \frac{W}{b} \quad 3.13$$

$$b_i = Y1 + \Delta s \quad 3.14$$

The other parameters needed to predict  $K$  are the outboard span fraction where the outboard flaps end and the aspect ratio. The outboard span fraction,  $b_o$ , is the same value as the input parameter  $Y4$ . The three parameters,  $b_i$ ,  $b_f$ , and the aspect ratio,  $AR$ , can be used with the empirical function shown from reference [28] to compute  $K$ . The empirical function assumes the flaps are ungapped, that they are continuous from  $b_i$  to  $b_o$ , which is not generally true for commercial aircraft. However, for commercial aircraft the gaps are usually small, and may contain an engine pylon, so this correlation is still considered valid. Any errors in this

correlation will be corrected in the empirical function for the flap profile drag,  $C_{Dflap}$ , discussed later.

The  $\Delta C_{L0}$  term is the additional lift at zero angle of attack generated by the flap and slat deployment at the trailing edge of the wing. ESDU has a catalog of articles, references [31]-[35], dedicated to predicting the additional lift at zero angle of attack. Some of the articles require numerous parameters that are beyond the scope of this model and poor predictions resulted from using approximate values. The final method uses the ESDU method for leading edge slats, reference [31], and treats the trailing-edge flap as a plain flap using the ESDU method in reference [32]. However, the ESDU plain flap method has been implemented in conjunction with an effectiveness correlation from Torenbeek which is an empirical function of the deflection angle and chord fraction [9]. Accordingly, the total change in lift coefficient at zero angle of attack is the sum of the change in lift coefficient caused by the flaps and the slats, multiplied by the efficiency factor in Torenbeek, which is presented in Equation 3.15.

$$\Delta C_{L0} = \eta_f [\Delta C_{L-le} + \Delta C_{L-te}] \quad 3.15$$

The first step in predicting the additional lift of the flaps and the slats is to account for the chord extension. An approximation made is that entire chord of the flap and slat is extended from the wing, this approximation is probably decent for flaps but likely in error for slats. The extended chord is the sum of the wing chord plus the chords of the flap and slats if they are extended, Equation 3.16. Additional lift at zero angle of attack is added if the slats are gapped, for most aircraft during takeoff the slats are sealed, but for landing they are gapped. It appears for matching test data that  $19.2^\circ$  slat deflection provides a good breakpoint between sealed and gapped leading edge devices. Accordingly, the additional lift from a gapped slat system,  $\Delta C_{L-le2}$ , is zero if the slat deflection is less than  $19.2^\circ$  and 0.03 if greater, Equation 3.17. All of these components can be combined with the slat deflection angle,  $\delta_{le}$ , in Equation 3.18 to estimate the total additional lift from the leading edge slat.

$$c' = c + c_f + c_{le} \quad (\text{if both flaps and leading edges are deployed}) \quad 3.16$$

$$\Delta C_{L-le2} = \begin{cases} 0 & \delta_{le} < 19.2^\circ \\ 0.03 & \delta_{le} \geq 19.2^\circ \end{cases} \quad 3.17$$

$$\Delta C_{L-te} = -2.70 \frac{c'}{c} \delta_{le} \frac{\pi}{180} \left[ \cos^{-1} \left( 1 - 2 \frac{c_{le}}{c'} \right) - \sqrt{1 - \left( 1 - 2 \frac{c_{le}}{c'} \right)^2} \right] + \Delta C_{L-le2} \quad 3.18$$

The change in lift at zero angle of attack due to trailing-edge device deployment,  $\Delta C_{L-te}$ , is defined in Equation 3.19. The equation is very similar in form to the leading edge lift with the exception of an empirical efficiency factor,  $J_p$ . The definition of  $J_p$  and the derivation of the additional trailing-edge lift at a zero angle of attack are found in reference [32].

$$\Delta C_{L-te} = 2 \frac{c'}{c} J_p \delta_f \frac{\pi}{180} \left[ \pi - \cos^{-1} \left( 2 \frac{c_f}{c'} - 1 \right) + \sqrt{1 - \left( 2 \frac{c_f}{c'} - 1 \right)^2} \right] \quad 3.19$$

The flap efficiency,  $\eta_f$ , can then be estimated from Torenbeek's correlations. The one used in the model is for an average double-slotted flap and it is shown in Figure 3.19.

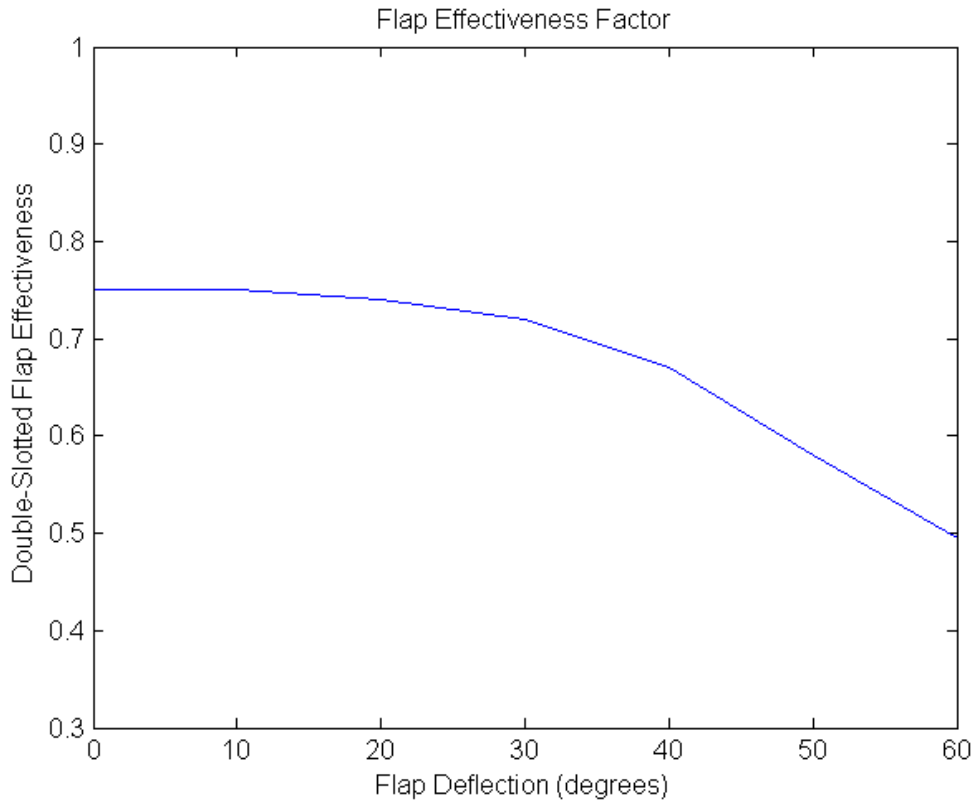


**Figure 3.19: Flap effectiveness empirical function for double-slotted flaps from Torenbeek [9].**

### 3.4.3. Flap Profile Drag

The flap profile drag is another empirical function. The parameters are flap deflection angle, flap chord ratio, and the wing quarter chord sweep. The empirical function interpolates the flap deflection angle into the curve shown in Figure 3.20, and then scales it by the empirical function presented in Equation 3.20.

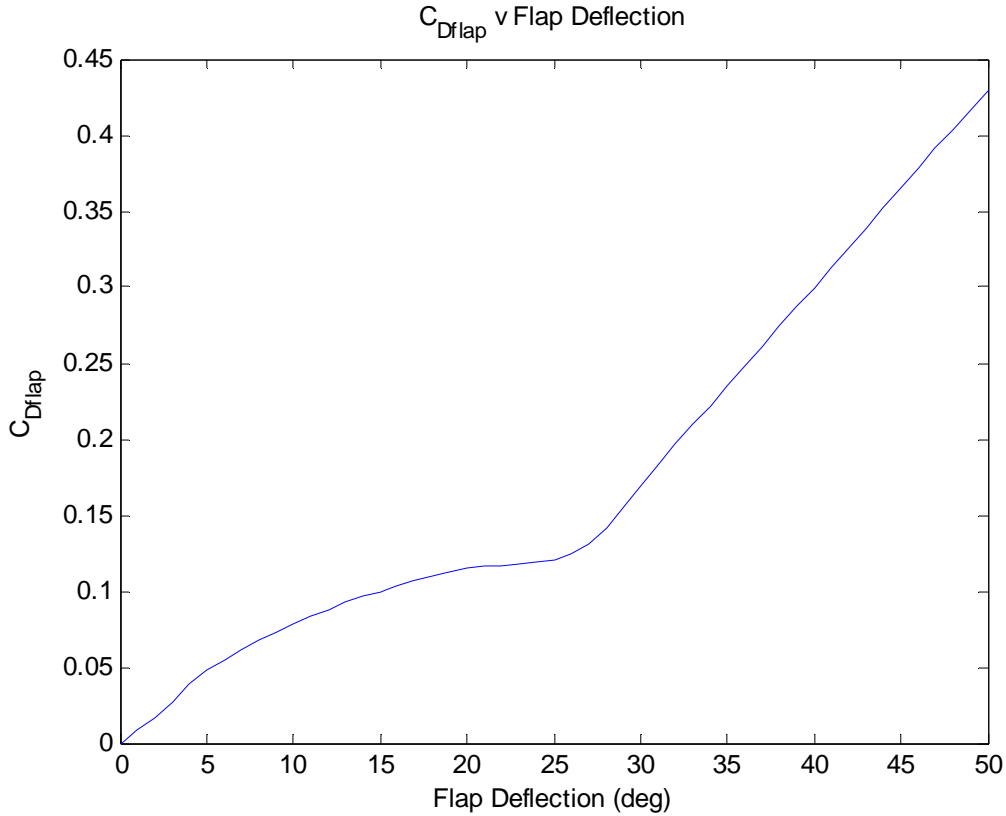


**Figure 3.20: Raw  $C_{Dflap}$  to be used in Equation 3.20.**

$$C_{Dflap} = C_{Dflap}(\delta_{flap}) \cdot \cos(\Lambda_{0.25c}) \cdot \left(\frac{c_f}{c}\right)^{0.3} \quad 3.20$$

As a comparison the actual flap profile drag for an aircraft with a quarter chord sweep angle of  $30^\circ$  and a chord fraction  $c_f/c=0.25$  is shown in Figure 3.21 for this method, Schaufele's method, and two ESDU methods. The method herein has more profile drag than the other methods, which likely means the flap vortex drag is in error. Accordingly, both the flap vortex

drag and flap profile drag may be bookkeeping drag in a way that is inconsistent with the definitions; nonetheless the total drag is estimated correctly. As a point of note, when multiple flaps of different chords are used on the same airplane the area-weighted average of the flap chords should be used for the flap profile drag estimate.

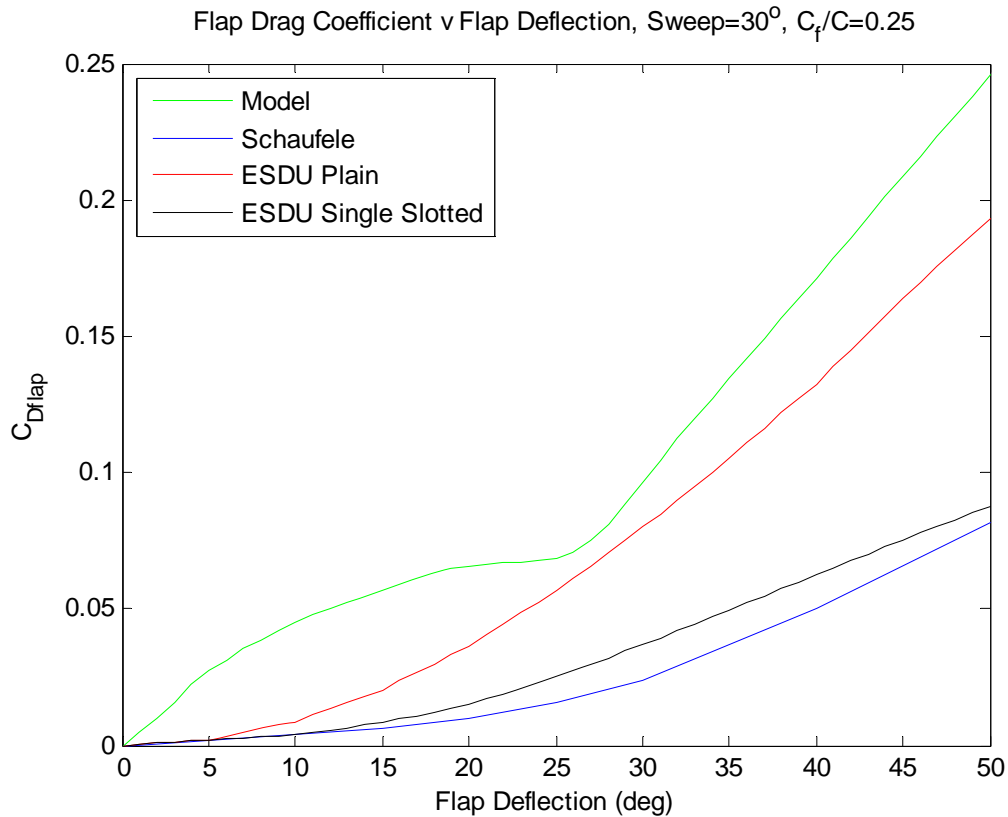


**Figure 3.21: Sample curve of  $C_{D_{flap}}$  v Flap Deflection for an aircraft with  $30^\circ$  of sweep and a flap chord fraction of 0.25. Compared to results from Schaufele [10] and ESDU [32],[34].**

#### 3.4.4. Slat Drag

There are three confounding phenomena that occur from slat deployment. The first is that the deployment increases the camber of the wing and enables the wing to decrease its angle of attack, which reduces drag. The second, especially for gapped leading edge devices, is that the slat helps to maintain flow attachment over the wing, which decreases drag. The third is that deployment of the slat increases the drag due to additional wetted area, local flow separation behind the slat, and generally makes the wing a less clean surface.

Equation 3.21 shows an empirically generated slat deployment drag coefficient. The first term, accounts for the decrease in angle of attack of the wing and reduced flow separation and is proportional to the additional lift generated by the flaps at zero angle of attack. The second term accounts for the drag penalty of altering the clean wing.  $S_{le}$  is the reference area of the wing covered by the slats, is defined differently from other methods where  $S_{le}$  is normally all of the wing area effected by the slats.

The correlation used assumes the slats are sealed for deflections below  $19.13^\circ$  and are gapped for higher deflections. Although flaps maybe sealed between  $10-17^\circ$  and gapped around  $20-35^\circ$  the  $19.13^\circ$  does not have to change, it represents a good mean value.

$$C_{Dslat} = -0.07 \cdot \Delta C_{L0} + 0.15 \left( \frac{S_{le}}{S_{ref}} \right) \left( \frac{\delta_{le}}{19.13} \right) \quad 3.21$$

Very little data is available for the drag increment for slat deployment. One of the few is Schaufele [10] which says a good average value for slat drag is 0.006.

### 3.4.5. Landing Gear Deployment Drag

The landing gear drag prediction method is the simple correlation from Schaufele [10]. The drag coefficient is linearly related to the flap deflection angle, as presented in Figure 3.22.

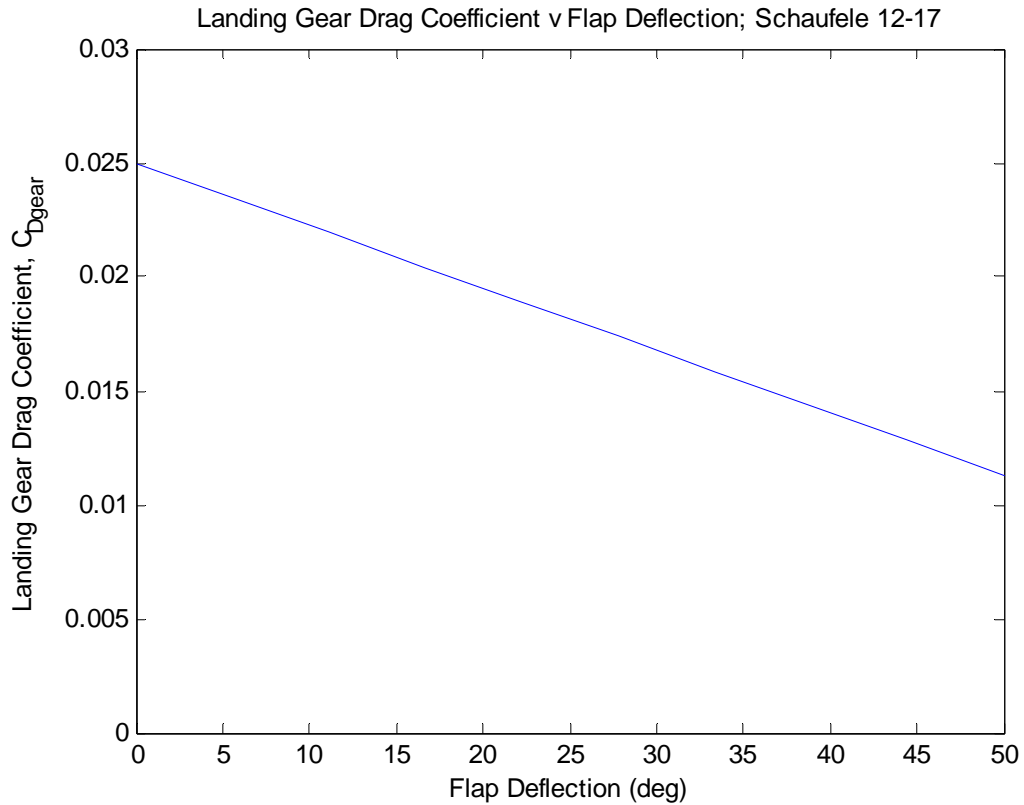


**Figure 3.22: Landing gear drag coefficient prediction [10].**

The drag predicted by Schaufele’s method is based on data from the DC-9. Other aircraft with multiple wheels on each truck would have a different drag coefficient; however, it appears that the drag coefficient will still vary linearly with the flap deflection angle. For a much more sophisticated landing gear drag prediction method the reader is encouraged to see reference [36].

### 3.5. Method Results – Flaps Deployed

The results for flaps deployed are not as accurate as the results for the clean aircraft. The maximum error encountered for any predicted point on any of the drag polars was 11 percent. However, the average error is about 3%. The results of the Boeing 727-100, 737-700, 747-100, and a NASA wind tunnel model are presented herein. In all of the plots, the lines represent the flight test data or wind tunnel data, and the asterisks represent the estimates of this low-speed estimation method.

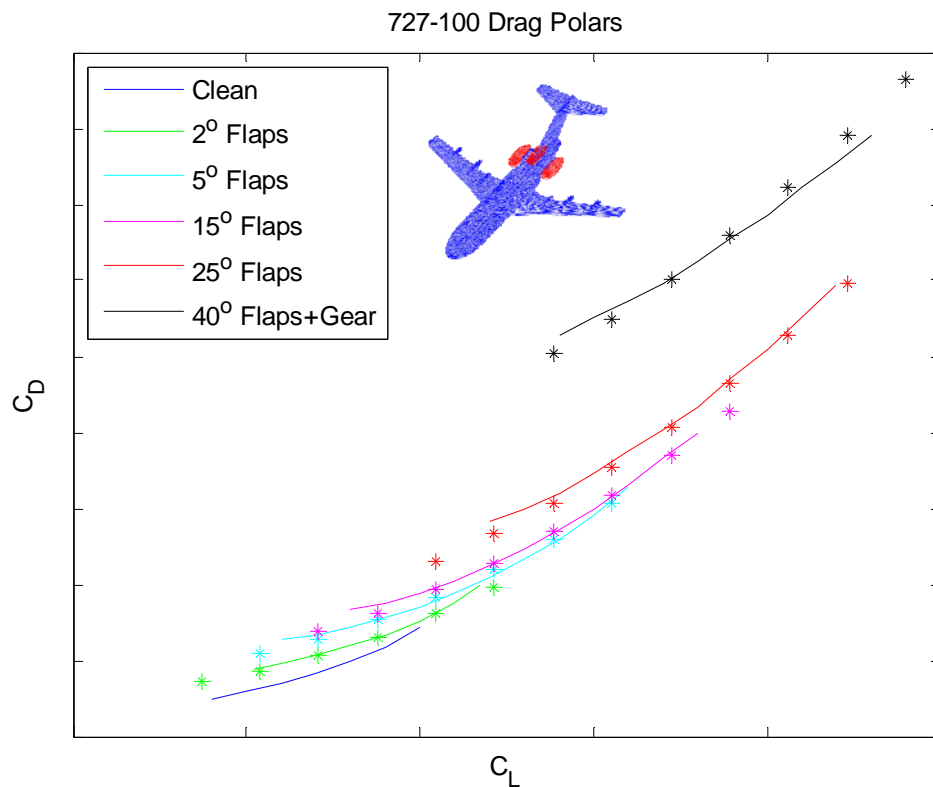


Figure 3.23 Predicted drag polars for the 727-100 for 5 different flap settings. Lines represent flight test data and overlaid asterisks represent the predictions.

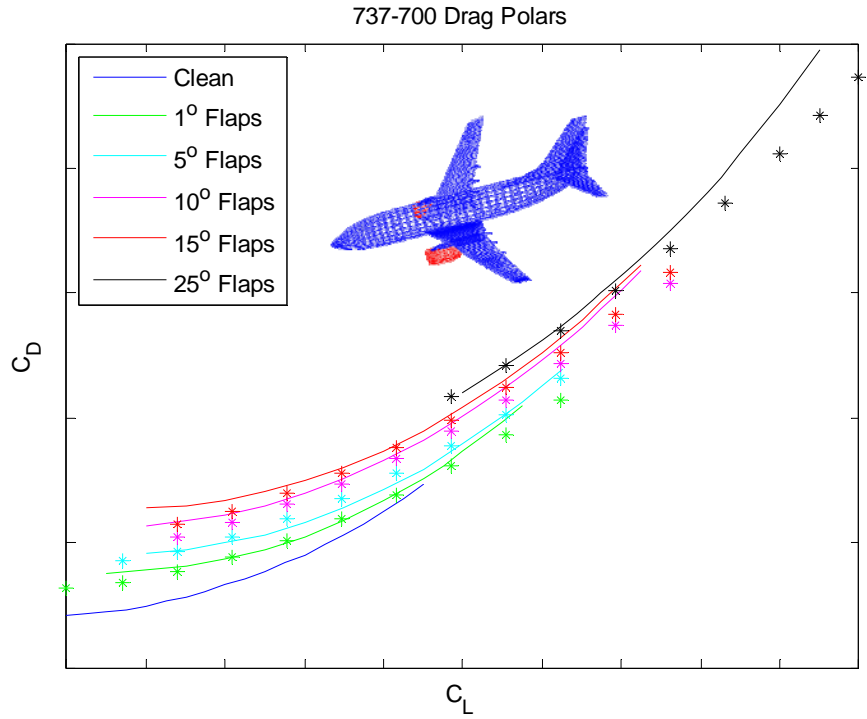


Figure 3.24 Predicted drag polars for the 737-700 for 5 different flap settings. Lines represent flight test data and overlaid asterisks represent the predictions.

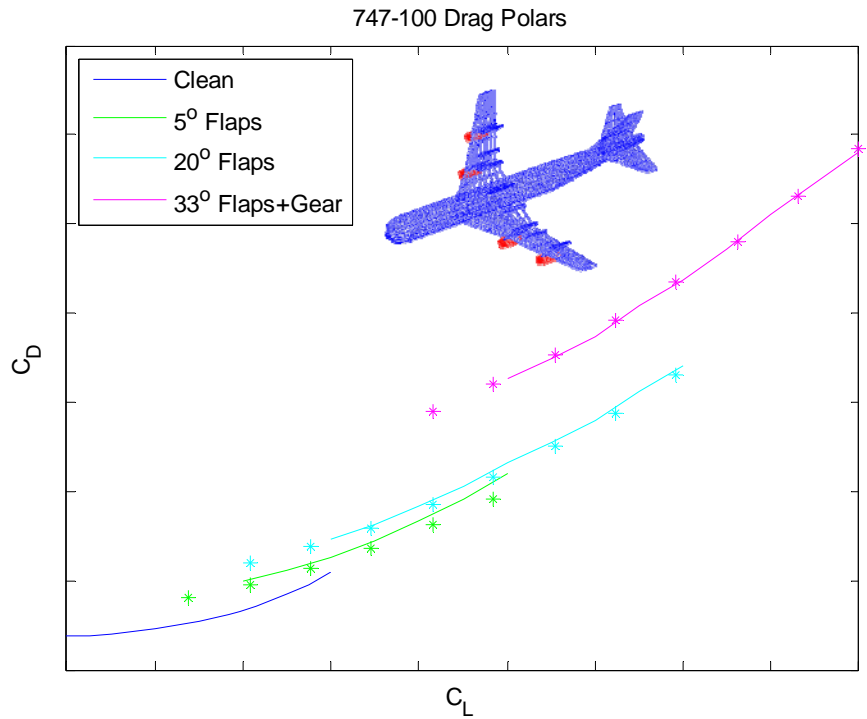
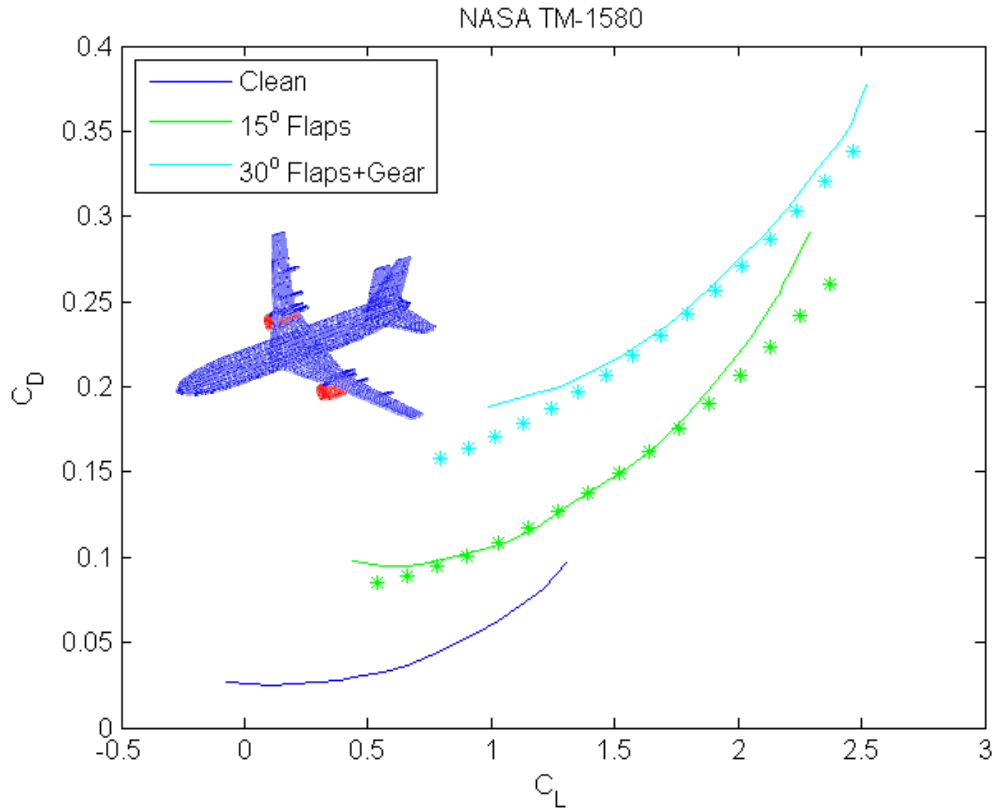


Figure 3.25 Predicted drag polars for the 747-100 for 3 different flap settings. Lines represent flight test data and overlaid asterisks represent the predictions.



**Figure 3.26 Predicted drag polars for NASA TM-1580, a subsonic commercial transport wind tunnel model. Lines represent the wind tunnel test data and overlaid asterisks represent the predictions [37].**

### 3.6. Lift v Angle of Attack and $C_{L_{max}}$ for Clean Configuration

The lift curve prediction method is a hybrid method that uses parts of Schaufele's method [10] and results of the vortex lattice code, AVL. Schaufele's method empirically predicts the lift curve slope  $dC_L/d\alpha$  as a function of sweep and aspect ratio. With the slope known, it is necessary to find a point on the curve, and this point is estimated by assuming  $(L/D)_{max}$  occurs at an angle of attack between zero and two degrees. This is a good estimate as there is a limitation on fuselage angle of attack set by the push-cart force a flight crew can exert, so during cruise the fuselage inclination needs to be less than two degrees.

AVL computes the potential flow lift curve slope and lift at zero angle of attack based on the wing and horizontal tail configurations and camber. Both methods produce surprisingly similar results at low Mach numbers and low angles of attack. However, AVL offers two

improvements at low angle of attack that Schaufele's method does not. First, AVL computes the effect of the horizontal tail on the lift curve slope; whereas, Schaufele scales the lift curve slope by 1.08. Second, AVL accounts for changes in Mach number up to about Mach 0.7 by applying the Prandtl-Glauert correction. Accordingly, to predict  $C_L$  v  $\alpha$  at low angles of attack  $dC_L/d\alpha$  and  $C_{L@\alpha=0}$  are taken from AVL's predictions.

At high angles of attack, Schaufele's method predicts the lift curve much more accurately than AVL. This is because AVL is a potential flow solution and no viscous effects are predicted, so the lift curve remains linear. Schaufele's method has a simple correlation for  $C_{Lmax}$  and an easy method to adjust the lift curve to account for non-linearities. It is essential that the wing tip stall after the main wing to prevent loss of lateral control since the ailerons are at or near the wing tips. Accordingly,  $C_{Lmax}$  can be predicted by estimating  $C_{Lmax-tip}$  from the general behavior of supercritical airfoils.  $C_{Lmax}$  for the wing can then be predicted as a function of sweep and the wingtip  $C_{Lmax}$ . If the Mach number is greater than 0.25 Schaufele also provides an adjustment to account for the loss of lift at higher speeds as a function of Mach number. These three correlations (left)  $C_{Lmax-tip}$  as a function of wingtip thickness to chord ratio, (center) ratio of airplane  $C_{Lmax}$  to  $C_{Lmax-tip}$  as a function of wing sweep, and (right) the ratio of  $C_{Lmax}$  to  $C_{Lmax-low-speed}$  as a function of Mach number are plotted in Figure 3.27.

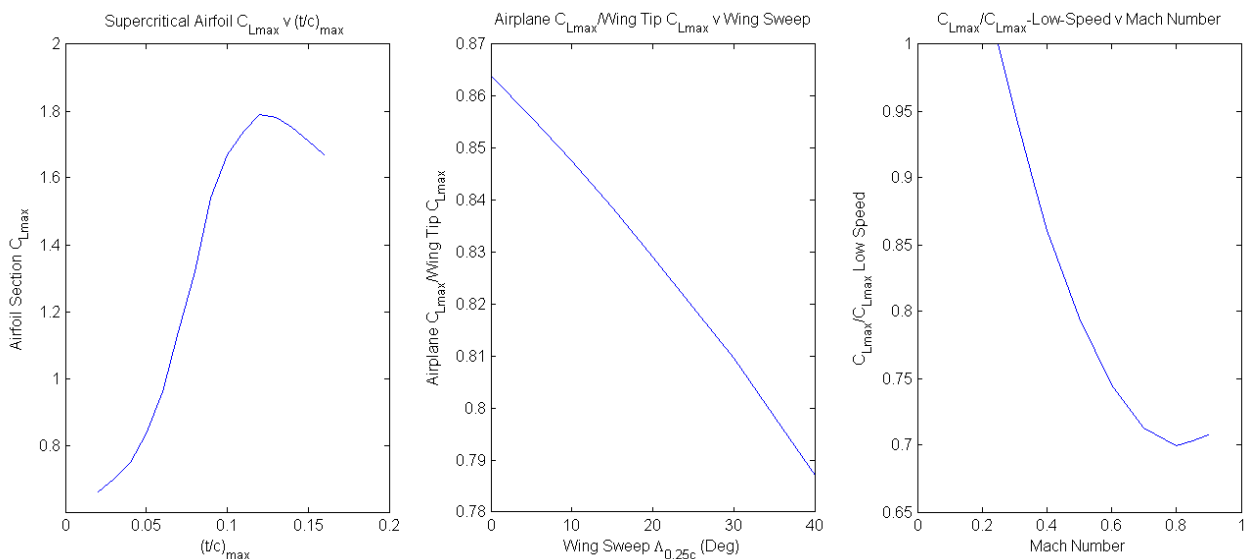


**Figure 3.27: Schaufele's method of predicting  $C_{Lmax}$  for a clean wing. Left,  $C_{Lmax-tip}$  as a function of wingtip thickness to chord ratio, center, ratio of airplane  $C_{Lmax}$  to  $C_{Lmax-tip}$  as a function of wing sweep, and right, the ratio of  $C_{Lmax}$  to  $C_{Lmax-low-speed}$  as a function of Mach number [10].**

Once  $C_{L_{max}}$  is known Schaufele provides a simple method for predicting the portion of the lift curve affected by viscous separation. The method assumes the lift curve is linear until  $0.9 \cdot C_{L_{max}}$  and then will show non-linearities. The angle of attack for  $C_{L_{max}}$  is predicted by assuming the lift curve slope is linear through  $C_{L_{max}}$ , and then the angle of attack predicted for  $C_{L_{max}}$  with the linear method is increased by two degrees. Accordingly, a parabola can be fit to the upper portion of the lift curve by placing its maxima at  $C_{L_{max}}$  located at the linear angle of attack plus two degrees, and requiring that the parabola is tangent to the linear portion of the lift curve slope at  $0.9 \cdot C_{L_{max}}$ .

The predictions of this hybrid method are shown for the Boeing 737-700 at low-speed in Figure 3.28 and for a NASA wind tunnel model at Mach 0.55 in Figure 3.29.

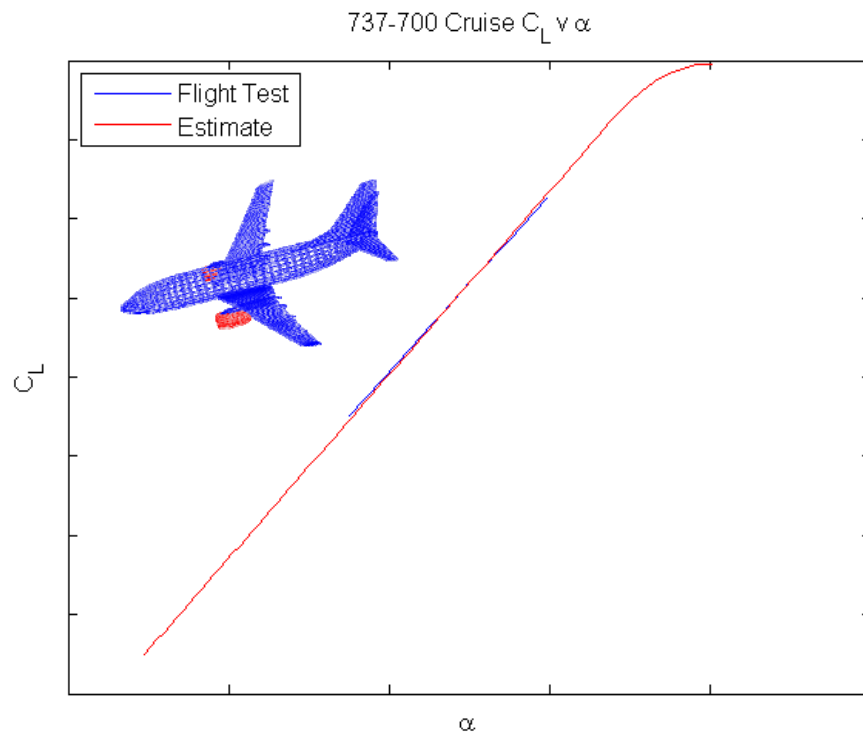


**Figure 3.28:** Comparison of the predicted lift curve for the 737-700 and flight test data at low speed.

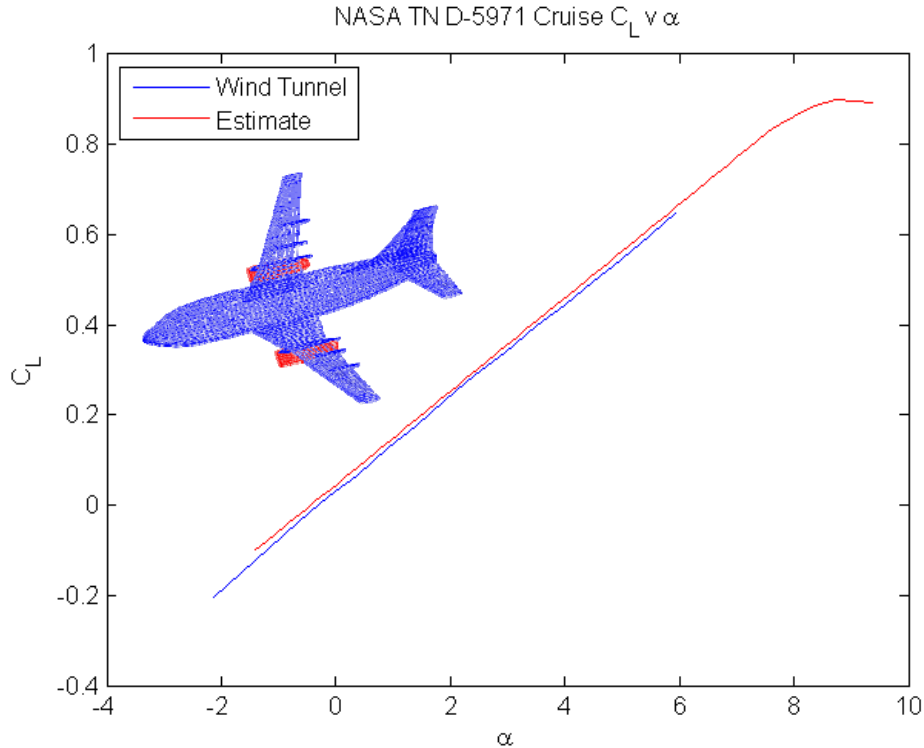


**Figure 3.29: Comparison of the predicted lift curve and wind tunnel data for a NASA model at  $M=0.55$  [19].**

### 3.7. Lift v Angle of Attack and $C_{Lmax}$ Predictions for High-Lift Devices

#### 3.7.1. $C_{Lmax}$ Data for Current Aircraft

The first step in estimating the lift curve,  $C_L$  v angle of attack, for the high-lift configurations is to predict the maximum lift coefficient. The maximum lift coefficient for multi-element flap configurations is quite challenging to estimate accurately. There are numerous parameters, such as leading edge radius, gap heights between flaps and slats, and the size of high-lift device supporting structure which all impact the maximum lift. The method described herein reduces a large collection of parameters to average values in order to predict  $C_{Lmax}$  from the parameters used in the low-speed aerodynamics model. The average values represent the best estimate of the values to match published  $C_{Lmax}$  values for aircraft and wind tunnel results. There are two

public sources of  $C_{Lmax}$  values, one is a published list from the Boeing Company [38], and the other is the FAA’s Integrated Noise Model (INM).

Airplane	<b>B-47/B-52</b>	<b>367-80</b>	<b>727</b>	<b>747</b>	<b>767</b>	<b>777</b>	<b>737-700</b>
Boeing $C_{Lstall}$	1.8	1.78	2.79	2.55	2.45	2.57	2.78
INM $C_{Lmax}$			2.83	2.22		2.53	2.44

**Table 3.4: Comparison between published values of  $C_{Lstall}$  and the  $C_{Lmax}$  values computed from the Integrated Noise Model database in the landing configuration for various Boeing airplanes [38].**

An important difference between  $C_{Lstall}$  and  $C_{Lmax}$  is that  $C_{Lstall}$  is an FAA defined value that is the minimum airspeed flyable to a stall with a rate of approach to the stall of one knot per second. This value is typically 11% higher than the unaccelerated 1-g  $C_{Lmax}$  [17]. This likely accounts for some of the discrepancies between the two data sources. The INM values were selected as the  $C_{Lmax}$  values to calibrate the low-speed aerodynamics method as the goal of this work is to estimate noise.

### 3.7.2. Computing $C_{Lmax}$

The  $C_{Lmax}$  prediction for the high-lift configuration is built on a collection of ESDU articles [31]-[35]. However, because the aircraft model defines parameters differently than in the ESDU articles, and many of the parameters are not included a variety of alterations and approximations have been made. The section will present an outline of the ESDU method and will present the modifications and approximations made to the method. The basis for the prediction of the maximum lift coefficient of the wing with flap and slat deflection is to compute a change in  $C_{Lmax}$  caused by the leading and trailing edge devices and add them to the clean wing  $C_{Lmax}$ . The clean wing maximum lift coefficient is estimated using Schaufele’s method as discussed in Section 3.6. The additional maximum lift coefficient from the trailing edge flaps,  $\Delta C_{Lmax-te}$ , will be presented in first, followed by the additional maximum lift coefficient from the leading edge slats,  $\Delta C_{Lmax-le}$ . The three parts of the maximum lift coefficient are then added as shown in Equation 3.22.

$$C_{Lmax} = C_{Lmax-clean} + \Delta C_{Lmax-te} + \Delta C_{Lmax-le} \quad 3.22$$

### 3.7.3. Computing $\Delta C_{Lmax}$ due to Trailing-Edge Flaps

To predict  $\Delta C_{Lmax-te}$  the trailing edge flaps are treated as double-slotted which provides a good representation of the flap systems a modern commercial aircraft. All of the changes to the maximum lift coefficients are done with two-dimensional airfoils and then empirically correlated to a change in the three-dimensional maximum lift coefficient. Initially,  $\Delta C_{Lmax-2D}$  is computed for a 2-dimensional airfoil with flaps and then another empirical method is used to correlate  $\Delta C_{Lmax-2D}$  to  $\Delta C_{Lmax-te}$  for a 3-dimensional wing.

The full equation to compute  $\Delta C_{Lmax-2D}$  is shown in Equation 3.23 which is significantly modified from reference [35]. The first term in the equation accounts for the additional maximum lift due to chord extension and is a function of the two-dimensional maximum lift coefficient defined in Equation 3.24, the extended flap chord,  $c'$ , defined in Equation 3.16, and the flap deflection angle,  $\delta_f$ . The second and third terms of the equation account for the additional lift of the double slotted flaps. The  $\Delta C_{L1}$  and  $\Delta C_{L2}$  terms are empirical functions of the chord fractions of the two flap segments and their deflection angles, and they are unchanged from reference [35]. The first flap segment is treated as having seventy percent of the flap chord and the second flap segment is treated as having thirty-five percent of the flap chord. The deflection angle of each flap segment is assumed to be the same, and equal to the deflection of the flap itself. There are two remaining empirical corrections in Equation 3.23, the first,  $K_{t1}$ , is defined in Figure 3.30 as a function of flap deflection, and has been significantly modified from the original function. The other parameter,  $J_{t1}$  remains unaltered.

$$\Delta C_{Lmax-te-2D} = 0.1C_{Lmax-2D} \left( 1 - \frac{c}{c'} \right) [1 - \sin(\delta_f)] + 1.7K_{t1}J_{t1}\Delta C_{L1} + 0.561\Delta C_{L2} \quad 3.23$$

$$C_{Lmax-2D} = \frac{C_{Lmax-clean}}{\cos(\Lambda_{0.25c})} \quad 3.24$$

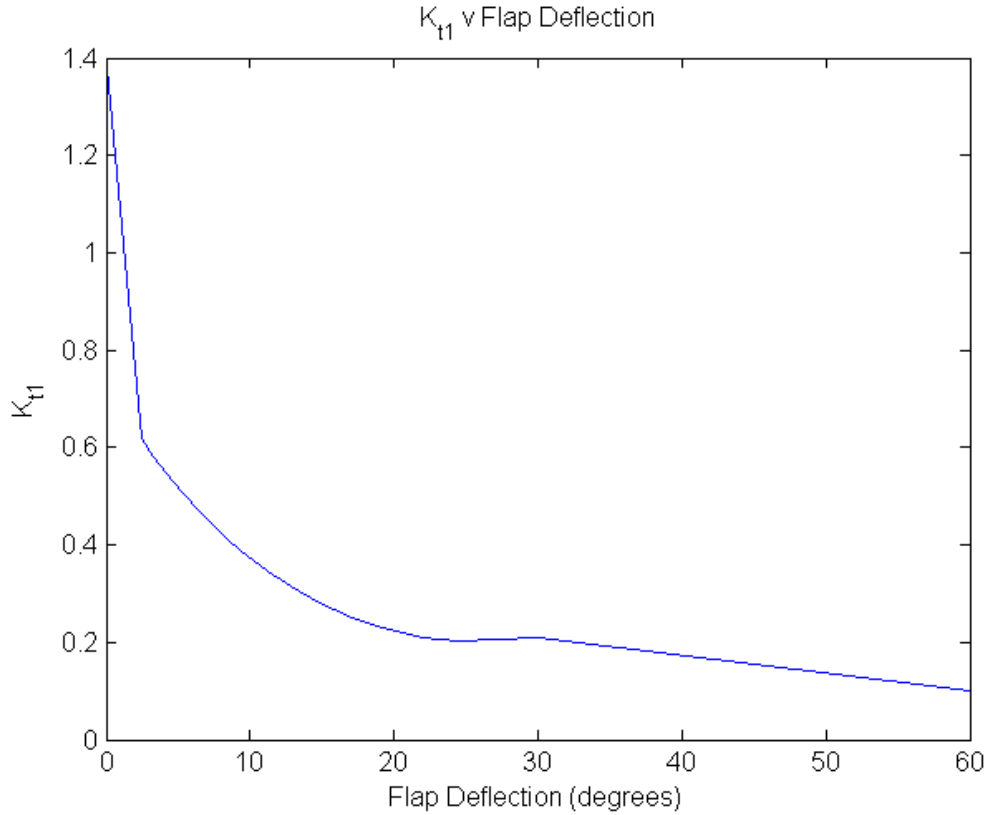


**Figure 3.30: Empirical function for  $K_{t1}$  used in predicting the additional maximum lift of a trailing edge flap.**

To compute the three-dimensional  $\Delta C_{L_{\max-te}}$  from the two-dimensional value computed in Equation 3.23, a method based on reference [39] was used. Equation 3.25 shows the final form of the method including the approximations made.

$$\Delta C_{L_{\max-te}} = 0.1683 \cos(\Lambda_{0.25c}) \log_{10} [\text{Re} \cdot \cos^2(\Lambda_{0.25c})] \frac{\Delta C_{L_{\max-te-2D}}(\Phi_o - \Phi_i)}{\mu_p} \quad 3.25$$

The parameter  $\mu_p$  is an empirical function of the wing taper ratio, and the parameters  $\Phi_i$  and  $\Phi_o$  are empirical functions of the inboard and outboard flap span fractions. The empirical functions are unchanged from reference [39], assuming the center of pressure of the wing is located at forty percent of the chord.

### 3.7.4. Computing $\Delta C_{Lmax}$ due to Leading-Edge Slats

The process of computing the additional lift for leading edge slats is quite similar to the method for computing the additional lift of trailing edge flaps. First, the additional two-dimensional lift will be computed, and then it will be converted to the additional three-dimensional lift coefficient by an empirical adjustment.

The two-dimensional additional lift for slats is computed using Equation 3.26 which has been considerably modified from reference [31].  $K_s$ ,  $\delta_0$ , and  $K_l$  are empirical functions of the leading edge slat deflection angle,  $\delta_{le}$ , in degrees.  $K_s$  is presented in Equation 3.27,  $\delta_0$  is presented in Equation 3.28 and the empirical function for  $K_l$  is shown in Figure 3.31. The variable  $c'$  is defined in 3.16 and is the same value as used for trailing edge flaps. The parameter  $\delta_0$  is the slat setting at which no additional lift is generated. For sealed flaps,  $\delta_0$  should be zero and the slat will generate additional lift as soon as it is deployed; however, for gapped slats  $\delta_0$  should be 0.25. The method assumes that slat deflections less than 19.2 degrees are sealed and deflections above 19.2 degrees are gapped. This relationship does not have to hold strictly as that value corresponds to the intersection of the two curves.

$$\Delta C_{Lmax-le-2D} = K_s K_l \left( \frac{\pi \cdot \delta_{le}}{180} - \delta_0 \right) \sqrt{1 - \left( 1 - \frac{2c_{le}}{c'} \right)^2} \quad 3.26$$

$$K_s = \begin{cases} 0.2 & \delta_{le} < 19.2^\circ \\ 6.6 & \delta_{le} \geq 19.2^\circ \end{cases} \quad 3.27$$

$$\delta_0 = \begin{cases} 0 & \delta_{le} < 19.2^\circ \\ 0.25 & \delta_{le} \geq 19.2^\circ \end{cases} \quad 3.28$$

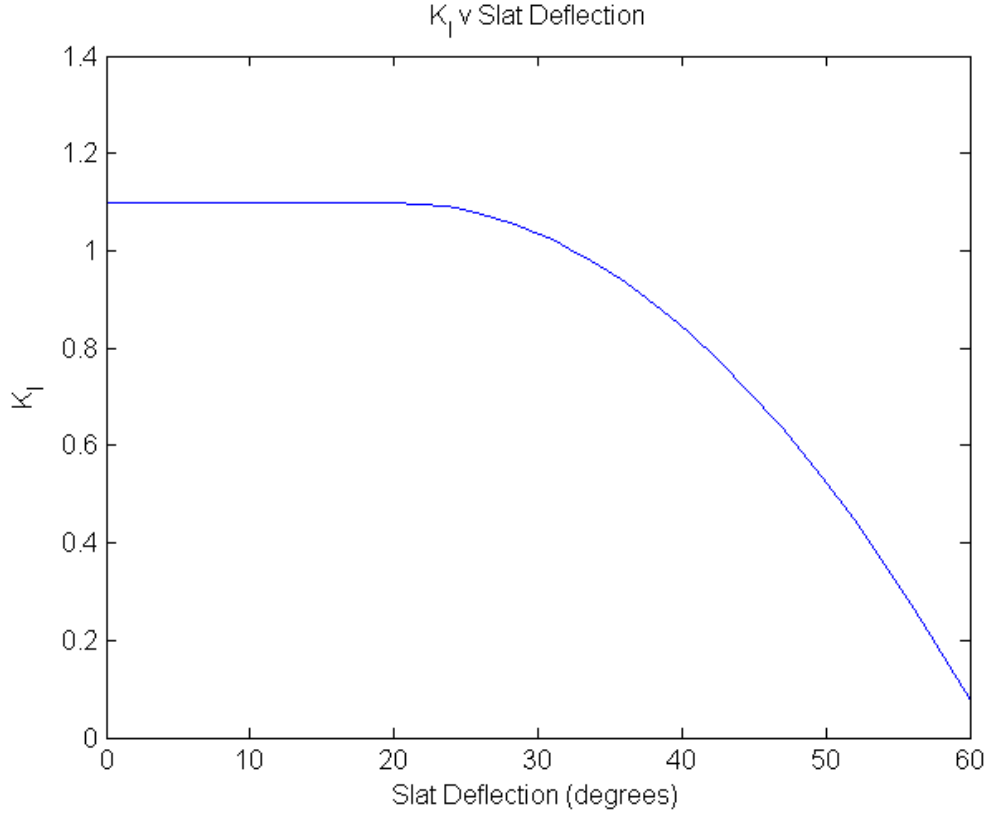


**Figure 3.31: Empirical function of the slat deflection angle for the parameter  $K_l$  modified from reference [31].**

To convert the two-dimensional  $\Delta C_{L_{\max-le-2D}}$  into a three-dimensional lift coefficient increment; Equation 3.29 is used [40]. The parameter  $\mu_p$  is the same value as used for the trailing edge flaps. The parameter  $\Psi_i$  is an empirical function of the inboard span fraction at which the leading edge slats begin. The slats are approximated for this function as being continuous from the inboard edge all the way to the wingtip. The empirical function for  $\Psi_i$  is taken directly from reference [40], assuming the wing center of pressure is located at forty percent of the chord.  $\Psi_o$  would be the equivalent parameter for the outboard slat span fraction and is computed in the same way.

$$\Delta C_{L_{\max-le}} = 0.153 \cos(\Lambda_{0.25c}) \cdot \log_{10} [\text{Re} \cdot \cos^2(\Lambda_{0.25c})] \frac{\Delta C_{L_{\max-le-2D}} \cdot \Psi_i}{\mu_p} \quad 3.29$$

### 3.7.5. $C_{Lmax}$ Prediction Results

The  $C_{Lmax}$  predictions for all of the cases show results within ten percent for all available data; however, in general the predictions are accurate to within five percent. The worst case error prediction accounts for an approach speed error of 4.5 knots, and as a point of reference airline transport pilots are only tested for the ability to maintain an aircraft speed to within  $\pm 5$  knots. Figure 3.32 shows the prediction of the maximum lift coefficients for the Boeing 737-700 compared to the data contained in the Integrated Noise Model. Figure 3.33 presents the percent error in maximum lift coefficient for a collection of the commercial transport configurations studied, and shows the general error of five percent and the maximum error of nine percent.

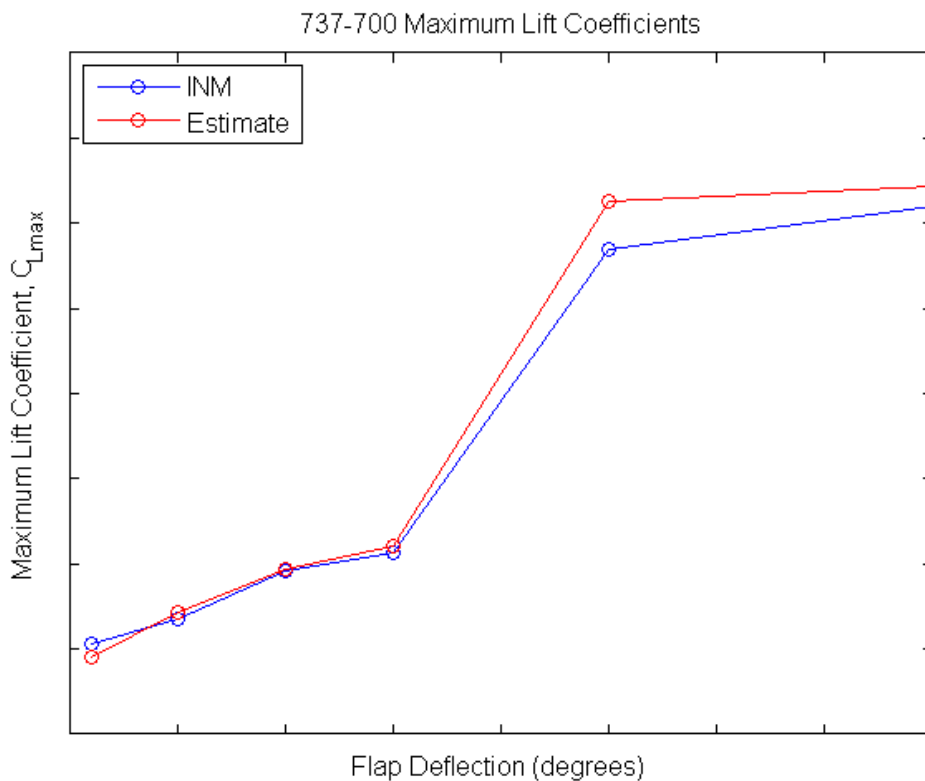


**Figure 3.32: Comparison between predicted maximum lift coefficient and the maximum lift coefficient contained in the Integrated Noise Model for the Boeing 737-700.**

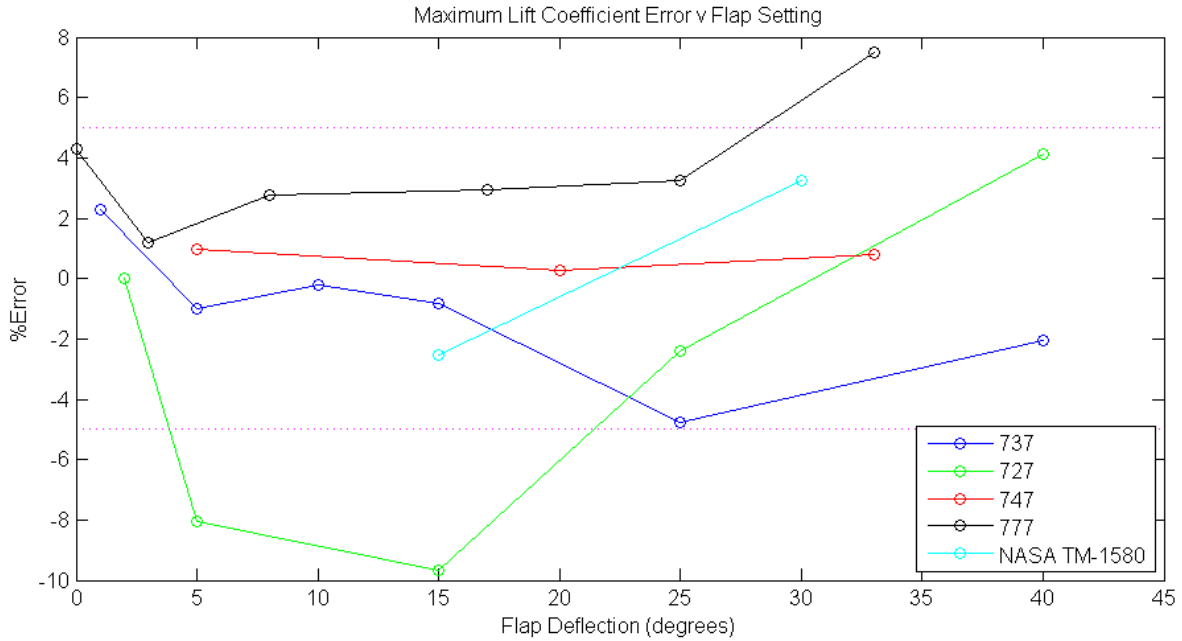


**Figure 3.33: Plot showing the percent error for the maximum lift coefficient predictions for many commercial aircraft configurations as a function of flap deflection angle.**

### 3.7.6. Predicting $C_L$ v Angle of Attack

Predicting the  $C_L$  v angle of attack curve for aircraft with flaps and slats deployed is much more complex than for aircraft in the clean configuration. The essential reason for this is that the lift curve slope is nonlinear at much lower angles of attack. In addition, there are numerous small details that have a large impact on the additional lift of flaps at zero angle of attack. Consequently, the vertical shift of the lift curve, the shape of the lift curve, and the slope of the lift curve must all be computed through a subset of the parameters needed to predict them. Attempts with simple potential flow models such as vortex lattice methods proved unreliable even for small flap deflections. The model developed is derived from reference [41], but the method has been substantially altered and in certain cases the parameters have been redefined.

The first step in predicting the  $C_L$  v  $\alpha$  curve is to predict the zero-lift angle of attack. This is an implicit equation that is solved iteratively for  $\alpha_{C_L=0}$ , and is shown in Equation 3.30.

$$\alpha_{C_L \alpha=0} \cos^N(-\alpha_{C_L=0}) = \frac{-C_{L\alpha=0}}{a \frac{180}{\pi} \left[ 1 + (\Psi_o - \Psi_i) \left( 1 + \frac{c_{le}}{c} \right) + (\Phi_o - \Phi_i) \left( 1 + \frac{c_{te}}{c} - K_\delta \frac{c_{te}}{c} \right) \right]} \quad 3.30$$

The parameter N is an empirical function of the Reynolds number taken from reference [41].  $C_{L\alpha=0}$  is the lift coefficient at zero angle of attack which is the sum of the coefficient of lift at zero angle of attack for the clean wing and the  $\Delta C_{L0}$  from flaps computed in Equation 3.15. The parameter a is the lift curve slope for the clean wing computed by the vortex lattice code. The parameters  $\Phi$  and  $\Psi$  are the same as computed for the change in maximum lift coefficient in section 3.7.  $K_\delta$  is a simple function of the flap deflection shown in Equation 3.31. It is an important note that  $\alpha_{CL=0}$  represents the angle of attack of the wing for which  $C_L=0$ , this value must be decreased by the angle of incidence to predict  $\alpha_{CL=0}$  for the aircraft, this is shown in Equation 3.32.

$$K_\delta = 1 - \cos(\delta_f) \quad 3.31$$

$$\alpha_{C_L=0}|_{body} = \alpha_{C_L=0} - W_{inc} \quad 3.32$$

The next parameter needed to estimate the lift curve slope for the high-lift configuration is to predict the angle of attack at which flow separations begin to dominate the lift curve slope. This is done through another iterative solution for  $\alpha^*$  shown in Equation 3.33, which is a function of similar parameters to the equation used to solve for the angle of attack at zero lift, Equation 3.30. The additional parameter  $C_L^*$  represents the lift coefficient at which large flow separations start and the overall lift curve exhibits nonlinear behavior. It is defined such that the point  $(\alpha^*, C_L^*)$  is on the lift curve. The value of  $C_L^*$  is 0.3 less than the maximum lift coefficient, Equation 3.34.

$$C_L^* = a \frac{180}{\pi} \left[ 1 + (\Psi_o - \Psi_i) \left( \frac{c_{le}}{c} \right) + (\Phi_o - \Phi_i) \left( \frac{c_{te}}{c} - K_\delta \frac{c_{te}}{c} \right) \right] (\alpha^* - \alpha_{C_L=0}) \cos^N(\alpha^* - \alpha_{C_L=0}) \quad 3.33$$

$$C_L^* = C_{L_{max}} - 0.3 \quad 3.34$$

The slope for the nonlinear portion of the curve can be computed using Equation 3.35.

$$\alpha^* = a \frac{180}{\pi} \left[ 1 + (\Psi_o - \Psi_i) \left( \frac{c_{le}}{c} \right) + (\Phi_o - \Phi_i) \left( \frac{c_{te}}{c} - K_\delta \frac{c_{te}}{c} \right) \right] \times \quad 3.35$$

$$\cos^N(\alpha^* - \alpha_{C_L=0}) \left[ 1 - N(\alpha^* - \alpha_{C_L=0}) \tan(\alpha^* - \alpha_{C_L=0}) \right]$$

The angle of attack for  $C_{L\max}$  is then a simple function of only the angle of attack at which nonlinearities dominate the lift curve and the nonlinear lift curve slope; this is presented in Equation 3.36.

$$\alpha_{C_{L\max}} = \alpha^* + \frac{0.39}{a^*} \quad 3.36$$

With all of the parameters computed it is now possible to compute the entire lift curve. The lift curve is separated into two parts, a generally linear portion for angles of attack less than  $\alpha^*$  and a nonlinear part for angles of attack greater than  $\alpha^*$ . Accordingly, the final lift versus angle of attack function is shown in Equation 3.37 for  $\alpha \leq \alpha^*$  and in Equation 3.38 for  $\alpha > \alpha^*$ .

$$C_L = a \frac{180}{\pi} \left[ 1 + (\Psi_o - \Psi_i) \left( \frac{c_{le}}{c} \right) + (\Phi_o - \Phi_i) \left( \frac{c_{te}}{c} - K_\delta \frac{c_{te}}{c} \right) \right] (\alpha - \alpha_{C_L=0}) \cos^N(\alpha - \alpha_{C_L=0}), \quad 3.37$$

$\alpha \leq \alpha^*$

$$C_L = C_{L\max} - 0.30 \left[ 1 - \frac{a^*(\alpha - \alpha^*)}{0.39} \right]^{1.3}, \quad \alpha > \alpha^* \quad 3.38$$

### 3.7.7. $C_L$ v Angle of Attack Results

The predictions of  $C_L$  v Angle of Attack are shown for the 737-700 in the landing and takeoff configurations in Figure 3.34. A similar comparison is made in Figure 3.35 for the wind tunnel model used in NASA TP-1580 [37]. A note about the wind tunnel model is that the error shown for the landing configuration is likely due to the landing gear deployment. The lift curve prediction does not account for large regions of separated flow underneath the wings. Nonetheless, the method shows very good correlation with both the flight and wind tunnel test results.

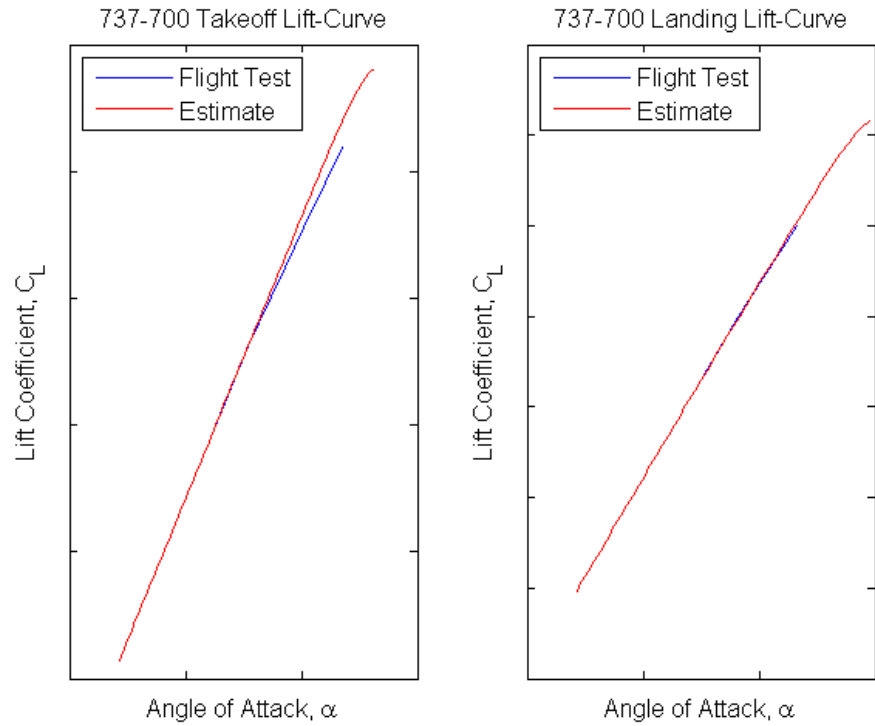


**Figure 3.34: Comparison of the predicted lift curve and flight test data for the 737-700 in both the takeoff and landing configuration.**

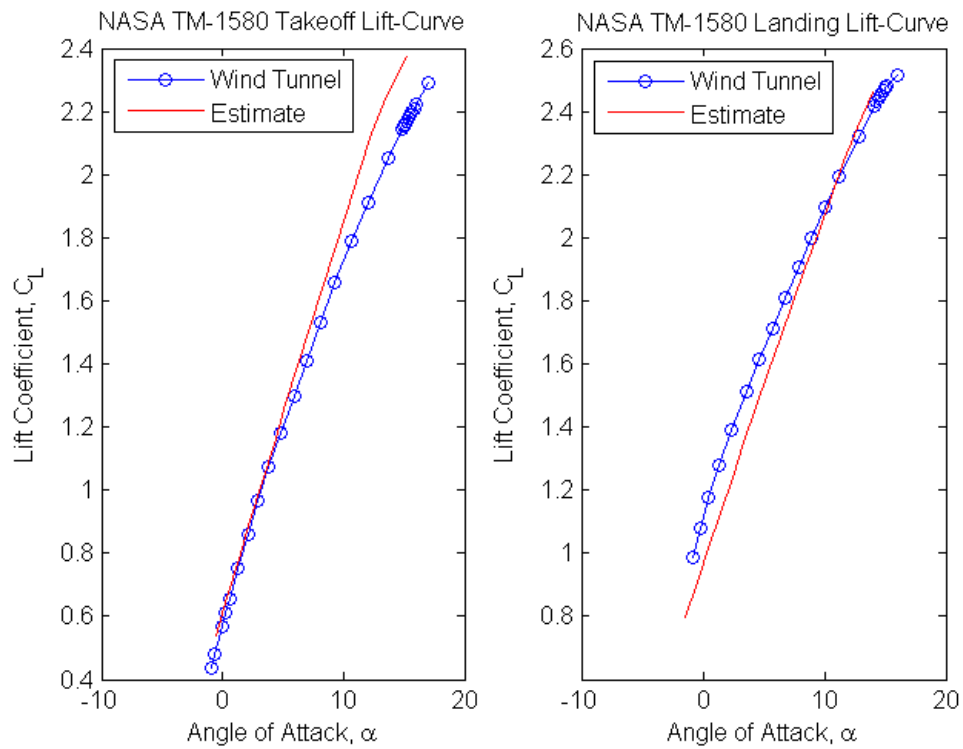


**Figure 3.35: Comparison of the predicted lift curve and wind tunnel data for the model of NASA TP-1580 in both the takeoff and landing configuration.**

### 3.8. Method Limitations/Known Issues

The low-speed aerodynamic prediction method discussed in this chapter is designed as a high-level conceptual design tool. For instance, with the 747-100 the nose shape input to the code is blunt; however it has the same total wetted area and fineness ratio as the actual 747-100. The correlations used for profile drag are unable to specifically capture the affects of the second level on the fuselage; however, a similar drag penalty can be otherwise modeled.

A known issue is the interference drag prediction due to engine-pylon-wing combination. The current method used is from Hoerner [26] and is only a function of the nacelle diameter and distance between the wing and the nacelle. This method is based on external stores and not engines; therefore, it is quite likely this term is in error or at least missing certain components. It is known that bypass ratio, vertical, and horizontal position of the nacelle with respect to the wing, are important; however, only the vertical position is considered in this correlation. There are a few mitigating factors in the prediction of interference drag, the most important being that interference drag is small when considered with the total aircraft drag, around 5%. Accordingly, even a 20% error in the interference drag prediction is only about a 1% error in the overall drag prediction. The other mitigating factor is that the trend of engine installations over time has been to locate the engines closer to the wing with a smaller separation distance. So, as technology improves the engines become closer to the wing and this method predicts a corresponding decrease in interference drag.

There is considerable confusion reducing multi-element flap deployment into one deflection angle. For instance, each flap surface on a triple-slotted flap could be deflected  $45^\circ$ ; however, the line from the hinge on the airfoil to the tip of the last flap could be approximately  $60^\circ$ . To confuse this further, Boeing reports flap deflection in detents which are the locations the flap lever in the cockpit. The detents do not directly correspond to other flap deflection angles. For instance an approximate mapping for the 777-200ER and 737-400 are shown in Table 3.5 and Table 3.6.

<b>Flap/Slat Detent</b>	<b>Minimum Flap Setting</b>	<b>Maximum Flap Setting</b>
1	$>0^{\circ}$	$\leq 1^{\circ}$
5	$>1^{\circ}$	$\leq 4.6^{\circ}$
10	$>4.6^{\circ}$	$\leq 9.6^{\circ}$
20	$>9.6^{\circ}$	$\leq 19.6^{\circ}$
25	$>19.6^{\circ}$	$\leq 24.6^{\circ}$
30	$>24.6^{\circ}$	$\leq 32.6^{\circ}$

**Table 3.5: 777-200ER Flap detents and bounds on corresponding flap deflection angles [42]**

<b>Flap/Slat Detent</b>	<b>Minimum Flap Setting</b>	<b>Maximum Flap Setting</b>
1	$>0^{\circ}$	$\leq 0.5^{\circ}$
5	$>0.5^{\circ}$	$\leq 5^{\circ}$
10	$>5^{\circ}$	$\leq 10^{\circ}$
15	$>10^{\circ}$	$\leq 15^{\circ}$
25	$>15^{\circ}$	$\leq 25^{\circ}$
30	$>25^{\circ}$	$\leq 30^{\circ}$
40	$>30^{\circ}$	$\leq 40^{\circ}$
45	$>40^{\circ}$	

**Table 3.6: 737-400 Flap detents and bounds on flap deflection angles [43].**

Accordingly, there are some inaccuracies in that the polars cannot be matched exactly to a flap deflection or slat deflection angle. The mitigating factor is, the method still appears to estimate the correct drag polar for each flap and slat deflection when a flap deflection angle within a couple of degrees above or a couple of degrees below is used. For instance, the predicted drag polar for an aircraft with flaps detent 15 maybe high; however, if the flap deflection angle were to be reduced to  $12^{\circ}$  the polar and lift curve will likely be correct.



## CHAPTER 4: Trajectory Modeling

Airport community noise is dependent on the flight path the airplane travels. Noise dissipates when traveling through the atmosphere so increasing the height of the aircraft above the ground reduces the noise experienced on the ground. However, increases in thrust also increase the amount of noise the aircraft produces, so there is a trade-off. This chapter presents the modeling approach for trajectory simulation. The trajectories are computed so they are as realistic as possible and so they represent the actual trajectories that an airplane flies. They account for small effects including finite thrust rise or fall-off times, and finite time changes for varying flap settings. The simulation is separated into two parts, the takeoff roll, which is defined as start of the roll until the airplane has reached the takeoff reference speed,  $V_2$ , at an altitude of thirty-five feet, [44], and the climb segment, which uses the airplane state at thirty-five feet as its initial condition and simulates the climb to a specified altitude.

### 4.1. Methodology--Takeoff

The takeoff calculation is designed to be as accurate as can be achieved with the low-speed aerodynamics model. It consists of a 4<sup>th</sup> order accurate Runge-Kutta integration scheme with adaptive time stepping and includes ground effect, decreasing rolling friction with increasing lift, thrust lapse effects, and a simple rotation model. A free-body diagram of the forces acting on an aircraft when on the ground is shown in Figure 4.1. The equations of motion are obtained by summing all of the forces acting on the airplane. The acceleration in the horizontal direction is shown in Equation 4.1 and is equal to the thrust,  $T$ , minus the drag,  $D$ , and the rolling friction,  $F_r$ , divided by the aircraft mass. The vertical acceleration is shown in Equation 4.2, and is the sum of the thrust minus the drag multiplied by the sine of the flight path angle relative to the horizontal,  $\gamma$ , plus the lift,  $L$ , multiplied by the cosine of the flight angle minus the aircraft weight,  $W$ , all divided by the aircraft mass. The ground plane is modeled in that if the vertical acceleration is negative, a force representing the ground,  $F_g$ , is added such that the vertical acceleration is zero. Another concern while the aircraft is on the ground is the aft portion of the fuselage may not strike the ground. Accordingly, there is an upper bound on the flight path angle. In addition, while the airplane is on the ground, there is strict relationship

between the wing's angle of attack,  $\alpha$ , the wing angle of incidence,  $W_{inc}$ , and the flight path angle; it is shown in Equation 4.3. These equations, and the aircraft rotation model, are integrated in time until the airplane reaches an altitude of thirty-five feet.

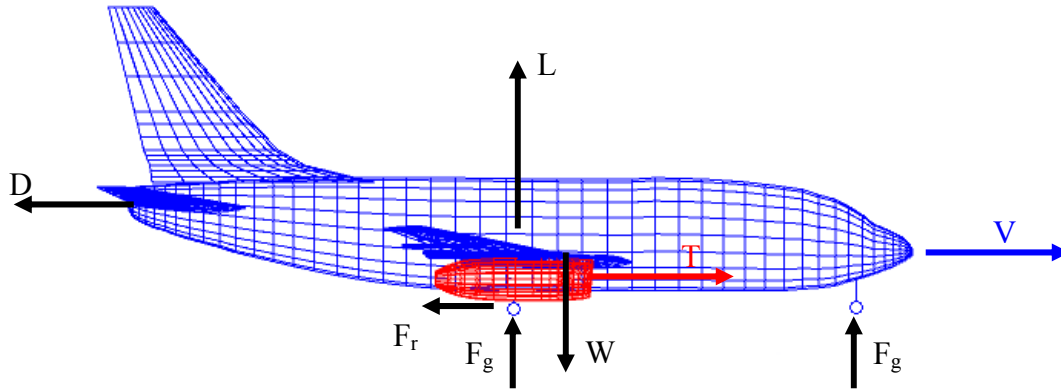


**Figure 4.1: Forces used for takeoff simulation.**

$$a_x = \frac{T - D - F_r}{W/g} \quad 4.1$$

$$a_y = \min\left[0, \frac{(T - D)\sin \gamma + L \cos \gamma - W}{W/g}\right] \quad 4.2$$

$$\gamma = \alpha - W_{inc} \quad 4.3$$

The rolling friction model used is quite simple and comes from Schaufele [10]. The rolling friction is the normal force exerted by the ground on the airplane multiplied by a constant,  $\mu$ . The formulation is in Equation 4.4.

$$F_r = \mu(W - L \cos \gamma); \mu = 0.15 \quad 4.4$$

Both the lift and drag are interpolated by angle of attack from the low-speed aerodynamics results. One modification employed is the use of a ground effect model from Hoerner [26]. With this model, the induced drag is scaled by a function of the proximity of the wing to the ground plane nondimensionalized by the wing span. The function from Hoerner is shown in Figure 4.2.

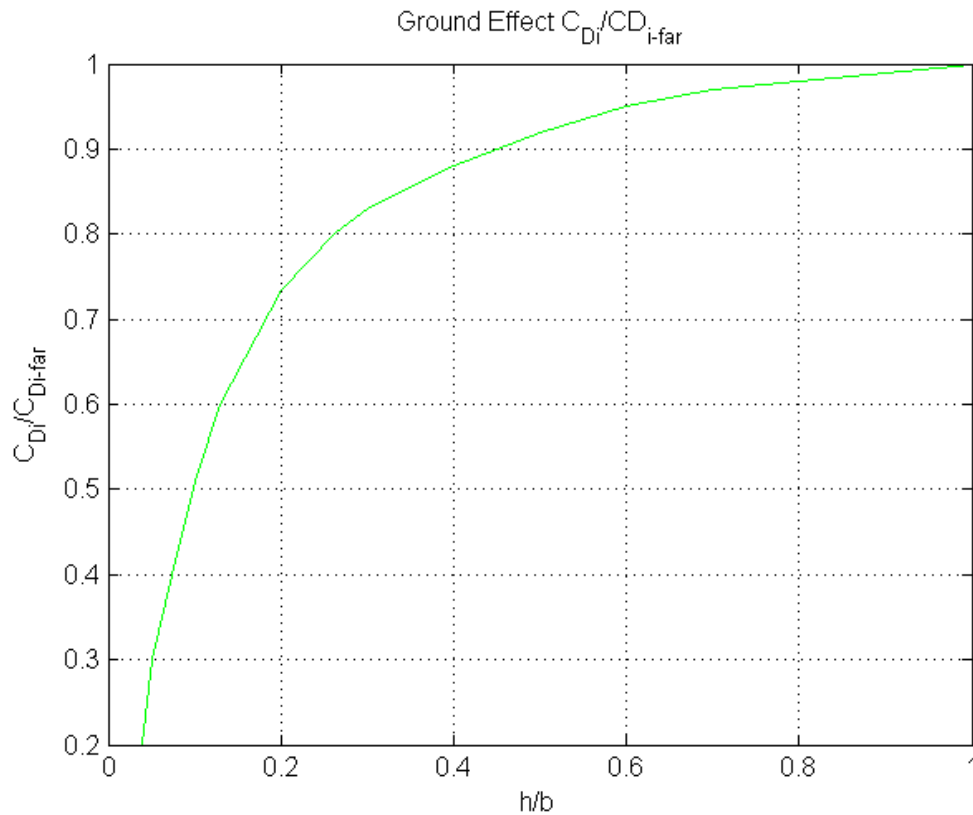


**Figure 4.2: Ground effect, ratio of induced drag in ground effect to far-field induced drag. The abscissa,  $h/b$ , is the height of the wing above the ground plane divided by the wing span [26].**

To isolate the induced drag portion of the drag polar, a quadratic polynomial is fit to the drag polar and the total drag minus the constant drag from the polynomial fit is considered to be the induced drag. This method assumes that the aircraft drag behaves in a textbook sense and that drag is the sum of a constant term and a term that is a function of the square of the lift coefficient. That prediction of the induced drag is then scaled by the appropriate ratio interpolated from the Hoerner plot and added to the constant drag term. This value of drag is then used in the integration procedure.

#### 4.1.1. Engine Thrust Prediction

Two methods are used to estimate the change in engine thrust as velocity, altitude, and temperature change. The first is regression of data from engine manufacturers contained in the

Integrated Noise Model (INM) [45], and the second is full engine performance tables from Pratt & Whitney [46]. The form of the INM regression data is shown in Equation 4.5, the definition of the parameters is shown in Table 4.1, and the values for the GE90-90B engine are shown in Table 4.2.

$$\frac{T_n}{\delta} = E + FV + G_A h + G_B h^2 + H_C T_C \quad 4.5$$

$\frac{T_n}{\delta}$	Corrected net thrust per engine, engine net thrust divided by the ambient pressure ratio.
E	Regression coefficient (lbf)
F	Regression coefficient (lbf/knot)
V	Aircraft velocity (knots)
$G_A, G_B$	Regression coefficients (lbf/ft, lbf/ft <sup>2</sup> )
h	Altitude (ft)
$H_C$	Regression coefficient (lbf/°C)
$T_C$	Temperature at the aircraft (°C)

**Table 4.1: Definition of parameters in INM thrust lapse model [45].**

	<b>Maximum Takeoff</b>	<b>Maximum Climb</b>
E (lbf)	93672.6	67093.7
F (lb/kt)	-122.25	-85.76
$G_A$ (lb/ft)	1.182	1.850
$G_B$ (lb/ft <sup>2</sup> )	-8.06e-5	-7.6e-5
$H_C$ (lbf/°C)	0	0

**Table 4.2: Sample regression coefficients for use in INM thrust lapse model for GE90-90B engine.**

The other method for predicting thrust lapse, the use of full engine performance tables should be more accurate, and will also enable the fuel burn to be computed. The challenge is that almost all data of this form is proprietary; however, at the time of the writing of this document the author was in possession of data for the JT8D-9 and JT9D-7A engines [46]. The engine performance charts are in the form of carpet plots of thrust and specific fuel consumption as functions of power setting and Mach number. In addition, there is a unique carpet plot for each altitude the engine was tested at. Accordingly, the interpolation of data on these charts is rather complicated, so a summary of the interpolation is included herein.

The interpolation was formulated such that either a value of net thrust or a throttle setting, fraction of maximum thrust, could be used. If the throttle setting were used, the maximum climb thrust was interpolated from engine performance data at 85% power and was scaled to the desired throttle setting to obtain a net thrust. The net thrust and aircraft flight Mach number were used to obtain the four nearest data points on the engine performance carpet plot, where a maximum of two data points from any constant power or constant thrust line were used. Given these four data points an isoparametric quadrilateral is created. This enables 3-5 iterations of a Newton solution to find a quadratic interpolation of the desired performance point from the nearest four data points. Given a few bounds on the shape of the elements, the solution sequence shows great aptitude for interpolation and extrapolation.

The remaining step to find the thrust is to interpolate the altitude effects. The charts for the altitude immediately higher and immediately lower than the desired altitude are used. The corrected net thrust is assumed to vary linearly in altitude,  $h$ , and is used for the interpolation, in lieu of the net thrust such that thrust lapse is better captured. This interpolation is shown in Equation 4.6. For specific fuel consumption the variation with altitude is computed with a direct linear interpolation and the values are not corrected.

$$\frac{F_n}{\delta} = \left[ \frac{F_n}{\delta} \Big|_2 - \frac{F_n}{\delta} \Big|_1 \right] / [h_2 - h_1] (h - h_1) + \frac{F_n}{\delta} \Big|_1 \quad 4.6$$

#### 4.1.2. Takeoff Rotation

To properly compute the rotation rate of the aircraft would involve computing the aircraft's moment of inertia and attempting to compute the moments about the aircraft's landing gear. There is an insufficient amount of public data to accurately predict the weight distribution of commercial aircraft, so the rotation is modeled in a lower-fidelity way. The first approximation is from the 777-200 Operator's Manual [47], which contains a list of rotation speeds,  $V_r$ . It appears that a good fit for the rotation speed is seven knots less than  $V_2$ , the minimum controllable airspeed; this is shown in Equation 4.7.

$$V_r \approx V_2 - 7kts \quad 4.7$$

After the rotation speed is reached the aircraft will rotate at peak rate of three degrees per second until the reference speed  $V_2$  is attained. This speed must occur at or before the aircraft reaches a height of thirty-five feet above the ground. The peak rotation rate is from National Transportation Safety Board accident reports where aircraft struck their tail during takeoff because the pilots exceeded the aircraft's design maximum rotation rate of three degrees per second [48]. Accordingly, the rotation rate is given by Equation 4.8.

$$\frac{d\alpha}{dt} = \max[3, 0.8(\alpha_{V_2} - \alpha)] \quad 4.8$$

The behavior of the aircraft rotation is such that the aircraft rotation angle exponentially decays to the angle of attack at which the aircraft attains the desired flight speed. The constant, 0.8, represents a value representative of most commercial aircraft and one that will not cause the aircraft to rotate so quickly that the drag increases fast enough to slow the airplane and prevent it from leaving the ground. This model is unphysical, but compares well with the actual takeoff behavior of commercial aircraft.

#### *4.1.3. Takeoff Method Validation*

There is a small set of data available to validate the takeoff prediction method, which is the Federal Aviation Regulations (FAR25) for takeoff field length [44]. The aircraft manufacturers are required to publish the legal runway length from which their aircraft are allowed to takeoff, and by computing these legal distances a validation of the takeoff method is possible. The regulations are divided into two sections, all engines operating and one-engine failed.

For the case of all engines operating, the FAR25 takeoff field length is defined as 115% of the horizontal distance required for the airplane to attain an obstacle clearance height of thirty-five feet.

For the case where an engine has failed the analysis is considerably more complicated. At the instant the engine fails, there is a two-second period at which no control inputs can be made as this is to simulate the pilot reaction time. At that point, the pilot may either reject the takeoff by applying full brakes and spoilers, but not any reverse thrust, or the pilot may continue the takeoff on the remaining engines. If the pilot continues the acceleration to takeoff the normal takeoff analysis is run, but with the thrust from one less engine. If the pilot rejects the takeoff, after the two-second delay, the thrust is set to zero, full-braking is assumed and the drag from spoilers is simulated.

To simulate full-braking, the maximum of braking coefficients is used. There are two publicly available sources for maximum braking coefficients of current aircraft. FAR25 has two sets of braking coefficients for wet runways, one for aircraft with active break controls and one for aircraft without active break controls [44]. The other source is a regression of 737 dry-runway braking coefficient tests [49]. Since this model is only used for dry runways it was assumed the maximum braking coefficients would be the maximum of the wet runway braking coefficient and the 737 dry-runway braking coefficients. The FAR25 braking coefficients are a function of both speed and aircraft tire pressure, and the dry-runway 737 runway braking coefficients are a function of only aircraft velocity. Accordingly, the variation in normal force due to decreased lift and the variation in braking force due to speed are both modeled.

The aircraft spoiler drag is modeled in a much simpler fashion. In Shaufele, there is a spoiler drag coefficient given in an FAR25 sample problem for the DC-9 [10]. This drag coefficient is used for all aircraft for lack of any data about aircraft spoiler drag.

With the engine-failed case, the FAR25 distance is defined as the distance when both the distance to continue to accelerate and takeoff is equal to the distance to bring the airplane to a complete stop on the runway. This is known as the concept of a balanced field, and the speed at which the distances are equal is called  $V_{EF}$ . There is another reference speed  $V_1$  which must be greater than  $V_{EF}$ , and some mechanisms are used by the airframe and engine manufacturers such that  $V_1$  may be used to artificially lower the balanced field length. This may be done by having an automatic override of a thrust de-rate or another change to the takeoff procedure.

Essentially,  $V_1$  is the critical speed that when the aircraft reaches it the pilots must continue to takeoff and the aircraft will no longer be allowed to stop, or be capable of stopping, on the runway [50].

Overall, the FAR25 required runway length is the maximum of the 115% of the all engine operating runway length and the balanced field length.

#### 4.1.4. Takeoff Method Results

The results of the FAR25 runway length requirements are used to validate that the takeoff simulation is accurate. Matching the FAR25 distances requires a high level of accuracy of not only the takeoff procedure, but also methods to have the aircraft takeoff with one-engine failed and prediction of minimum stopping distances. Accordingly, the fact that the FAR25 predictions of the takeoff simulation and the published values are within five-percent show that the takeoff simulation exceeds the level of accuracy needed to simulate departure for noise concerns. The FAR25 takeoff field lengths have been studied for two airplanes, the Boeing 777-200 shown in Figure 4.3, and the Boeing 747-200 shown in Figure 4.4.

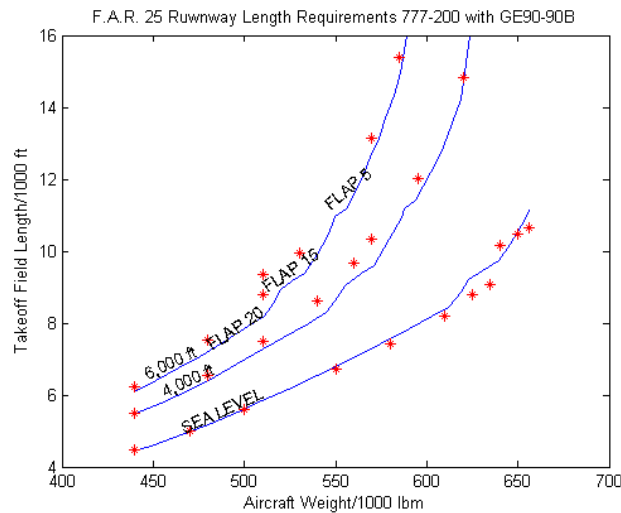


**Figure 4.3: Comparison of estimated FAR25 runway length requirement for the Boeing 777-200 with the GE90-90B engine and values published by Boeing. The red asterisks are the estimates and the blue lines are the published data [51].**

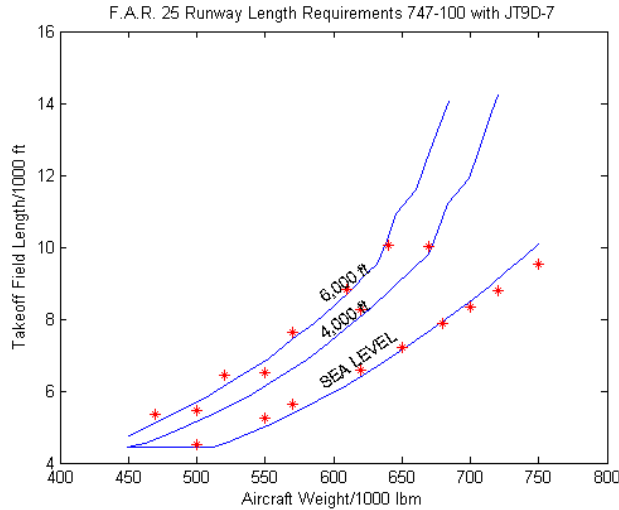


**Figure 4.4: Comparison of estimated FAR25 runway length requirement for the Boeing 747-100 with the GE90-90B engine and values published by Boeing. The red asterisks are the estimates and the blue lines are the published data [52].**

It is worth noting that except where the flaps settings change in the published data, the predictions of distance are within five-percent. In the areas where the flap settings are being varied the correlation is considerably worse. However, it is likely that Boeing “connected the dots” and that the line segments plotted are not real data [25].

## 4.2. Methodology--Flight

The in-flight trajectory method is designed to follow the method in SAE-AIR-1845 [53], as this is the method contained in the INM. However, there are some substantial modifications to the method in an attempt to make the trajectory simulation more accurate. It should be noted that two trajectory simulations are in use, a full model and a reduced linear model. The reduced linear model is considerably similar in scope and accuracy to the method contained in SAE-AIR-1845, but in large part that method is considered secondary to the full model. In this light, the linear model will only be discussed briefly and comparisons between the linear model and the method in SAE-AIR-1845 are left to the reader.

The simulation is based on a free-body diagram of an aircraft in flight. By definition the lift vector is perpendicular to the aircraft velocity and the drag is anti-parallel to the velocity. The thrust is assumed to be aligned with the aircraft axis, although on most commercial aircraft the

thrust vector is about 1.5 degrees from the aircraft axis. The error caused by this is insignificant as the cosine of 1.5 degrees causes a thrust loss of less than four-hundredths of a percent. The free-body diagram is shown in Figure 4.5.

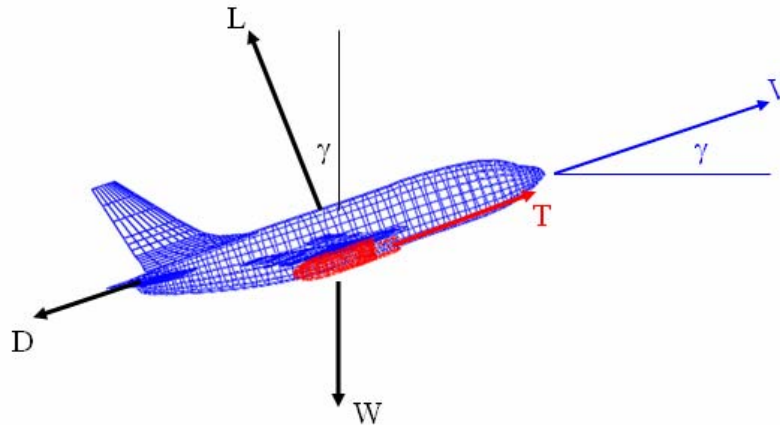


**Figure 4.5: Free-body diagram of an aircraft in flight.**

From the free-body diagram, a summation of forces in the horizontal direction,  $x$ , and vertical direction,  $y$ , enable the aircraft's acceleration to be computed. The equations for the horizontal and vertical accelerations are shown in Equations 4.9 and 4.10 respectively.

$$a_x = \frac{(T - D)\cos \gamma - L\sin \gamma}{W/g} \quad 4.9$$

$$a_y = \frac{(T - D)\sin \gamma + L\cos \gamma - W}{W/g} \quad 4.10$$

An important note is that the lift and drag are dependent on each other, and that the angle of attack sets the ratio of lift to drag. That constraint means three methods of climbing are available to the pilots of an airplane. The first climb type, (1) is for a constant flight path angle,  $\gamma$ , and a constant velocity,  $V$ . With both the flight path angle and velocity specified, the required thrust can be computed by solving the Equations 4.9 and 4.10 such that both horizontal and vertical accelerations are zero. The second climb type (2) is for a constant thrust and velocity. This is typical of an initial climb out of an airport where an aircraft climbs at the velocity  $V_{2+15\text{kts}}$  with a constant throttle setting. In this case, the angle of attack must be computed such that the accelerations in Equations 4.9 and 4.10 are both zero. The final climb

type (3) is an acceleration climb. In an acceleration climb, the thrust and rate of climb are fixed and the aircraft can vary both the angle of attack and flight path angle such that the desired velocity change is achieved. The three climb types represent the capabilities of the flight instruments available to the pilots; they require only knowledge of airspeed, rate of climb and throttle lever setting, three of the six primary flight instruments.

For the first type of climb, a constant flight path angle and velocity, Equations 4.9 and 4.10 are converted to the form shown in Equations 4.11 and 4.12. Equation 4.11 is solved for the lift coefficient the aircraft should be flying at, that lift coefficient is then used to compute the drag coefficient from the drag polar. With both the lift and drag coefficient Equation 4.12 is used to compute the required thrust.

$$C_L = \frac{W/\cos \gamma}{\frac{1}{2}\rho V^2 S} \quad 4.11$$

$$T = \frac{1}{2}\rho V^2 S C_D + W \sin \gamma \quad 4.12$$

Similarly for the second type of climb, constant thrust and constant velocity, Equations 4.11 and 4.12 are used to solve for the flight path angle as a function of the angle of attack. The angle of attack is used with the lift curve slope to predict the lift coefficient, which is then interpolated in the drag polar to find the drag coefficient. A zero crossing method is used with the angle of attack as the dependent variable to find when the flight path angle computed with Equation 4.11 is equal to the flight path angle computed with Equation 4.12. For the acceleration climb case, the constant rate of climb is used to compute an instantaneous flight path angle. Equations 4.11 and 4.12 are then solved with a bisection search to find the instantaneous angle of attack that will solve that system of equations.

The fact that the constant rate of climb acceleration case is inherently unsteady (both velocity and flight path angle are constantly changing) makes the discussion of how time variations are solved in the model important. There are numerous other ways to have transients in the climb methods, for instance, with both the constant velocity climb methods, what happens if the initial aircraft state is at another velocity or a different angle of attack?

The essential equation of the transients between flight segments and the acceleration case is Equation 4.13. The basis of the equation is that the pilot can control the airspeed by adjusting either the throttle or the angle of attack. For a fixed throttle setting, the only input is the angle of attack. Accordingly, Equation 4.13 will vary the angle of attack so that it exponentially decays or increases at rate that will force the aircraft airspeed and flight path angle to converge to the desired values. Again a rate limit is applied to the pitch rate so that three degrees per second is not exceeded.

$$\frac{d\alpha}{dt} = 2.5(\alpha_{desired} - \alpha(t) + \gamma_{desired} - \gamma(t)) \quad 4.13$$

Other transients accounted for in the simulation are changing aircraft flap settings and aircraft power settings. On real aircraft the flap settings do not change instantaneously, so in this simulation when a flap setting is changed the drag polar is interpolated between the drag polars of each setting. It is assumed that it takes approximately five seconds for the flap settings to change. Similarly, when a throttle setting is varied the thrust varies like the exponentially decaying function similar to that in Kerrebrock [54]. This is because jet engines require time for the shafts to spool-up or spool-down when the throttle setting is varied. The time constant for the exponential decaying function is such that ninety-nine percent of the variation occurs in one and a half seconds.

The entire system of equations is then integrated with a 4<sup>th</sup> order accurate variable time-step Runge-Kutta method. The integration scheme is capable of switching between the three types of climb during a climbout procedure, for velocity changes larger than five percent it is recommended to use an acceleration procedure, otherwise, the transient portion of the code should be able to establish the aircraft on the desired velocity and flight path angle.

### 4.3. Validation, INM results

A collection of cases was used to verify the methods. The two cases presented herein are comparisons with manufacturer procedures defined as standard departures contained in the

INM. The first procedure is for the Boeing 777-200 with GE90-90B engines taking off at maximum gross weight, 656,000 lbm. The second procedure is the Boeing 747-200 with JT9D-7A engines with a gross weight of 725,000 lbm. The two climbing procedures are detailed in Table 4.3.

777-200 Standard Departure	747-200 Standard Departure
<ul style="list-style-type: none"> <li>• Takeoff, Flaps 5, 100% (Takeoff) Thrust <ul style="list-style-type: none"> <li>– Constant acceleration takeoff</li> <li>– Constant V climb to 1000’ AGL</li> </ul> </li> <li>• Flaps to 1, 85% (Climb) Thrust <ul style="list-style-type: none"> <li>– Accelerate to 221.7kts while climbing 875fpm</li> </ul> </li> <li>• Flaps up, 85% (Climb) Thrust <ul style="list-style-type: none"> <li>– Accelerate to 235.4kts while climbing 970fpm</li> <li>– Accelerate to 246kts while climbing 1020fpm</li> <li>– Constant V climb to 3000’ AGL</li> <li>– Accelerate to 250kts while climbing 1031fpm</li> <li>– Constant V climb to 5500’ AGL</li> <li>– Constant V climb to 7500’ AGL</li> <li>– Constant V climb to 10,000’ AGL</li> </ul> </li> </ul>	<ul style="list-style-type: none"> <li>• Takeoff, Flaps 10, 100% (Takeoff) Thrust <ul style="list-style-type: none"> <li>– Constant acceleration takeoff</li> <li>– Constant V climb to 1000’ AGL</li> <li>– Accelerate to 216.0kts while climbing 1012fpm</li> </ul> </li> <li>• Flaps 5, 85% (Climb) Thrust <ul style="list-style-type: none"> <li>– Accelerate to 256.0kts while climbing 500fpm</li> </ul> </li> <li>• Flaps 0, 85% (Climb) Thrust <ul style="list-style-type: none"> <li>– Accelerate to 276kts while climbing 500fpm</li> <li>– Constant V climb to 5,500’ AGL</li> <li>– Constant V climb to 7,500’ AGL</li> <li>– Constant V climb to 10,000’ AGL</li> </ul> </li> </ul>

**Table 4.3: Detailed climb procedures for Boeing 777-200 and Boeing 747-200 aircraft at maximum takeoff weight contained in the INM.**

The two departures are simulated with the full model as discussed previously and with a linear model as a time saving method. The linear model assumes that all quantities change linearly with time and that many quantities can be replaced with their averages over long time periods. For instance, the thrust during a climb segment is treated as constant, with the value taken at the mid-altitude of the climb segment. Similarly, for acceleration cases many quantities are treated as constant and are measured at the mid-velocity. The results of the two models and the flight path data contained in the INM are shown in Figure 4.6 for the 777 and in Figure 4.7 for the 747. The estimates of final horizontal distance required for the aircraft to reach 10,000 feet above ground level from each method is then compared in Table 4.4 for the 777 and in Table 4.5 for the 747.

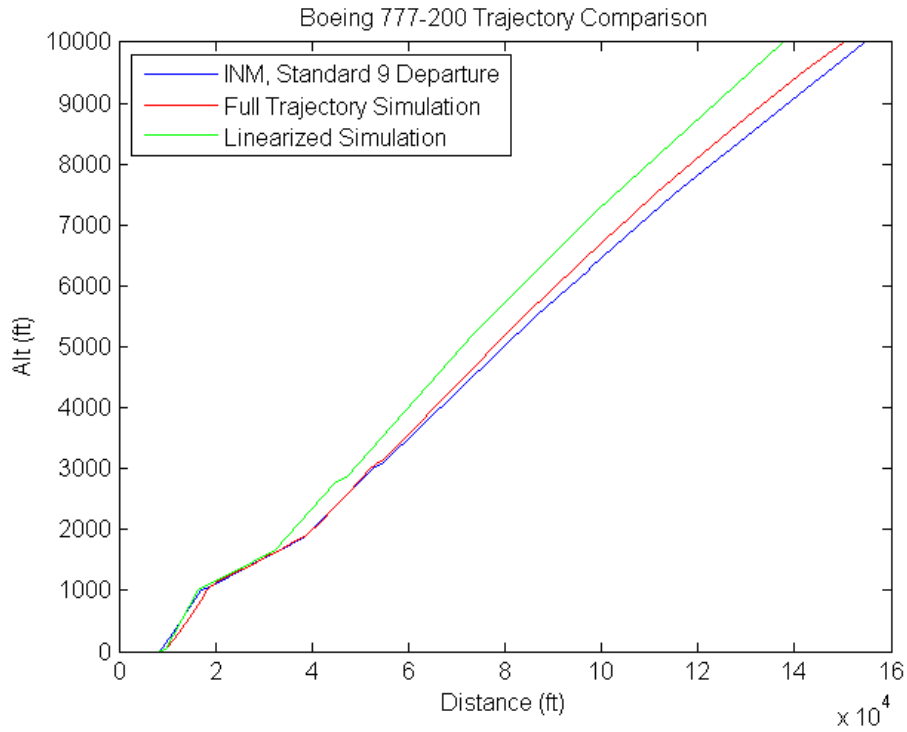


**Figure 4.6: Comparison of the trajectory computed with the full simulation and the linear model compared to the data contained in the INM for the Boeing 777-200.**

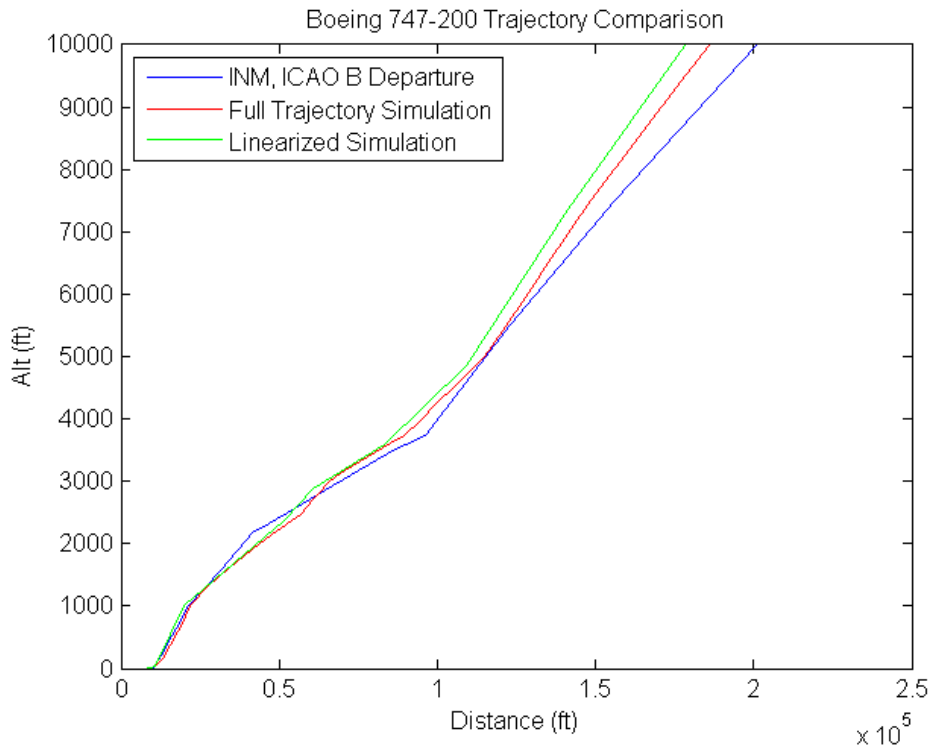


**Figure 4.7: Comparison of the full and linear simulation method and the trajectory data for the Boeing 747-200 contained in the INM.**

<b>Boeing 777-200</b>	<b>Horizontal Distance at 10,000 ft</b>	<b>% Difference</b>
INM, Standard 9 Departure	25.4nm	0
Full Trajectory Simulation	24.7nm	2.66%
Linearized Simulation	22.7nm	10.5%

**Table 4.4: Comparison of total horizontal distance covered when the aircraft reaches 10,000' for the Boeing 777-200. The percent difference between the linear model and the full simulation is 8.07%.**

<b>Boeing 747-200</b>	<b>Horizontal Distance at 10,000 ft</b>	<b>% Difference</b>
INM, Standard 6 Departure	33.1nm	0
Full Trajectory Simulation	30.6nm	7.46%
Linearized Simulation	29.5nm	11.0%

**Table 4.5: Comparison of total horizontal distance covered when the aircraft reaches 10,000' for the Boeing 747-200. The percent difference between the linear model and the full simulation is 3.76%.**

The results show that the flight path simulation generates results that are quite similar to the trajectories contained in the integrated noise model. The trajectories in the INM are computed using a simple linear procedure from manufacturer data, so the differences between the full simulation and the INM trajectories may not be error. It is possible that the full simulation which attempts to account for considerably more effects than INM may be more accurate; however, both methods show very similar results so that the simulation should be considered validated and able to produce trajectories to within 10% of INM trajectories.



## CHAPTER 5: Noise Estimation

There are two main components to estimating the community noise from an aircraft. The first component is determining how much noise the aircraft generates and the second is determining the quantity and location of the noise that reaches the ground. This work is primarily focused on low-speed aerodynamics so the noise signature of the engine will be assumed constant, that is, the engine will not vary; however, the thrust levels will, and the only changes in noise emanating from the engine considered will be due to changes in aircraft thrust. Accordingly, the low-speed aerodynamics can impact noise in three ways. First, (1) there can be aircraft configuration changes such as increasing flap and slat deployment which change the airframe noise signature. Second, (2) if a set flight path angle is prescribed, better aerodynamic performance will require less thrust and the low-speed performance will reduce the amount of engine noise required to perform the maneuver. Third, (3) for a fixed thrust level better aerodynamic performance will give the airplane better climb performance and it will climb at a steeper angle which increases the distance between the airplane and the ground and will reduce the amount of community noise because of atmospheric dissipation. This chapter will discuss the method for estimating the quantity and location of noise that reaches the ground.

### 5.1. Aircraft Noise Estimation

The Integrated Noise Model, INM, contains data called noise-power-distance curves, NPDs, which are either supplied by aircraft manufacturers or are experimentally determined. An NPD contains the aircraft noise caused by an aircraft passage at a set of heights directly overhead and with its engines at different thrust levels. For instance, a Boeing 777-200 will have about five NPDs for both approach and departure aircraft configurations corresponding to different levels of thrust. Each NPD will plot noise in decibels as a function of the logarithm of distance from the aircraft. A sample NPD, for the Boeing 777-200 with GE90-90B engines contained in INM is shown in Figure 5.1.

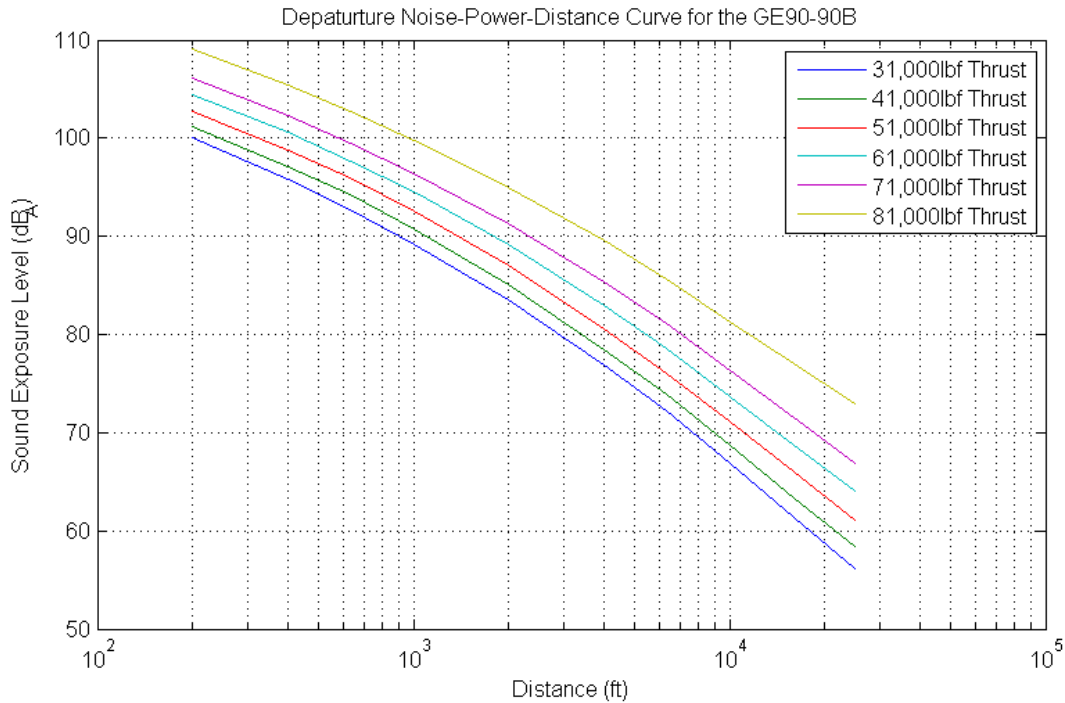


**Figure 5.1: Departure Noise-Power-Distance curve for the Boeing 777-200 with GE90-90B engines. Thrust level is corrected the net thrust per engine, so the total thrust will actually be twice the number shown as the 777 has two engines.**

The set of NPDs shown in Figure 5.1 is the entire aircraft noise signature. The only caveat to that statement is if another frequency weighting is desired, for instance Effective Perceived Noise Level (EPNL) as opposed to the A-weighted Sound Exposure Level (SEL). Each frequency weighting will have its own set of NPDs so there will be a unique set of NPDs for any frequency weight, in this case both SEL and EPNL will have a set of NPDs. However, assuming noise impacts are only being evaluated in one frequency weighting, the set of NPDs similar to Figure 5.1 is the complete aircraft noise signature. Accordingly, to find the variations in aircraft noise signature that correspond to changes in aircraft configuration such as flap and slat deployment it is necessary to compute the changes in the NPDs.

To compute the change in the NPDs the airframe-only noise signature is estimated and subtracted from the NPDs. The new airframe noise signature for the modified configuration is then estimated and added back to the NPDs. This should, assuming the airframe noise predictions are accurate, correctly scale the NPDs to account for a modified aircraft configuration with a constant engine.

There are to date only two computational methods for determining airframe noise signatures, a set of empirical methods and computational aero-acoustics. Using computational aero-acoustics for noise requires large amounts of computer processing power and is largely only feasible at the component level, although fairly good accuracy is possible [55]. For complete airframes empirical methods seem to be the current industry standard, and there are three methods in particular. There is an FAA method by Fink [56], and a NASA method called the Aircraft Noise Prediction Program (ANOPP) [57]. Another reference by Hubbard [58] compares the two methods. A third empirical method by the Engineering Science Data Unit [59], ESDU, is also quite similar to, and references, the ANOPP method. It claims to be a slightly improved version of the ANOPP method, but only has one or two coefficients that are slightly different. The ANOPP method was selected to maintain consistency between codes used within EDS.

The ANOPP method separates the airframe into major components, such as the wing and tail surfaces. The noise signature of each component is comprised of five empirical functions. One function is the noise directivity which is a function of the two angles from the aircraft to the observer. Varying the angles in this function enables the entire noise signature of the airframe to be integrated over a flight path. For the NPDs used in the INM, the flight paths that must be simulated are infinitely long, straight, constant velocity, directly overhead passage of the aircraft flying at 160 knots [45]. The ANOPP method must also be supplemented with an atmospheric dissipation model so the NPDs estimated can be used to predict the noise at an airport. There are two different sets of atmospheric dissipation coefficients, SAE-AIR-1845 [53] and FAR A36.4 [60]. The atmospheric dissipation is in units of decibels per one-hundred feet and is given as a function of frequency. The two methods are compared in Figure 5.2. The atmospheric absorption in SAE-AIR-1845 is less conservative, i.e. there is more noise dissipation, than FAR A36. The dissipation however, is quite similar at low frequencies, and it is only at high frequencies that they differ. The dissipation from SAE is primarily used for airport community noise predictions; whereas, the dissipation in FAR A36 is used for aircraft noise certification. Since the primary objective of this work is airport community noise only

the dissipation coefficients contained in SAE-AIR-1845 will be used. This will still be true even in the test cases where certification noise is estimated for purposes of validation.

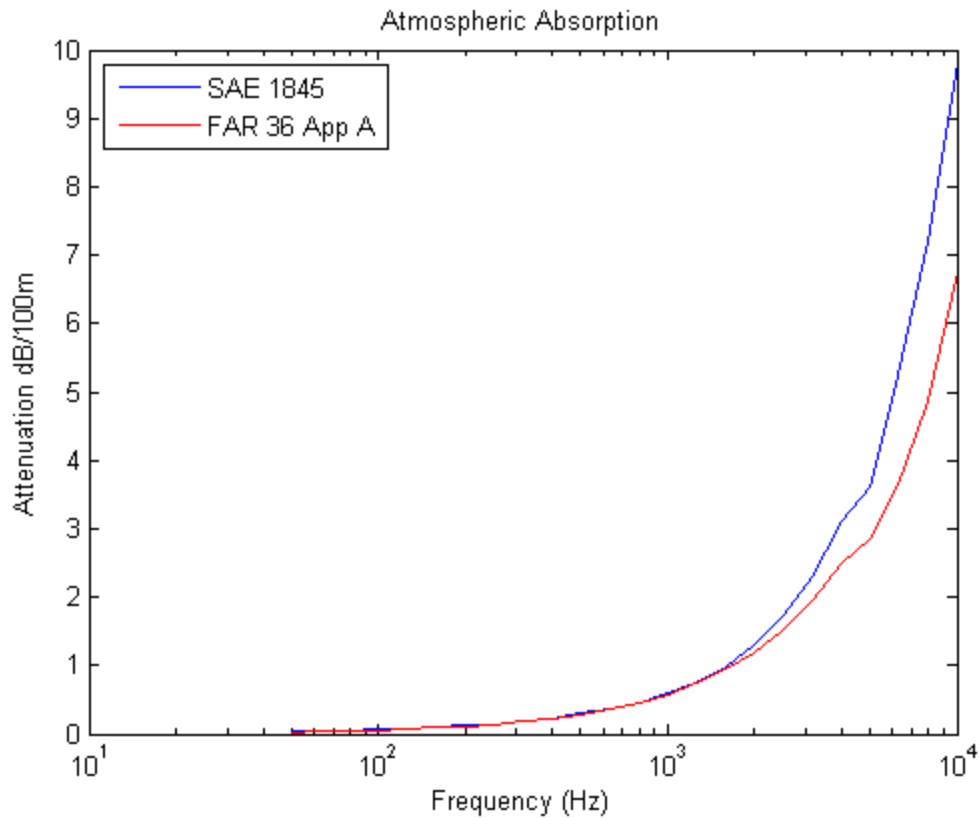


**Figure 5.2: Comparison of the atmospheric absorption of noise from SAE-AIR-1845 and FAR A36 [53], [60].**

The ANOPP method and SAE-AIR-1845 atmospheric dissipation have been used to predict the NPDs for the Boeing 777-200 airframe noise and compared with the NPDs contained in the INM. The NPDs in the INM include the noise generated by the engine; however, the NPDs from ANOPP do not. Accordingly, the NPDs predicted for the airframe should always be less than the NPDs contained in the INM; this difference should be considerable for takeoff NPDs and slight for landing NPDs. The comparison between the takeoff NPDs in INM with 31,000 lbf of thrust per engine (62,000 lbf of total thrust) is compared with the airframe only contribution in Figure 5.3. The aircraft configuration used for takeoff is slats takeoff, which is deployed but still sealed, and flaps deployed five-degrees. The landing configuration NPDs are shown in Figure 5.4, in this case the aircraft thrust contained in the INM NPDs is only 12,000 lbf per engine, so the predictions from ANOPP should only be slightly less than the data

contained in the INM. The aircraft configuration for the landing NPDs is slats landing, deployed and gapped, flaps thirty-degrees, and landing gear deployed.

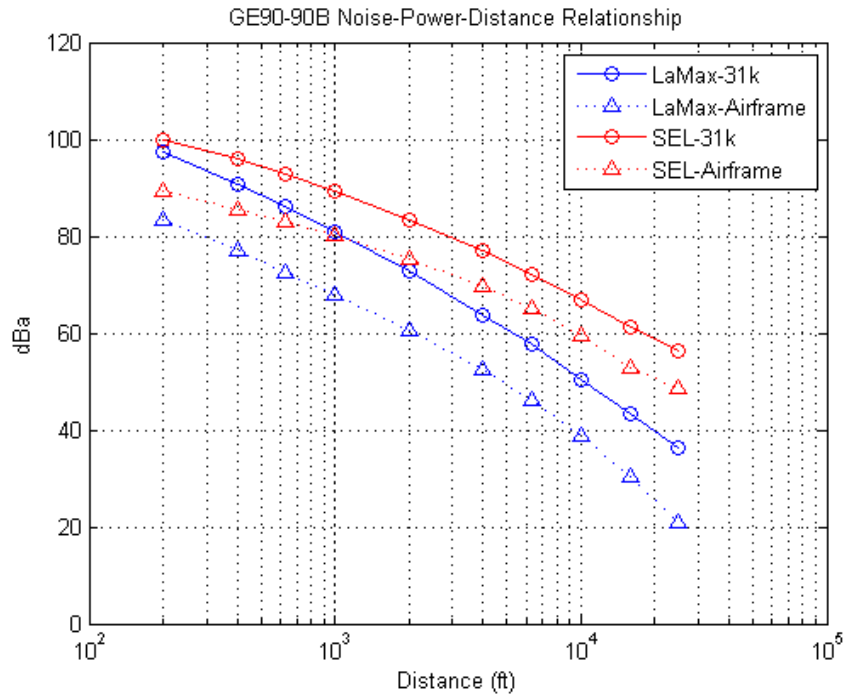


**Figure 5.3: Comparison of takeoff airframe NPD prediction from ANOPP and the takeoff NPD with 31,000 lbf of thrust per engine contained in the INM. The maximum A-weighted sound exposure, L<sub>A</sub>Max is shown in blue, and the Sound Exposure Level, SEL, is shown in red. The aircraft configuration for the Boeing 777-200 is slats takeoff, and flaps five-degrees.**

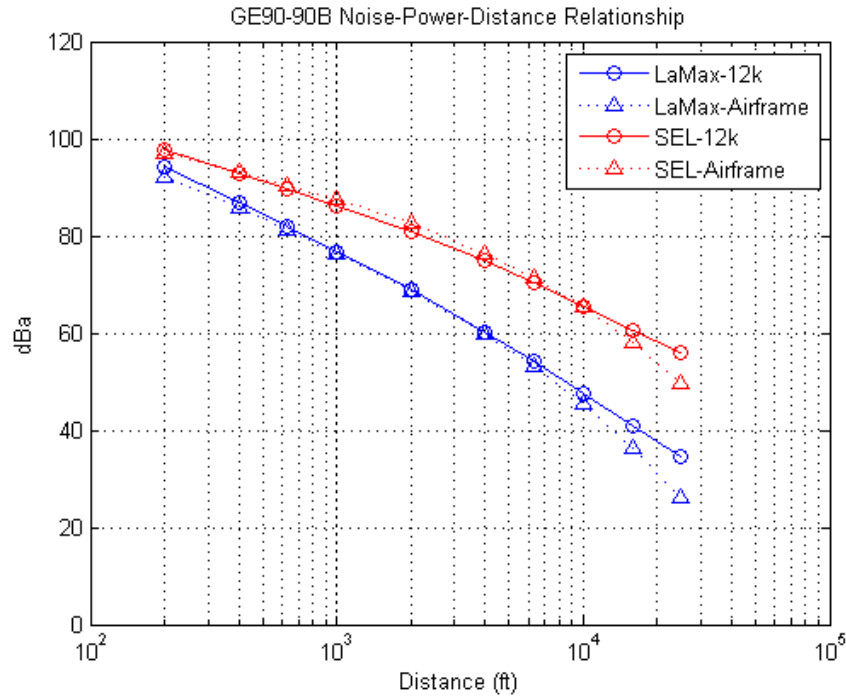


**Figure 5.4: Comparison of takeoff airframe NPD prediction from ANOPP and the landing NPD with 12,000 lbf of thrust per engine contained in the INM. The maximum A-weighted sound exposure,  $L_A\text{Max}$  is shown in blue, and the Sound Exposure Level, SEL, is shown in red. The aircraft configuration for the Boeing 777-200 is slats landing, flaps thirty-degrees, and landing gear deployed.**

From the landing configuration comparison, Figure 5.4, it is shown that the airframe noise signature predicted by ANOPP is quite close to the actual NPD for the aircraft. The SEL is noticeably over predicted by ANOPP at a distance between 1,000 and 5,000 feet. The error is about 1-2dBA or about 2-3% error; however, at other distances the error is smaller.

This method to predict the NPDs for the airframe enables a scaling of the actual NPDs in the INM to predict the changes of aircraft noise associated with the different configurations. The scaling is done by computing the NPDs for the original airframe configuration as well as the NPDs for the new configuration with the ANOPP code. The original NPDs from INM are then scaled according to Equation 5.1, which amounts to converting the noise metrics from logarithms back to frequency weighted sound pressure levels, added and/or subtracted, and then converted back to logarithms.

$$NPD = 10 \log_{10} \left[ 10^{\frac{INM\_NPD}{10}} - 10^{\frac{ANOPP\_AirFrame\_NPD}{10}} + 10^{\frac{ANOPP\_New\_AirFrame\_NPD}{10}} \right] \quad 5.1$$

The use of Equation 5.1 enables the NPDs to retain all of the correct engine noise content, but to modify the aircraft noise signature to account for different configurations.

## 5.2. Predicting Ground Level Noise

To predict the noise on ground or the airport community noise exposure only the aircraft trajectory and the NPDs are necessary. The INM is the tool that accomplishes this task. The basis of the INM is to create a grid along the ground near the airport. It then computes the distance between points on the ground and the aircraft for the entire trajectory. The minimum distance from the aircraft to each point on the ground is then selected. When the aircraft passes that point on the trajectory, the NPDs are interpolated by the thrust value the aircraft is using, which leaves a single noise-distance curve for that power setting. That singular noise-distance curve is then logarithmically interpolated with the minimum distance between the airplane and the point on the ground. This procedure computes the maximum noise exposure on the ground for the entire trajectory. There are numerous complications to this, for instance noise metrics that include time and exposure weightings. For the complete detailed procedure for computing the noise on the ground from the NPDs see the INM theory manual [45].



## CHAPTER 6: Noise Sensitivities

The purpose of the thesis is to compute the sensitivity of noise to low-speed aerodynamics, which will be the primary subject of this chapter. To compute a true sensitivity it is desirable to have a trajectory that consists of only one aircraft flap and slat setting. This way varying an aerodynamic model parameter, such as the flap setting, will influence the entire trajectory and there will only be one set of Noise-Power-Distance, NPD, curves. Conveniently, the FAA noise certification procedure requires a constant aircraft configuration for both takeoff and landing [60]. The only change allowed to the aircraft configuration is that during takeoff the airplane is allowed to immediately retract the landing gear. It should be noted that the certification procedures are unlike most normal aircraft departures and arrivals where the flap and slat settings are progressively changed.

The noise will be computed by the following procedure, first (1), the low-speed aerodynamic estimates will be made for the aircraft configuration, second (2), the NPD curves from the Integrated Noise Model (INM) will be scaled to compute the change in the aircraft noise signature, third (3), the flight trajectory will be computed, and finally (4), the INM will compute the noise at the certification points. That procedure takes about five-minutes on a standard Pentium-4 desktop computer. To prevent the need for running numerous cases for variations of each parameter in the low-speed aerodynamic tool, an initial sensitivity study was conducted to determine the parameters in the low-speed tool that have the largest effect on the aerodynamic estimates.

### 6.1. Low-Speed Aerodynamic Sensitivities

A design of experiments was created in which a baseline approximate Boeing 777-200 aircraft in the takeoff configuration was modified such that each of the sixty parameters to the low-speed aerodynamic model were studied at the  $\pm 1\%$  and  $\pm 10\%$  levels. Each set of aerodynamic results, drag polars, lift curves, and maximum lift coefficients were reduced to seven output variables. The output variables are angle of attack and drag coefficient at a lift coefficient of 0.7, angle of attack and drag coefficient at a lift coefficient of 1.0, and the angle of attack, lift

coefficient and drag coefficient at maximum lift. These seven output variables are computed by properly interpolating the lift curve and drag polar. A parameter is considered insignificant and will not be used in the noise sensitivity study if the maximum percent variation in any of the output parameters is less than one-tenth the input variation in percent. For instance, if the horizontal tail angle of incidence is increased by ten-percent and the maximum change in all of the output parameters is less than one-percent then that parameter will not be studied in the noise sensitivity study.

From the low-speed aerodynamic sensitivity study sixteen of the sixty parameters have a significant impact on the aerodynamics of the airplane. Those parameters are:

- 1) Wing angle of incidence
- 2) Wing Sweep
- 3) Aspect Ratio
- 4) Wing Planform Area
- 5) Wing Taper Ratio
- 6) Thickness-to-chord ratio at the wingtip
- 7) Percent span where the outboard flap ends
- 8) Inboard flap chord fraction
- 9) Outboard flap, inboard chord fraction
- 10) Outboard flap, outboard chord fraction
- 11) Outboard slat chord fraction
- 12) Horizontal tail Planform Area
- 13) Mach Number at which the drag polars are computed
- 14) Flap Deflection Angle
- 15) Slat Deflection Angle
- 16) Landing gear deployment

The noise sensitivity study will be conducted for both departure and arrival varying those sixteen parameters at the  $\pm 1\%$  and  $\pm 10\%$  levels, with the exception of landing gear deployment, which is a Boolean variable and will only be varied during approach.

## **6.2. Departure Noise Methodology**

The departure noise certification procedure is from the Federal Aviation Regulations, Chapter 36 Appendix B36.3 [60]. The procedure is as follows, (1) full-power takeoff, (2) full-power climb at a speed between  $V_2+10\text{kts}$  and  $V_2+20\text{kts}$  until an altitude of at least 684 feet if the

airplane has more than three engines, 853 feet if the airplane has three engines, and 984 feet if the airplane has less than three engines, (3) after crossing that altitude the airplane may decrease the power, but must maintain the a minimum power level such that the airplane attains a minimum climb gradient of four percent or maintains level flight with one-engine inoperative. The certification noise is then defined at two locations, a flyover point and a sideline point. The flyover point is a point directly underneath the aircraft flight path at a point 21,325 ft (6500m) from the start of the takeoff roll. The sideline point is defined as the maximum noise point on the ground along a line that is parallel to the flight path but located 1,476 ft (1450m) laterally from the projection of the flight path on the ground. The takeoff and sideline points are show schematically in Figure 6.1.

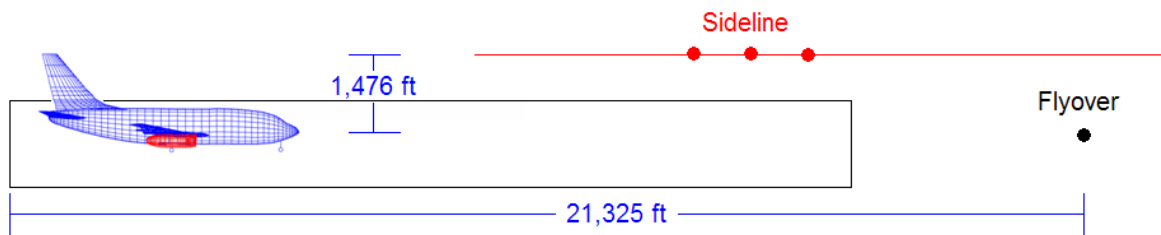


**Figure 6.1: Schematic showing the takeoff noise certification points.**

When an aircraft is being certified the aircraft manufacturer will determine what the optimum altitude is for minimum noise at the certification points. For instance, a Boeing 777-200 has two engines, so it is allowed to reduce power at any altitude above 984 feet. There is actually an altitude at which the total of the flyover and sideline noise will be the least, and this will typically be the altitude at which the pilots reduce the engine power during the certification test. These altitudes are proprietary to the aircraft manufacturer so it is necessary to sweep all of the likely altitudes. For the Boeing 777-200 that sweep revealed the cutback altitude is likely about 1,500 feet. The results of the estimates from the noise methodology used and the certification values for the Boeing 777-200 are shown in Figure 6.2. All of the certification noise values used are from the FAA Advisory Circular, AC36-1H, and are in EPNdB [61]. The only difference between the certification procedure and the procedure used in this analysis is that the engine out performance is unknown, and accordingly the four-percent climb gradient is used exclusively.

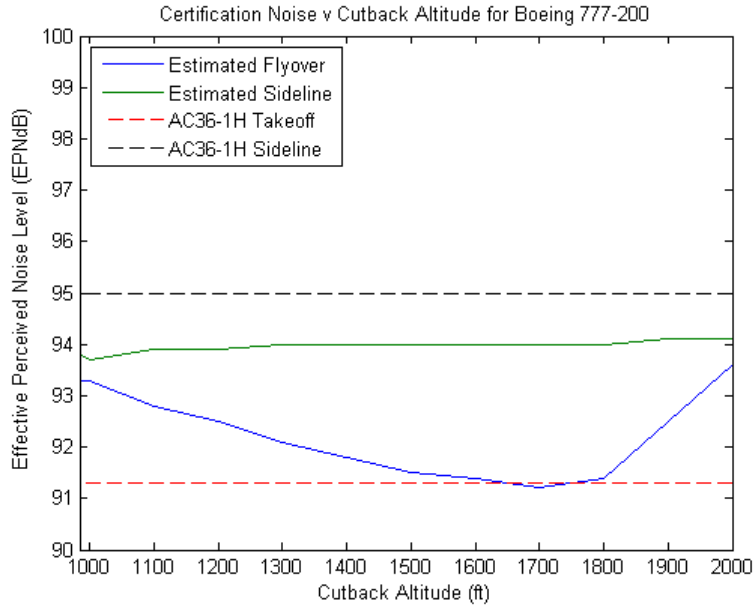


**Figure 6.2: Estimates of Flyover and Sideline noise for the Boeing 777-200 with various cutback altitudes, and a comparison to the actual certification noise values.**

A comparison between the certification noise values and the estimates from the noise prediction methodology are shown in Table 6.1. The results show that the noise methodology predicts the flyover noise within 0.1 EPNdB and the sideline noise to within 1.0 EPNdB. These results show that the model is working well, and that the sensitivity study conducted with this model will provide meaningful results.

	<b>Flyover Noise</b>	<b>Sideline Noise</b>
AC36-1H, Actual Values	91.3 EPNdB	95.0 EPNdB
Estimates	91.2 EPNdB	94.0 EPNdB

**Table 6.1: Comparison of 777-200 certification noise and estimates from the noise prediction methodology [61].**

### 6.3. Departure Noise Sensitivities

The departure noise is insensitive to the airframe configuration. This is primarily because the engine noise is 22dB louder than the airframe noise at full-power. This means that any changes to the airframe signature will be dominated by the engine noise and will not be noticed in a noise analysis. The only possible way for airframe changes to impact noise will be in flight path changes, for instance if the airplane is at a lower altitude at a certain point on the

trajectory than in the baseline case it will be louder. A sensitivity study was conducted with each of the fifteen continuous low-speed aerodynamic parameters that were shown to impact the aerodynamics. Each variable was tested at the  $\pm 10\%$  levels and the percent change in the sum of the flyover and sideline noise is shown in the tornado plot in Figure 6.5. The insensitivity of takeoff noise to airframe configuration is demonstrated as the largest change in noise is less than 0.2%. The two parameters with the largest impact are the aspect ratio and the planform area. Increasing both the aspect ratio and planform area will improve the climb capabilities of the airplane and decrease the noise by increasing the airplane's climb gradient.

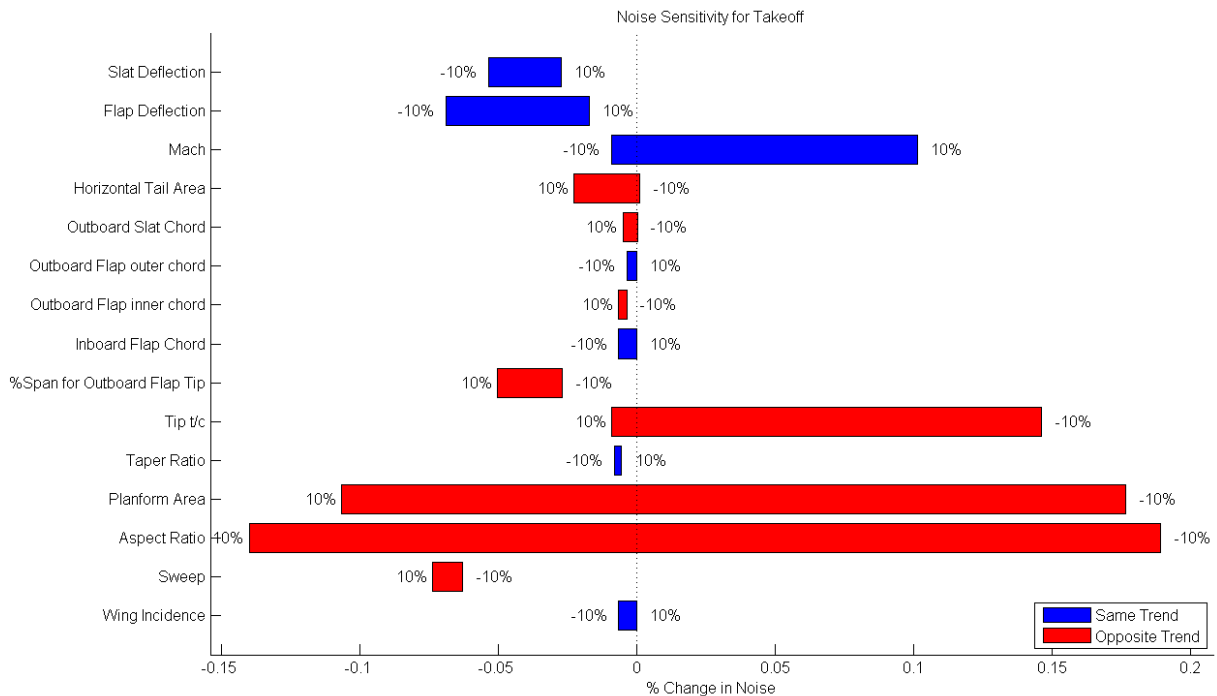


**Figure 6.3: Tornado plot of takeoff noise sensitivities. An important note is that the Mach number in the figure is not the Mach number flown, it is the Mach number at which the drag polar was computed.**

A more detailed study of designing departure trajectories for minimum noise will be presented in the next chapter.

The results of the aircraft design optimization study by Antoine, et al. [5] showed that the noise optimal aircraft had increased planform area, aspect ratio, horizontal tail area, and engine bypass ratio. It also had a decreased wing sweep. The sensitivity study conducted herein agrees with increasing the planform area, aspect ratio, and tail area. The tail area sensitivity found in this study is small, and the likely reason for an increase in tail area in the Antoine et al. paper is

to compensate for engine-out yaw moment from the large high-bypass ratio engine, and not for noise considerations. The only qualitative difference between the two studies is that in the Antoine paper the sweep changed significantly from 33.70 degrees to 14.25 degrees by redesigning the minimum cost airplane for minimum noise, and this study found sweep to be fairly insensitive between 28.48 degrees and 34.80 degrees. The likely cause of this would be a non-smooth design space, where increasing any one parameter may either increase or decrease noise depending on the local design sensitivity. It is likely that the 777-200 design is at a local minimum for cost where local sensitivities are not representative of global design changes.

#### 6.4. Approach Noise Methodology

The approach noise certification procedure is comparatively simple when compared to the departure noise procedure. The aircraft must maintain a velocity at least 1.23 times its stall speed,  $V_s$ , while it flies a three-degree glide slope to, and lands at a point 984 feet (300 m) from the beginning of the runway. The noise measured at a point 6,562 feet (2,000 m) from the beginning of the runway, or 7546 feet (2,300 m) from the touchdown point is the approach noise [60]. The procedure is shown schematically in Figure 6.4.

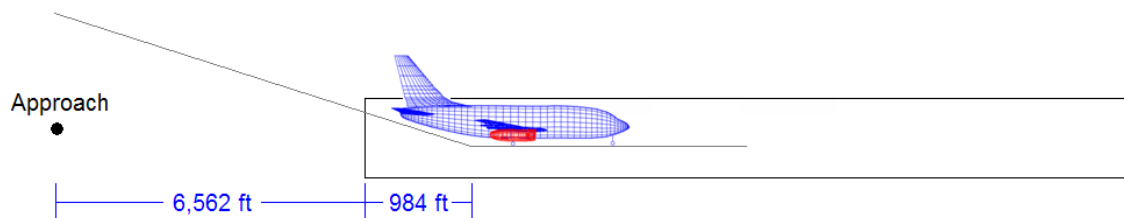


**Figure 6.4: Schematic of approach noise certification point.**

For the 777-200 approach, the certification noise is 97.8 EPNdB [61], the estimate from the noise methodology is 98.3 EPNdB which is in error of 0.5 EPNdB. Again the noise model accurately estimates the noise for the Boeing 777-200.

## 6.5. Approach Noise Sensitivities

The approach noise analysis sensitivity included two additional parameters, the approach flight path angle and the approach velocity multiplier, so a comparison could be made with the work of Hileman et al. [13] developing approach procedures with minimum noise. The approach flight path angle, with a baseline of 3 degrees was analyzed at  $\pm 10\%$  or 2.7 and 3.3 degrees. Similarly the approach speed multiplier, with a baseline of 1.3 was tested at  $\pm 10\%$  which is 1.17 and 1.43. The other fifteen important continuous low-speed aerodynamic parameters were also tested at  $\pm 10\%$ , and landing gear was tested deployed and stowed. The stowed configuration of the landing gear would represent deploying the landing gear when crossing the threshold, which may worry some pilots and would require software changes in the current aircraft fleet. The results of the approach sensitivity analysis are shown in Figure 6.5.

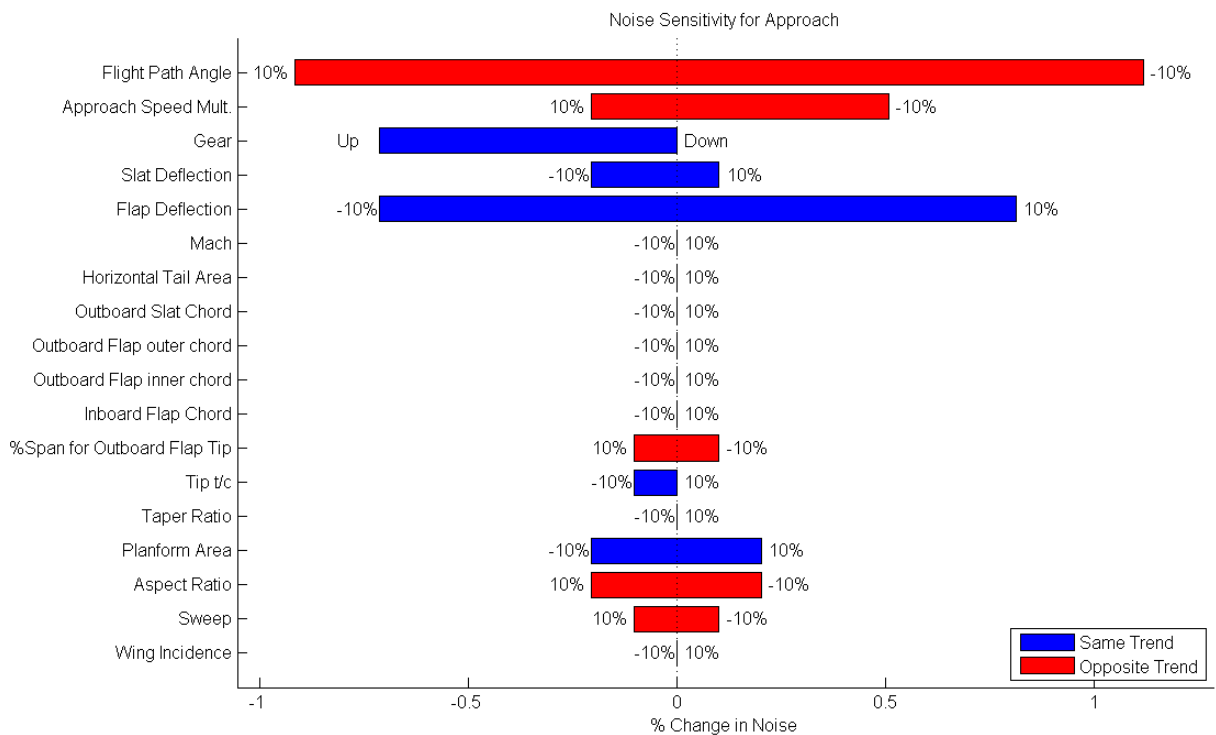


**Figure 6.5: Tornado plot of approach noise sensitivities. Note: Mach number in the sensitivity is the Mach number at which the drag polar is computed and not the Mach number at which the approach is flown.**

The two most sensitive parameters for approach noise are the speed and the flight path angle. Otherwise, with the exception of flap deflection angle, this sensitivity analysis again shows that changing the aircraft geometry has about a 0.20% change in the noise. There are some findings

here that are counterintuitive; for instance, it would be expected that approach noise would be sensitive to the airframe noise signature as there is considerably less thrust on approach than on takeoff. However, the sensitivity showing that an increase in approach speed decreases noise shows that this is not true, and the engine noise plays a considerable role in the approach noise.

For the airplane to fly a fixed angle flight path the airplane angle of attack is set by the aircraft velocity and the engine thrust must be adjusted based on the lift to drag ratio at that angle of attack. Essentially, the angle of attack will set the airspeed and the thrust will determine the flight path angle flown, higher power shallows the angle and lower power increases the steepness. For the baseline case, a three-degree flight path angle, the 777-200 requires about 30,000 lbf of thrust or 32% throttle to fly at  $1.3 \cdot V_s$ , or 1.3\*the aircraft stall speed in the landing configuration. A second study was conducted to determine at what airspeed the minimum noise occurs, if a minimum is found it means that approach thrust dominates the noise because increasing speed would decrease the required thrust. In contrast, if the airframe noise were dominating, then the airplane noise will increase with increasing speed. The results of the study are shown in Figure 6.6.

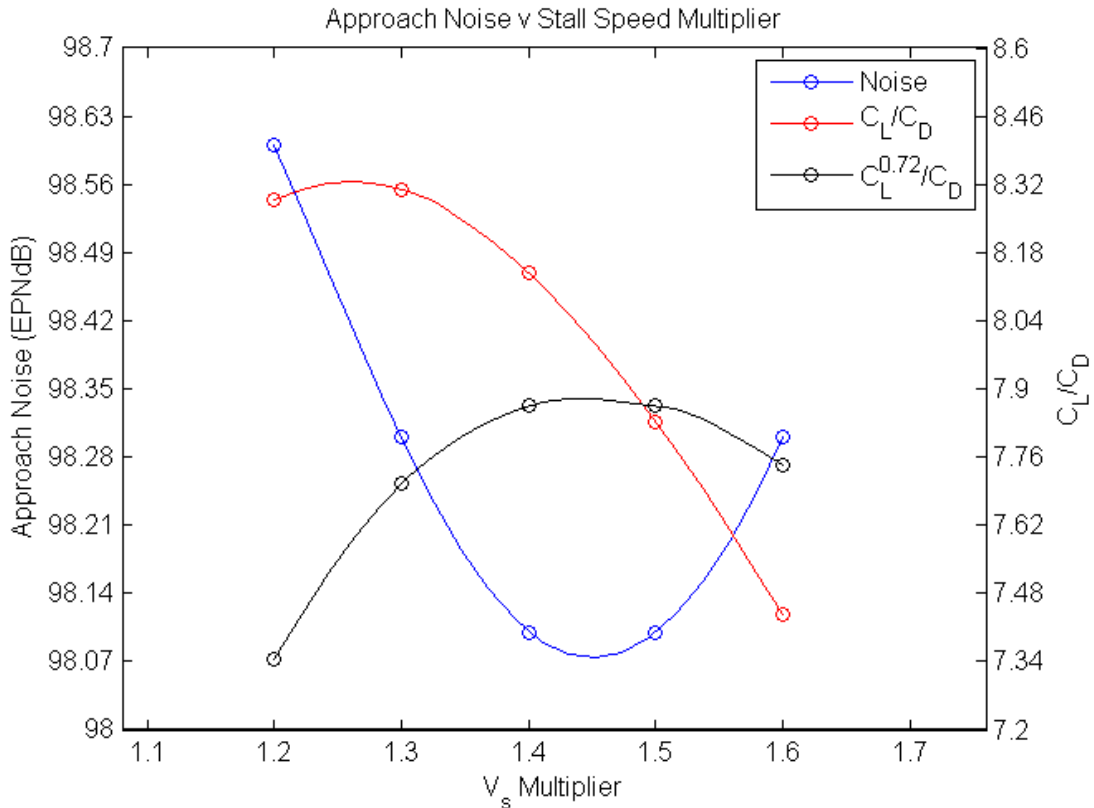


**Figure 6.6: Changes in approach noise due to increasing the approach speed.**

Figure 6.6 shows that by increasing approach speed from  $1.3V_s$  to  $1.42V_s$  the approach noise decreases by more than half of an EPNdB. This flight speed corresponds to maximizing  $C_L^{0.72}/C_D$ , which may only apply to the 777-200 in the approach configuration, but it is worthwhile noting that this exponent is nearly halfway between the maximum range and maximum endurance speeds. Looking at this more closely, the 777-200 needs at least 30,000 lbf of thrust to fly the 3-degree approach. With this thrust level the combined noise of the engine and airframe is 96.88 EPNdB at a distance of 400ft; whereas, the prediction of the airframe noise signature is only 93.88 EPNdB, which is 3 EPNdB lower. This means the amplitude of the noise from the engine and the airframe is twice that of the airframe alone. Accordingly, this analysis suggests that increasing the approach velocity will decrease the noise for a modern commercial aircraft, and any method to decrease the approach thrust will minimize approach noise.

These findings, that increasing the approach speed decrease noise, contrast the findings of Hileman et al. [13]. In that paper, it was found that decreasing approach speed decreases noise, which is the case for an aircraft where the airframe noise is the dominant source of noise. The aircraft in that paper is a BWB and has its engines mounted above the body so the engine noise is shielded from the ground. This means that the approach noise from the current fleet is largely dominated by the thrust required to maintain the 3-degree glide slope at a slow speed; however, for an entirely lifting configuration thrust is no longer dominating because of the considerably improved lift-to-drag ratio of over twenty compared with 8.3 in the current fleet. For both configurations increasing the approach angle reduces the approach noise. This is because a steeper approach angle keeps the airplane higher above the ground when it is outside of the airport boundary allowing the sound waves to propagate farther from the source and become weaker before they reach the ground.

A final approach noise study was conducted to determine the best combination of directions to change the dominant parameters in approach noise. All of the combinations of the flap deflection angle, slat deflection angle, approach flight path angle, and approach speeds were tested at  $\pm 10\%$ . It was found the best combination for minimum noise was to leave the flap and settings at the baseline and to increase both the approach speed and the flight path angle by 10%. This setting decreased the approach noise by 1.1 EPNdB or -1.12%. Similarly, the worst combination for the maximum noise was with the flaps and slats at the baseline but the approach speed and flight path angle decreased by 10%. This setting increased approach noise by 1.5 EPNdB or 1.53%.

## CHAPTER 7: Trajectory Optimization

It is essential for airlines to know the trade between time to climb, fuel burn, and noise, as these are all important factors in determining the cost and impact of a flight. Time is an important cost element as it determines the price of using the aircraft, the amount of maintenance the airplane needs, and the flight crew wages. Fuel consumption is also an important driver of a flight cost, and as Figure 7.1 shows, it is becoming an increasingly large fraction of the total airplane operational costs. Fuel burn is also directly related to environmental impacts such as carbon dioxide and global warming. Noise impacts costs through airport fees as many airports are now charging depending on how much noise an aircraft emits. In addition, there are procedural restrictions on aircraft flight paths to reduce noise; these impact cost through increased fuel burn and time. Determining the Pareto Front of departure trajectories for minimum time to climb, minimum fuel burn, and minimum time to climb will enable aircraft operators and airport planners to develop cost minimizing procedures or to properly monetize penalties to force reductions in noise emissions.

The trajectory optimization is computed for the Boeing 747-200 airplane which is largely out-of-service for passenger use, but is still used commonly for freight. The reason this aircraft was used is the availability of engine performance tables that enable the proper thrust lapse and specific fuel consumption to be computed for the engine. The methodology used for the optimization should be directly applicable to any other turbofan powered subsonic commercial transport aircraft in the current fleet. The results obtained should also show trends that are similar throughout the current fleet; however, the exact tradeoffs and trajectories will vary.

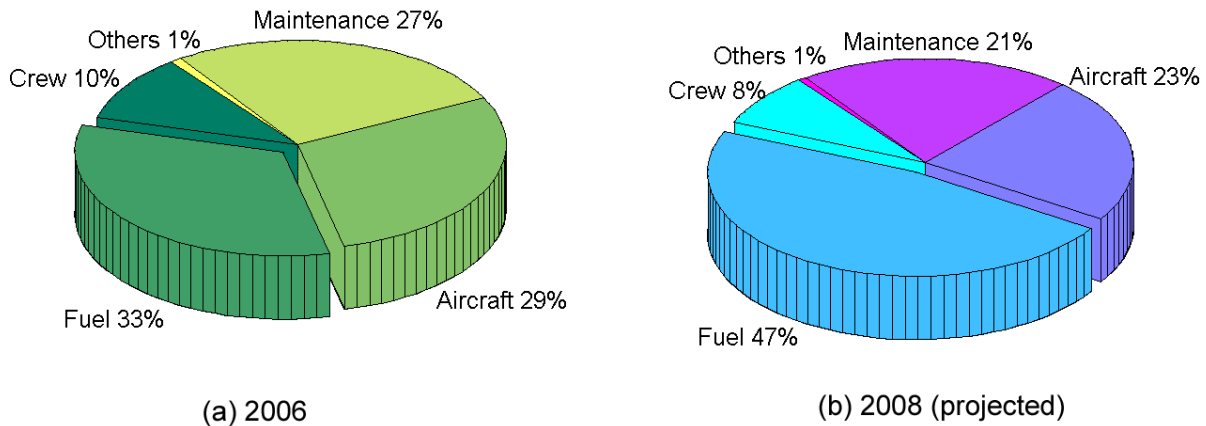


**Figure 7.1: Typical operational cost breakdown for a Boeing 747-200 used for passenger service in 2006, and the projected cost breakdown for 2008 [65].**

## 7.1. Problem Setup

The goal of this optimization is to find the Pareto Front of all trajectories a pilot could fly with a 747-200 in terms of minimum time to climb, minimum fuel burn, and minimum 55 EPNdB noise contour area. Essentially the front shows all of the trajectories for which none of the objectives could be improved without worsening at least one of the other objectives. The trajectories computed will all be two-dimensional, which means the aircraft are all assumed to have a straight-out departure and not turn below 10,000 feet. In an optimization of minimum population noise exposure it would be necessary to model turns; however, in the case of minimum land exposure this simplification will not cause a significant difference. The two-dimensional simplification means the pilot only has three inputs to the aircraft, the throttle setting, the pitch attitude or airspeed, and the flap setting. The throttle setting is a continuous variable between engine idle, which is about 7% of maximum thrust, and maximum thrust. The maximum thrust is a function of both the aircraft speed and altitude and is computed from engine performance tables from Pratt and Whitney [46]. The aircraft pitch attitude is set by the airspeed, so pilot will trim the airplane to fly at a specific airspeed and then power additions or reductions will set the rate of climb. The final parameter the pilot can change is the flap setting, and there are specific detents at which the pilot can position the flap lever. For the 747-200 the flaps can be positioned in one of four detents for takeoff: Up, 5-degrees, 10-degrees, and 20-degrees. Accordingly, this variable is modeled as a discrete variable between zero and three.

The first step in determining the best departure trajectory for minimum time to climb, fuel burn, and noise is to parameterize the trajectory. The climb procedure is separated into five segments, (1) takeoff and initial climb, (2-4) three constant velocity climb segments, and (5) a final enroute climb segment with the aircraft in the clean configuration that ends when the aircraft reaches 10,000 feet. For each of the climb segments there are four variables, pilot inputs, throttle setting, airspeed, and flap setting, and additionally the altitude at which the climb segment ends or transitions to the next segment. Some of the climb settings have fewer design variables, for instance for the first segment, takeoff and initial climb, there are only three design variables, the takeoff drag polar, the throttle setting, and the altitude at which the initial climb ends. This is because the FARs require the initial climb to be at an airspeed between  $V_2+10\text{kts}$  and  $V_2+20\text{kts}$ , so the airspeed is constrained in this model as in the INM to be at  $V_2+15\text{kts}$ . Also, the initial climb altitude must be at least 684 feet for the 747-200 as this is set by the FARs for airplanes with more than three engines [60]. Similarly, for the final climb segment the flap setting must be flaps up and the segment must end at 10,000 feet, so the only variables for this procedure are the airspeed and the throttle setting. For the three in-between climb segments all four variables must be set. This means there are a total of 17 design variables, and four pilot inputs during the climbing procedure. A schematic of the climb procedure is shown in Figure 7.2. Since all of the segments are modeled as constant velocity, if the velocity between the two segments varies by more than ten knots, an acceleration procedure is inserted. For the full model this would be unnecessary; however, for the linear model a better representation of the flight track is obtained. The acceleration procedure uses the aircraft configuration, power and flap setting from the previous segment, but maintains a climb rate that is sixty percent of what the airplane is capable of achieving until it reaches the velocity of the next flight procedure.

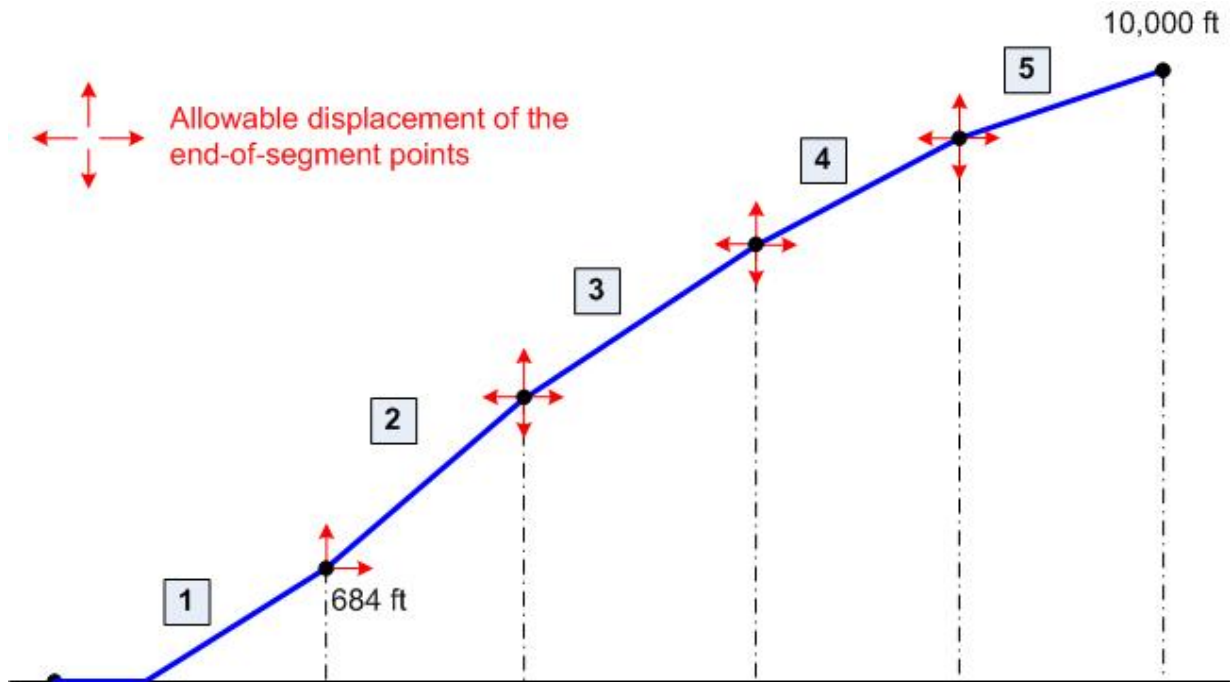


**Figure 7.2: Schematic showing divisions of the departure trajectory enabling the parameterization of the trajectory for optimization.**

There are a collection of bounds and constraints on the design variables. For takeoff it was assumed that any de-rate would be less than 25%, so the takeoff thrust would be between 75% and 100% of rated takeoff thrust. The other constraints are (1) the aircraft cannot stall, (2) the aircraft has a maximum dynamic pressure of 270 psf, (3) the flap setting is either decreasing or remaining unchanged (configuration approaching cruise configuration), (4) the airplane has a positive flight path angle, so it is always climbing, and (5) the altitudes at which the procedures change are always increasing.

## 7.2. Optimization Method

This optimization is difficult for numerous reasons. First, (1) the design space is a mix of discrete and continuous variables. Second, (2) most of the constraints cannot be violated, so methods such as sequential quadratic programming (SQP) may allow slight constraint violation and this is inaccurate. Third, (3) the design space contains variables of dramatically differing scales, for instance the throttle setting varies between zero and one, velocity between three hundred and seven hundred, and altitude varies between zero and ten-thousand. To properly

solve this would require rescaling the problem after every few optimization iterations. Fourth, (4) the objective space is noisy and characterized by many local minima. This is because there is a local optimum of velocity for each drag polar and altitude combination. Accordingly, the optimizer will get trapped at numerous transition altitudes as well as velocities. Fifth, (5) the objective space is discontinuous. This is because a velocity used for climb to 8,000 feet may be below the stall speed at 10,000 feet. In addition, a velocity above the stall speed for one flap setting may be well below the stall speed for the next flap setting. Similarly, the variations of both thrust and velocity make it so there is a band of feasibility, so both variables may need to be properly adjusted such that the aircraft doesn't overspeed or stall.

For a single-objective optimization of time to climb four optimization methods were attempted, SQP, non-derivative direct search (Nelder-Mead Method), particle swarm optimization (PSO), and a genetic algorithm (GA). SQP was used in conjunction with fifteen different initial conditions corresponding to all of the possible aircraft flap configurations (assuming takeoff occurs with flaps 10 degrees or less). The best time to climb found was 311.97 seconds. The same procedure was attempted with the non-derivative direct search and the best time to climb found was 318.8 seconds. PSO, like the GA, is able to incorporate the discrete variables, and the best time to climb found was 318.7 seconds. The GA, however, found the best time to climb of all of the methods of 307.8 seconds. The problem with the GA is that it took twenty hours to run on a Pentium 4, whereas PSO only took four hours, and the directional search techniques took only about one hour.

Another benefit to the GA is that because it uses a population instead of a single point, an entire Pareto Front can be found during one optimization run as opposed to using many optimizations to find individual points along the front. With all of these benefits of a GA, the long-run time was ignored and a multi-objective GA was created to optimize trajectories for minimum time to climb, minimum fuel consumption, and minimum noise exposure area. The fitness function used for the GA was the number of population members dominated, and the likelihood of reproduction was the fitness of an individual population member normalized by the sum of the entire population fitness. If any constraints were violated, the population member was flagged and the fitness was automatically set to zero. The other parameters of the

GA worth noting are that, the probability of a crossover during mating is one, the probability that a bit is mutated is 0.03, and four-percent of the most-fit members of the population are automatically carried over to the next generation. The seventeen elements of the design vector are modeled as binary between their upper and lower bounds. The drag polars require two bits to model the four possible drag polars, the continuous variables such as velocities and altitudes are modeled with sixteen bits, and the throttle settings are modeled with only five bits such that the throttle variations are coarse and represent actual pilot capabilities.

The GA was found to converge fastest when the initial population was small, and the algorithm ran for about between ten and twenty-five generations on continuously increasing generation sizes. The GA was used twice to find the Pareto Front of the departure trajectories, once for a 747-200 departure with a takeoff weight 725,000 lbm and again for a departure with a takeoff weight of 550,000 lbm. The 747-200 with the JT9D-7A engines used has a maximum takeoff weight of 734,000 lbm, so the two takeoff weights used represent an almost full takeoff and a lightly loaded takeoff. The average load factor for a 747-200 is 87.4%, although load factor does not directly relate to takeoff weight, an estimate for the takeoff weight for that load factor is about 700,000 lbm [65].

### 7.3. Results

The reference procedure for the 747-200 is the standard departure contained in the INM with a takeoff weight of 725,000 lbm. The standard procedure is explained in Table 4.3, and is plotted Figure 4.7. For the standard procedure, Table 7.1 contains the values of the objective functions. The key result of this analysis is that there is a family of trajectories that mutually reduce time to climb by two minutes, fuel burn by 1,300 lbm, and noise exposure area by 100 square miles when compared to this standard departure.

<b>Output</b>	<b>Full-Model</b>	<b>Linear-Model</b>	<b>%-Difference</b>
Time to Climb	447.6 seconds	428.7 seconds	4.3%
Fuel Burn	6,651 lbm	6,363 lbm	4.3%
Noise (55 EPNdB Exposure Area)	470 mi <sup>2</sup>	455 mi <sup>2</sup>	3.4%
Solution Run Time	350.3 seconds	23.2 seconds	93.3%

**Table 7.1: INM standard departure for Boeing 747-200 figures of merit.**

The GA found ten points on the final Pareto Front for takeoff with a gross weight of 725,000 lbm. The points on the Pareto front are presented in Table 7.2.

Point	Time to Climb (s)	Fuel Consumption (lbm)	55 EPNdB Contour Area (mi <sup>2</sup> )
<b>1</b>	<b>311.2</b>	<b>5,134</b>	<b>363</b>
2	312.0	5,132	363
3	312.1	5,156	363
4	312.3	5,159	363
5	312.5	5,167	362
6	312.6	5,147	363
7	312.8	5,142	363
8	312.9	5,138	362
<b>9</b>	<b>328.6</b>	<b>5,272</b>	<b>357</b>
<b>10</b>	<b>356.2</b>	<b>5,085</b>	<b>364</b>

**Table 7.2: Points along the Pareto Front for Boeing 747-200 departure trajectories with a takeoff weight of 725,000 lbm. Points in bold represent the anchor points of the trajectories.**

All of the key aspects of the trajectories corresponding to the anchor points, or minimum points for each objective, for the 747-200 with a takeoff weight of 725,000 lbm are plotted in Figure 7.3. For the minimum time to climb trajectory, as would be predicted by intuition, the aircraft climbs with full-throttle, and at a velocity close to the maximum lift to drag ratio. For the minimum fuel burn trajectory, the airplane uses about fifteen percent less power and flies at a velocity that minimizes the lift to drag ratio divided by the specific fuel consumption. For both the minimum time to climb and minimum fuel burn trajectories, the airplane does not use flaps. The likely reason for this is that the airplane attains the highest lift to drag ratio that it is capable of with the flaps up. An interesting aspect to this is that for takeoff the airplane requires a longer time and distance to get off the ground without flaps than it does with flaps. However, the increased lift to drag ratio for the initial climb segment more than compensates for that difference. The minimum noise trajectory is quite different from the minimum fuel burn and minimum time to climb trajectories. The optimum trajectory has a high takeoff flap setting, with flaps deployed twenty degrees. However, this enables the airplane to takeoff in a short distance and at a lower velocity than either of the other two trajectories. After the aircraft completes its initial climb segment, the trajectory behaves much more like the minimum time and fuel burn trajectories, and in fact, the trajectories are nearly parallel after that point. The

change caused by the higher takeoff flap setting is that the trajectory is always at a higher altitude than the other two trajectories. The increased altitude enables the mechanism of atmospheric absorption and propagation to reduce the amount of noise that reaches the ground. Also for the minimum noise case, the throttle setting is at an intermediate level between the two values obtained when minimizing time to climb and fuel burn. This throttle setting is likely to provide the proper trade between generating engine noise and obtaining enough altitude for the noise generated to be dissipated by the atmosphere. For the minimum noise case the velocity is also lower than the minimum time and minimum fuel burn trajectories. This effect occurs because by flying slowly, a higher fraction of the engine's power can be used for climbing, and the airplane is able to climb more steeply. A comparison of the noise contours for each of the trajectories is shown in Figure 7.4.

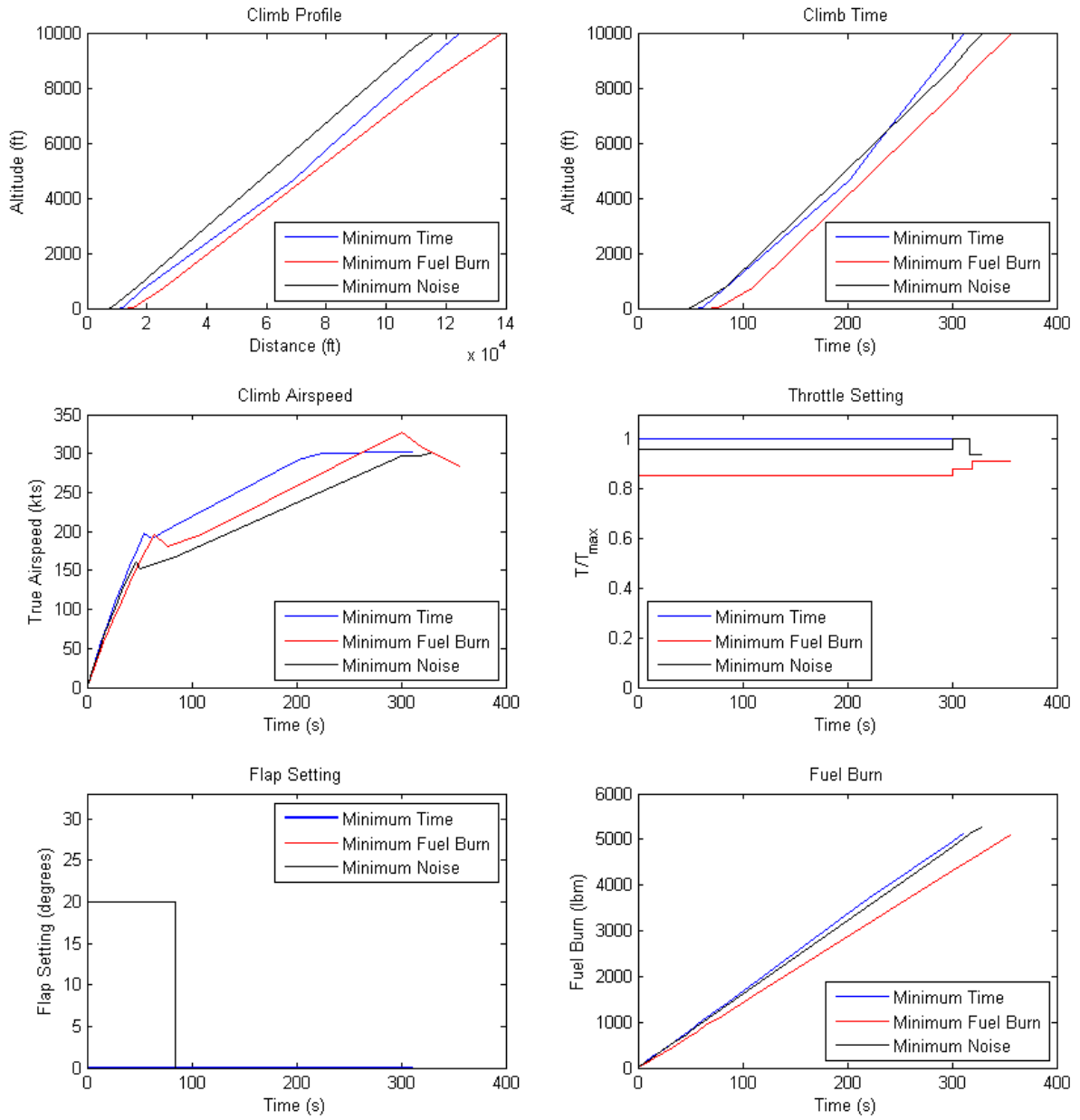


**Figure 7.3: Plots comparing the trajectories for minimum time to climb, minimum fuel burn, and minimum noise for a 747-200 with a takeoff weight of 725,000 lbm.**

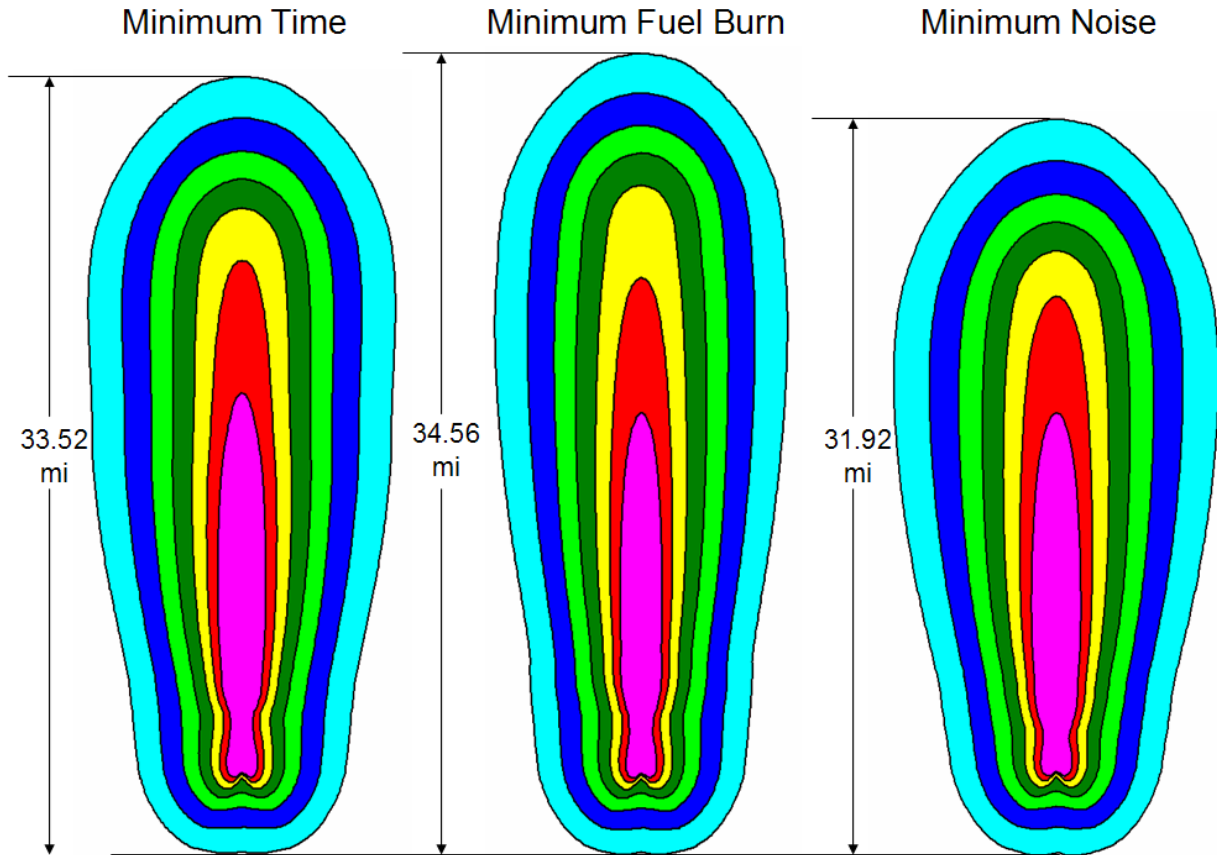


**Figure 7.4: Plots of the noise contours for each of the trajectories corresponding to minimum time to climb, minimum fuel burn, and minimum noise. The contour bands correspond to 55, 60, 65, 70, 75, 80, and 85 EPNdB.**

A second optimization study was conducted with a different aircraft takeoff weight, 550,000 lbm instead of 725,000 lbm. The Pareto Front for the optimal trajectories is presented in Table 7.3. The trajectories that minimize each of the objectives are plotted in Figure 7.5. The trajectory for the minimum time to climb is essentially unchanged with the exception of a velocity scaling. However, the trajectories for minimum noise and minimum fuel burn are substantially different from the departure with the nearly full load, and in fact become much more similar. For both, instead of having reduced power from takeoff throughout the climbout, the trajectories now have a substantial cutback and reapplication of thrust. Also, the minimum fuel burn trajectory uses ten degrees of flaps for the initial takeoff segment, whereas before it did not use flaps, and the flap setting for the minimum noise departure decreased from twenty degrees to ten degrees.

Point	Time to Climb (s)	Fuel Consumption (lbm)	55 EPNdB Contour Area (mi <sup>2</sup> )
<b>1</b>	<b>208.3</b>	<b>3,413</b>	<b>264</b>
2	210.1	3,410	263
3	212.2	3,362	243
4	214.3	3,071	234
<b>5</b>	<b>214.4</b>	<b>3,027</b>	<b>245</b>
6	214.6	3,071	234
7	219.6	3,051	239
<b>8</b>	<b>220.7</b>	<b>3,045</b>	<b>232</b>

**Table 7.3: Pareto Front for takeoff departures of a Boeing 747-200 with a takeoff weight of 550,000 lbm, points in bold represent the anchor points.**

Although the trajectories for the different takeoff weights are quite different, the optimized results are almost linear with takeoff weight. For a sample trajectory, the three objectives were computed for three different takeoff weights, and are shown in Table 7.4. The local derivatives of time to climb, fuel burn, and noise exposure were taken with respect to takeoff weight, and these derivatives were used to predict the optimum results for the 550,000 lbm takeoff from the 725,000 lbm takeoff. The results, shown in Table 7.5, show that all of the objective functions are nearly linear in takeoff weight; specifically for fuel burn and noise exposure the linear estimate is very accurate and is within three percent of the actual optimum. Accordingly, the objectives are very nearly linear in takeoff weight even though the trajectories are significantly different.

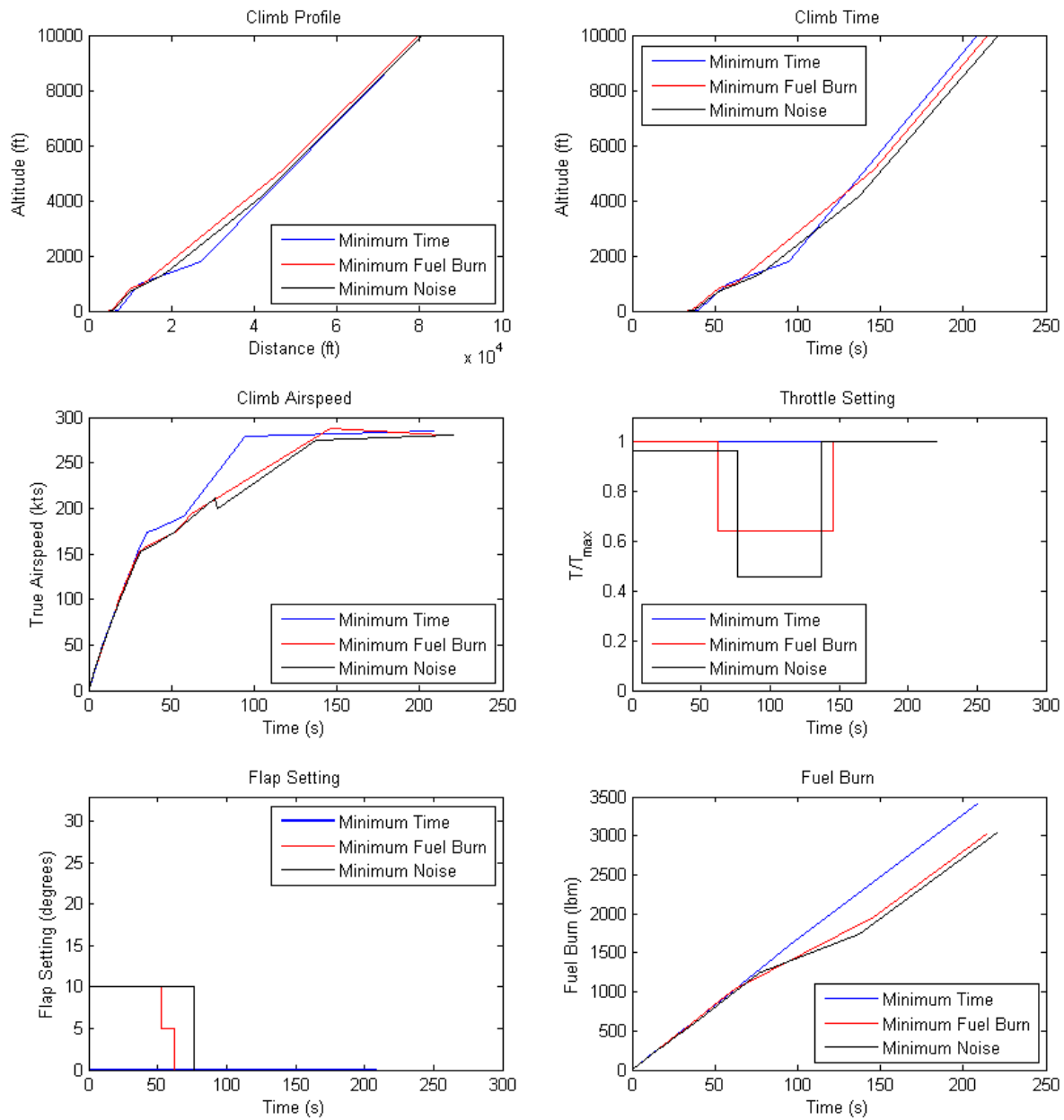


Figure 7.5: Plots showing the trajectories for minimum time to climb, minimum fuel burn, and minimum noise exposure area for a Boeing 747-200 with a takeoff weight of 550,000 lbm.

Takeoff Weight (lbm)	Time to Climb (s)	Fuel Burn (lbm)	Noise Exposure (mi <sup>2</sup> )
700,000	297.3	4,891.3	349
725,000	315.2	5,186.4	365
750,000	334.8	5,502.6	384

Table 7.4: Results of flying the same departure procedure with an aircraft of different takeoff weights.

	<b>Predicted Minimum</b>	<b>Actual Minimum</b>	<b>% Difference</b>
Time to Climb (s)	179.9	208.3	13.6
Fuel Burn (lbm)	2,945	3,027	2.69
Noise Exposure (mi <sup>2</sup> )	232	232	0.43

**Table 7.5: Results predicting the objective function values at another takeoff weight using a linear approximation.**

The results of this optimization are compared to the work of Wijnen and Visser who optimized 737-300 departure trajectories for minimum population noise exposure and fuel burn [15], [16]. The results of their optimization trajectories are quite similar to the trajectories for the 747-200 departure for a takeoff weight of 550,000 lbm, and quite different from the trajectories for the 725,000 lbm departure. In their work, the 737 had a gross weight of 123,000 lbm, which depending on the aircraft's engines was between 37% and 45% of the airplane's useful load. For the two 747 departures studied herein, 550,000 lbm corresponds to 35% of the useful load and 725,000 lbm corresponds to 91% of the useful load. From these results, it appears the different optimization methodologies and results affirm each other. A slight difference between the two methods is that in the Wijnen and Visser work, the minimization was for population exposure and not land exposure, so the cutback procedure is more complicated, although quite similar in the overall behavior.

#### **7.4. Maintenance Costs**

Turbine life is another important component when developing departure procedures. Most airlines de-rate their engines, or reduce the maximum takeoff power the airplane can use in order to increase the engine life. For instance, the CF6-80, which is similar in application to the JT9D used in this study, is commonly de-rated from 63,000 lbf of thrust to 53,000 lbf, or 14%. Another engine, the CFM56, is typically used for shorter flights where takeoff is a significant portion of the flight, can be de-rated even more from 27,000 lbf to 18,000 lbf, or 29%. This is because de-rating the engine reduces the temperature that the turbine is exposed to and increases the turbine life. The turbine section of the engine is one of the most life-critical portions of the engine as it subjects materials to both high temperatures and high stresses. This

section will show that even small changes in temperature can have significant impacts on turbine life, and accordingly engine maintenance costs.

Using an engine cycle model for the JT9D engine an estimate of the turbine inlet temperature as a function the engine de-rate or power setting was created. The results are presented in Figure 7.6, and show that for each 1% of thrust the engine is de-rated the maximum temperature the turbine is exposed to decreases by 5.90K [67].

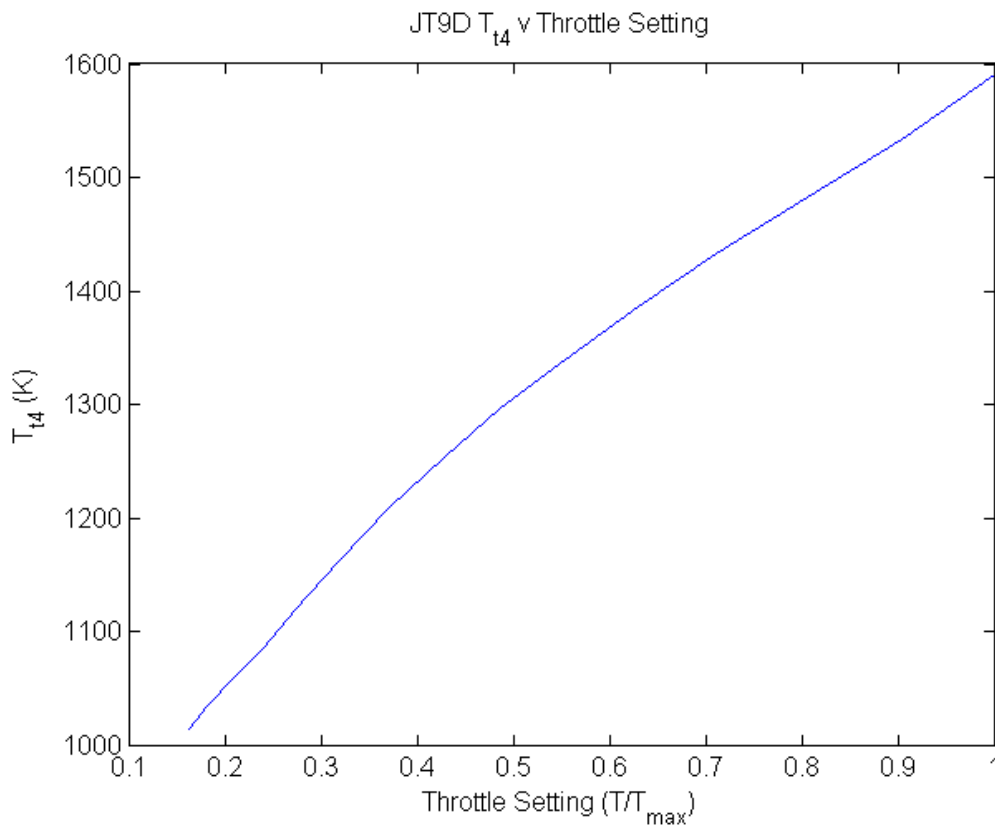


**Figure 7.6: Estimated change in turbine inlet temperature caused by reducing the takeoff power for the JT9D-7A engine for hot-day sea-level static conditions [67].**

To determine the benefit of reducing the turbine inlet temperature a Boeing study of water injection will be discussed. The study used water injection as a means to reduce emissions and lower the turbine inlet temperature,  $T_{t4}$ , of a Boeing study engine with 1980's technology as well as current technology, 2000, Pratt and Whitney engine [68]. For the 1980's engine, very

similar in size and technology to the JT9D engine used for this analysis, the Boeing study expected a 46% increase in turbine life for a decrease of turbine inlet temperature of 120°R. From Figure 7.6, the 120°R decrease in  $T_{t4}$  would correspond to a de-rate of 11.3%. Using Pratt and Whitney data, for the same turbine inlet temperature change the Boeing study predicts a life improvement of 29% for the hot section of the engine. Assuming that 60% of the times the engine is removed from the airplane for maintenance are to repair the hot section of the engine, and the more conservative Pratt and Whitney life improvement estimate, the airplane operator should expect to save about \$22/hour/engine or a decrease in Cash Airplane Related Operating Cost (CAROC) of 1.2%. For the 747-200, the savings of de-rating the engines 11% should be between \$90 and \$200 per hour of aircraft operation and not just the departure segment. In comparison, the total fuel burn saved from start of roll to an altitude of 10,000 feet in this study is about 1,300 lbm. In 2006, that fuel would cost about \$300, and currently that it is likely near \$600. For the 747-200 at maximum takeoff weight, assuming a full-power takeoff is the fuel optimal departure, and considering only the costs of fuel and turbine maintenance, Table 7.6 presents the optimal engine de-rate as a function of flight length and fuel cost.

Flight Length (Block Hours)	2006 Optimal De-rate	2008 Optimal De-rate
2	7.8%	3.8%
4	15.1%	7.5%
6	22.6%	11.3%
8	>29%	15.1%

**Table 7.6: Estimated optimal de-rate for different aircraft flight lengths and fuel prices.**

For the 747-200 the average flight length is 7.2 block hours, so this simple analysis suggests the optimal de-rate for the engines is about 14% [65]. It is important to note that many important cost parameters such as takeoff field length, time to climb, and initial cruising altitude have been ignored. However, this preliminary analysis suggests that further work is

required to study departure trajectory optimization in the framework of an airline cost model to find benefits in terms of both engine life and reduced fuel consumption.

## Conclusion

The low-speed aerodynamics estimation tool developed in this work requires approximately fifteen seconds of run-time on a modern Pentium 4 computer and produces results with errors similar to current preliminary design tools used by aircraft manufacturers. The tool has similar methods to other preexisting low-speed aerodynamic tools, but it has a wider range of estimation capabilities and has been thoroughly validated. The validation work includes Boeing flight test results, NASA wind tunnel results, and an empirically tuned Lockheed method. The results of the method are such that clean-configuration drag polars generally have about one-percent error, high-lift drag polars have about three-percent error, lift curves have up to ten-percent error, and the maximum lift coefficient has generally less than five percent error.

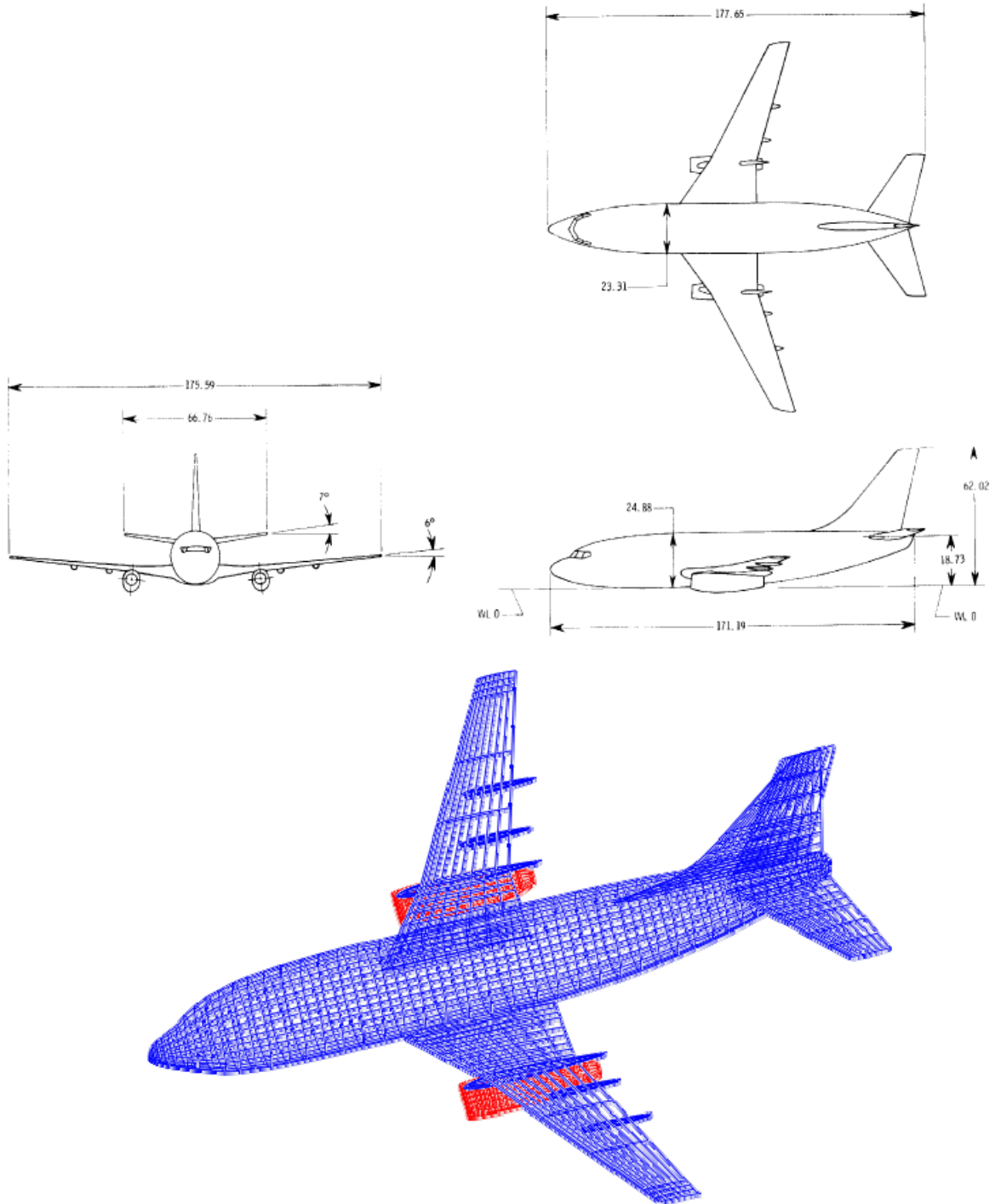
The low-speed aerodynamics estimation tool has been combined with an empirical airframe noise prediction tool, an engine cycle model, a trajectory simulator, and the Federal Aviation Administration's Integrated Noise Model to determine the influence of low-speed aerodynamics on airport community noise. For the tube and wing aircraft typical of the current transonic commercial fleet, the airport community noise is dominated by aircraft thrust and low-speed aerodynamics will only impact community noise in as much as is it determines the aircraft's height above the ground. For departure, engine noise dominates the airframe noise signature by over twenty EPNdB, and for arrival, the engine noise exceeds the airframe noise signature by three EPNdB. Accordingly, small variations in airframe configuration have a negligible impact on community noise; however, increased aerodynamic performance enables the aircraft to be at a higher altitude for a given amount of thrust or to use less thrust to achieve the same altitude. Atmospheric dissipation and thrust reduction are shown to be the most effective method for decreasing community noise. Using the FAA's noise certification procedure for arrival and departure small variations in aircraft configurations and operational procedures are studied to find aircraft noise reductions. For departure better climb performance is achieved by increasing aircraft aspect ratio and planform area, but the benefits are slight in that a ten-percent increase in either of these parameters only decreases the departure noise by two-tenths of a percent. For arrival, similarly small benefits are obtained by decreasing the flap deflection angle and delaying landing gear deployment; however, a considerable benefit of a

one-and-a-half percent noise reduction is gained by increasing the steepness of the approach path and increasing the approach velocity by ten-percent.

A final study parameterizes a departure trajectory for a Boeing 747-200 in terms of required pilot inputs and seeks to estimate the Pareto Frontier of trajectories in terms of minimum time to climb, minimum fuel consumption, and minimum community noise exposure. As general results, the minimum noise trajectory will have a higher flap setting, and a slower velocity, and will be above the minimum fuel burn or time to climb trajectories. The minimum fuel burn trajectory will have a velocity higher than the minimum noise trajectory but lower than the minimum time to climb. The trajectories and pilot inputs vary considerably with the aircraft takeoff weight; however, regardless of the takeoff weight substantial reductions in time to climb, fuel consumption, and noise exposure can be attained together. Compared to the standard departure for the 747-200 contained in the Integrated Noise Model, at maximum takeoff weight, time to climb can be reduced by two minutes, fuel burn reduced by 1,300 lbm, and 55 EPNdB noise exposure area reduced by 100 squares miles with a single procedure. This analysis shows that enabling airlines to depart from an airport with improved procedures can substantially reduce operating costs and noise impacts.

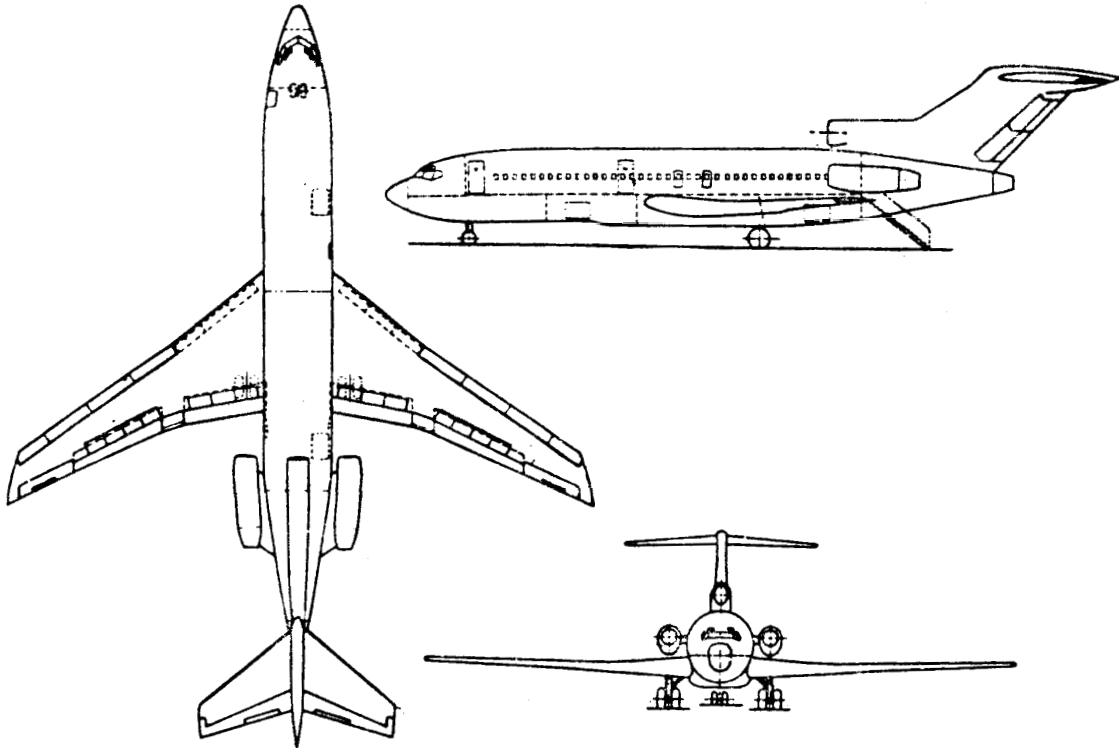
# Appendix A: Aircraft Geometries

## A.1. NASA TN D-5971 [19]



Dimensions are in centimeters.

A.2. Boeing 727-100 [62]



MODEL 727  
PRINCIPAL DIMENSIONS

WING

Area ..... 1560 Sq. Ft.  
 Span ..... 106 Ft.  
 Root Chord (Basic) . 246 In.  
 Tip Chord ..... 91.6 In.  
 Taper Ratio (Basic). 0.372  
 Incidence at Root .. +2°  
 Incidence at Tip ... +2°  
 Dihedral ..... 3°  
 Sweepback C/4 ..... 32°  
 Aspect Ratio ..... 7.2  
 M.A.C. .... 180.0 In.  
 Leading Edge MAC ... Sta. 860.2

FLAP

Leading Edge Area .. 54.8 Sq. Ft.  
 Trailing Edge Area  
 (Retracted) ... 280 Sq. Ft.  
 (Extended) .... 388 Sq. Ft.

AILERON

Inboard Area ..... 18.64 Sq. Ft.  
 Outboard Area ..... 36.5 Sq. Ft.

HORIZONTAL TAIL

Anhedral ..... 3°  
 Stabilizer Area ... 282.40 Sq. Ft.  
 Elevator Area ..... 94.14 Sq. Ft.  
 Span ..... 35 Ft. 9 In.

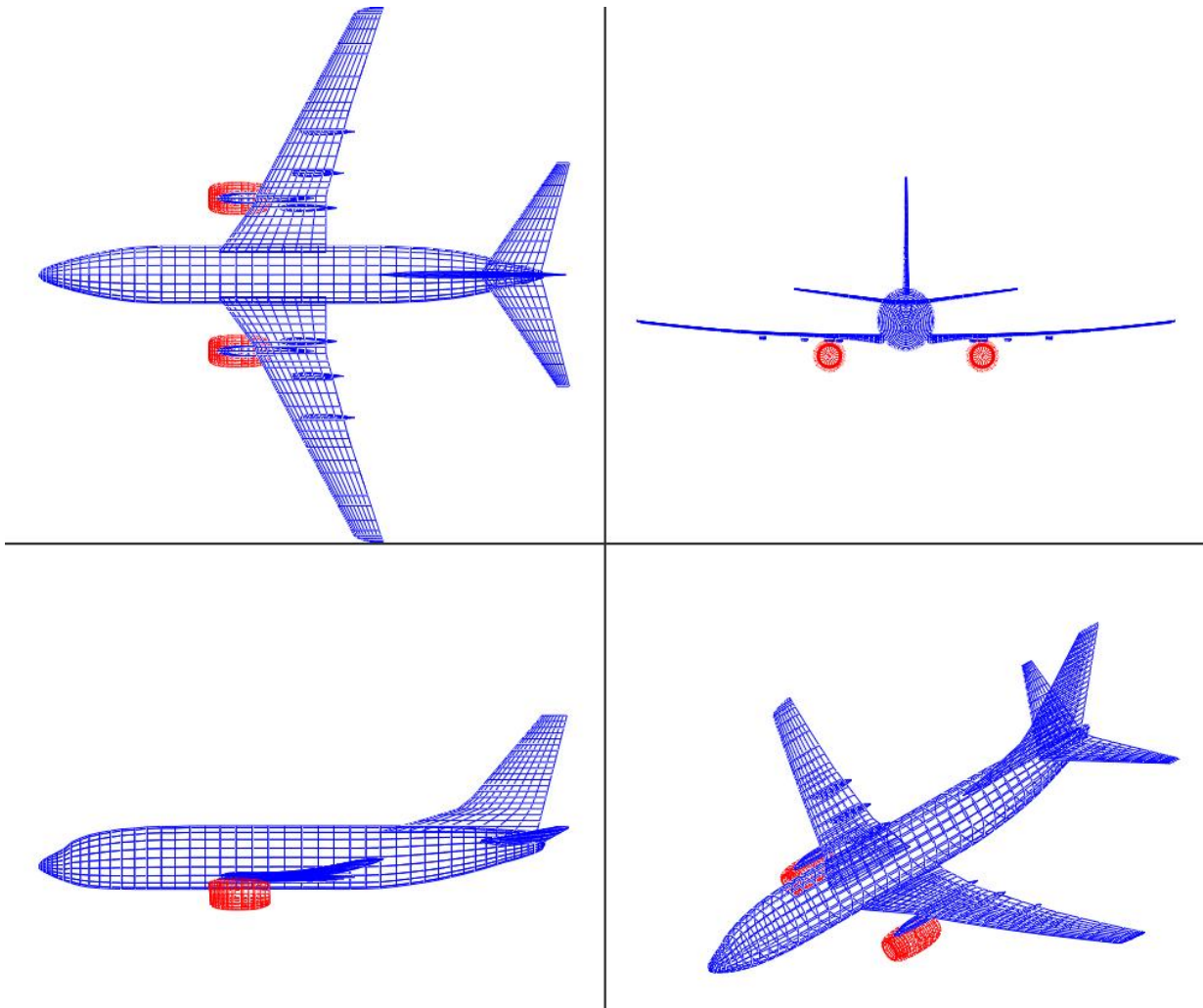
VERTICAL TAIL

Fin Area ..... 283.37 Sq. Ft.  
 Rudder Area ..... 72.63 Sq. Ft.

BODY

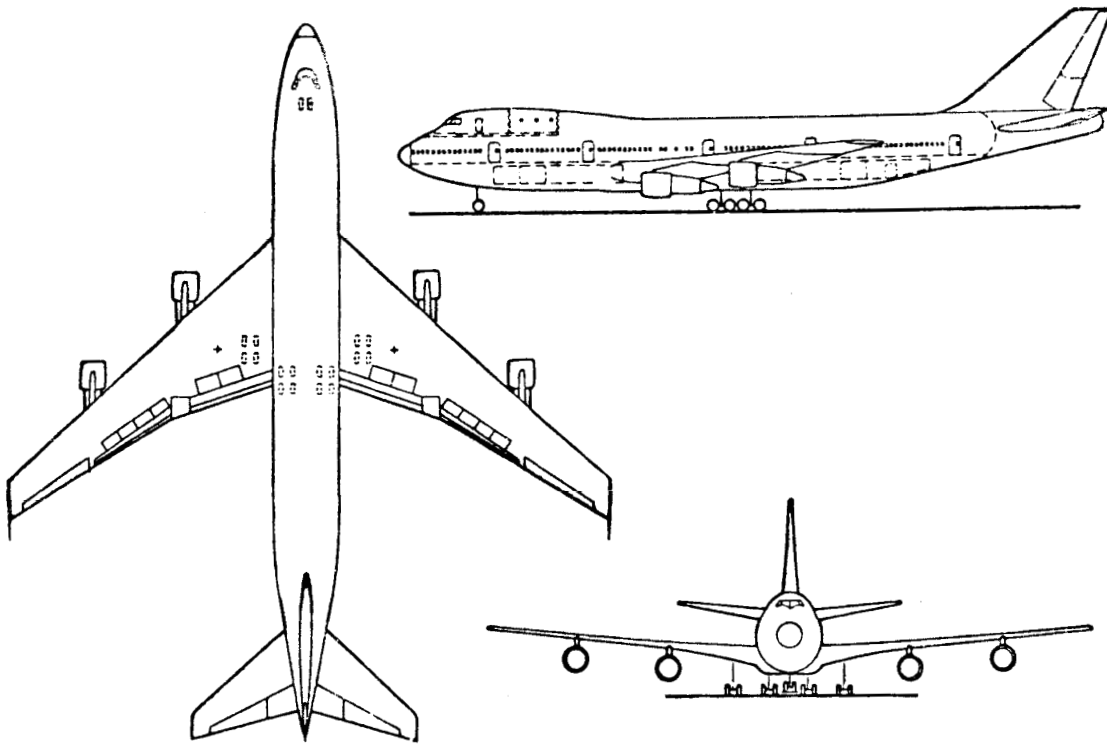
Length  
 Short Body(727-100)116 Ft. 2 In.  
 Long Body (727-200)136 Ft. 2 In.

### A.3. Boeing 737-700



Dimensions are from Boeing Commercial Aircraft and are proprietary.

**A.4. Boeing 747-100 [62]**



MODEL 747

PRINCIPAL DIMENSIONS

WING

Area . . . . .	5500 Sq. Ft.
Span . . . . .	195 Ft. 8 In.
Basic Root Chord . . . . .	449.68 In.
Reference Root Chord . . . . .	652.03 In.
Tip Chord . . . . .	160.00 In.
Taper Ratio . . . . .	.356 (Basic)
	.245 (Ref)
Incidence Root . . . . .	+2°
Incidence Tip . . . . .	+2°
Dihedral . . . . .	7°
Sweepback c/4 . . . . .	37.5°
Aspect Ratio (Ref) . . . . .	6.96
MAC (Basic only) . . . . .	327.78 In.
MAC c/4 Location (Sta) . . . . .	1339.91 In.

FLAP

Leading Edge Area (Retracted) . . . . .	448 Sq. Ft.
Trailing Edge Area (Retracted) . . . . .	847 Sq. Ft.

AILERON

Aileron Area (Inbd) . . . . .	71.8 Sq. Ft.
(Outbd) . . . . .	153.4 Sq. Ft.

HORIZONTAL TAIL

Area . . . . .	1470 Sq. Ft.
Sweepback c/4 . . . . .	37.5°
Span . . . . .	72 Ft. 9 In.
Root Chord . . . . .	32 Ft. 4 In.
Tip Chord . . . . .	8 Ft. 1 In.

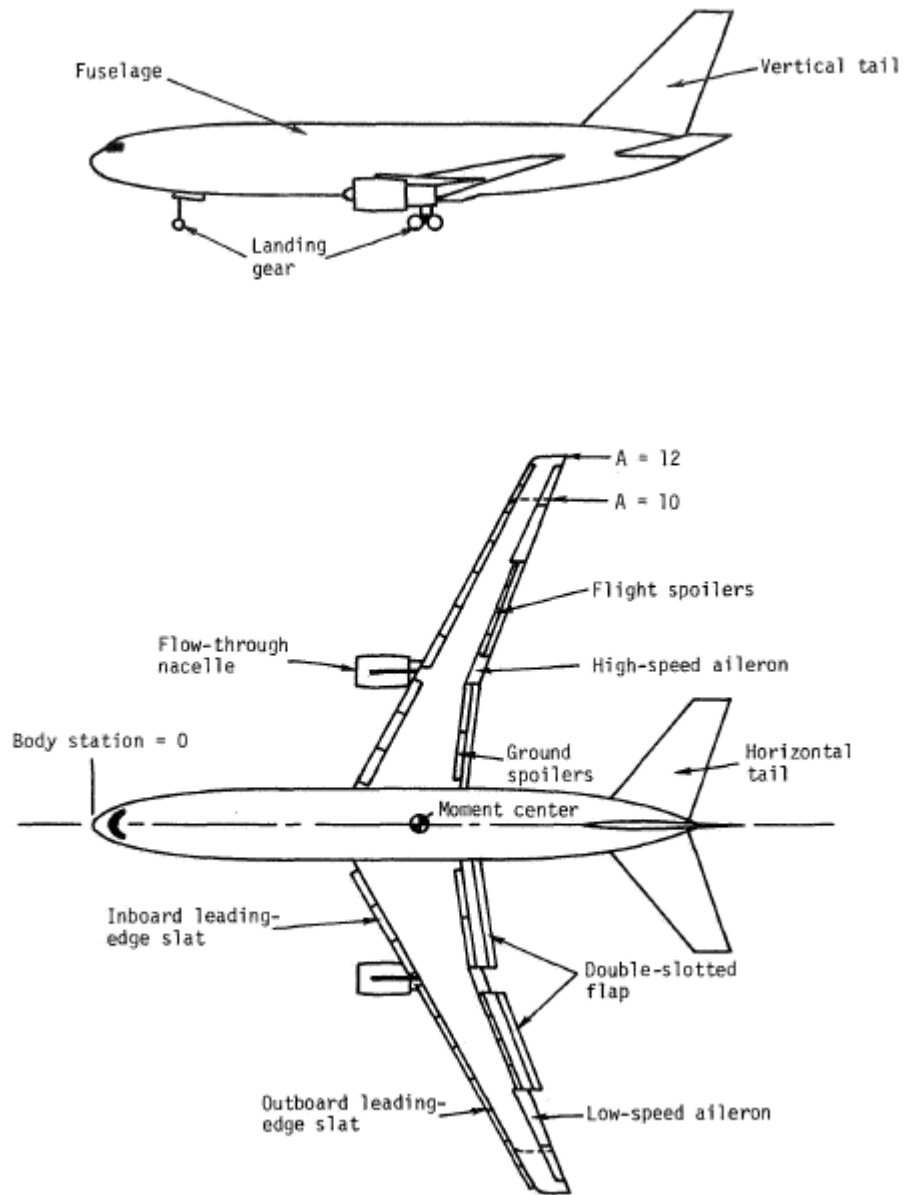
VERTICAL TAIL

Area . . . . .	830 Sq. Ft.
Sweepback c/4 . . . . .	45°
Span (Height) . . . . .	32 Ft. 3 In.
Root Chord . . . . .	38 Ft. 5 In.
Tip Chord . . . . .	13 Ft. 1 In.

BODY

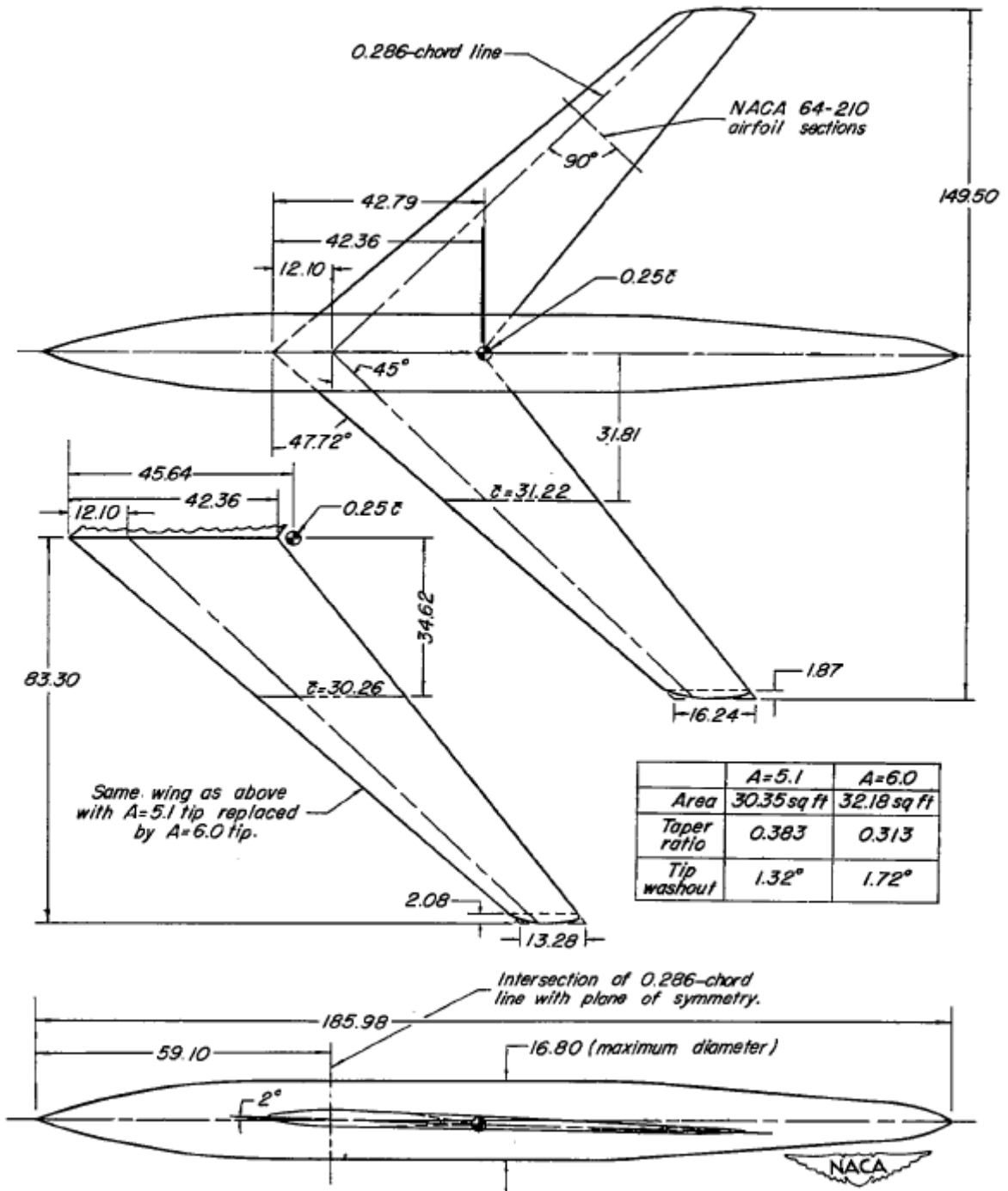
Length . . . . .	228 Ft. 6 In.
------------------	---------------

A.5. NASA TP 1580 [37]



(a) Configuration components.

A.6. NACA L50F20 [63]







## REFERENCES

- [1] Health Council of the Netherlands: Committee on the Health Impact of Large Airports. Public health impact of large airports. The Hague: Health Council of the Netherlands. September 2, 1999.
- [2] “Noise Exposure Comparisons.” NY/NJ/PHL Airspace Redesign Project, FAA. URL: [http://www.faa.gov/airports\\_airtraffic/air\\_traffic/nas\\_redesign/regional\\_guidance/eastern\\_reg/nyjphl\\_redesign/mitigation\\_displays/media/02\\_Noise%20Exposure%20Comparisons.pdf](http://www.faa.gov/airports_airtraffic/air_traffic/nas_redesign/regional_guidance/eastern_reg/nyjphl_redesign/mitigation_displays/media/02_Noise%20Exposure%20Comparisons.pdf), [accessed April 2008].
- [3] Waitz, Ian, et al. “Aviation and the Environment.” Massachusetts Institute of Technology, 2004.
- [4] Society of British Aerospace Companies, “Air Travel—Greener by Design; the Technology Challenge,” 2001, URL: [http://www.foresight.gov.uk/first\\_phase/1999-2002/dl/Defence\\_Aerospace\\_and\\_Systems/Reports/Air\\_Travel\\_Tech\\_Challenge/Air\\_Travel\\_Tech\\_Challenge\\_Aug\\_2001.pdf](http://www.foresight.gov.uk/first_phase/1999-2002/dl/Defence_Aerospace_and_Systems/Reports/Air_Travel_Tech_Challenge/Air_Travel_Tech_Challenge_Aug_2001.pdf), [accessed April 2008]
- [5] Antoine, Kroo, Willcox and Barter. “A Framework for Aircraft Conceptual Design and Environmental Performance Studies.” AIAA 2004-4314, August 30, 2004.
- [6] Spindler, Philip, Michael. “Environmental Design Space Model Assessment.” Massachusetts Institute of Technology, May 2007.
- [7] Feagin, Richard and Morrison, William. “Delta Method, An Empirical Drag Buildup Technique.” Lockheed, NASA CR-151971, 1978.
- [8] Paterson, J., H., et al. “A Survey of Drag Prediction Techniques Applicable to Subsonic and Transonic Aircraft Design.” AGARD CP-124, April 1973, pg 1.1-1.37.
- [9] Torenbeek, Egbert. Synthesis of Subsonic Airplane Design. Kluwer Academic Publishers, Dordrecht: 1982.
- [10] Schauffele, Roger, D. The Elements of Aircraft Preliminary Design. Aries Publications: Santa Ana, 2000.
- [11] Hileman, Spakovszky, Drela and Sargeant. “Airframe Design for ‘Silent Aircraft’” 45<sup>th</sup> AIAA Aerospace Sciences Meeting and Exhibit, January 8-11, 2007, Reno, AIAA 2007-453.
- [12] Crichton, de la Rosa Blanco, Law and Hileman. “Design and Operation for Ultra Low Noise Take-off.” 45<sup>th</sup> AIAA Aerospace Sciences Meeting and Exhibit, January 8-11, 2007, Reno, AIAA 2007-456.

- [13] Hileman, Reynolds, de la Rosa Blanco, Law, and Thomas. "Development of Approach Procedures for Silent Aircraft." 45<sup>th</sup> AIAA Aerospace Sciences Meeting and Exhibit, January 8-11, 2007, Reno, AIAA 2007-451.
- [14] Clarke, John-Paul Barrington. "A System Analysis Methodology for Developing Single Event Noise Abatement Procedures." Massachusetts Institute of Technology, February 1997.
- [15] Wijnen, R.A.A. and Visser, H.G., 2003. "Optimal Departure Trajectories with Respect to Sleep Disturbance." *Aerospace Science and Technology* 7, 81-91.
- [16] Visser, H.G. "Generic and site-specific criteria in the Optimization of Noise Abatement Trajectories." Proceedings of Eleventh Australian International Aerospace Congress, Melbourne, 2005.
- [17] Kroo, Ilan. "Aircraft Design: Synthesis and Analysis" Desktop Aeronautics, Stanford: 2006, URL: <http://adg.stanford.edu/aa241/AircraftDesign.html>, [accessed April 2008].
- [18] Mason, W.,H.. "FRICTMan." Virginia Tech, 1998, URL: [http://www.aoe.vt.edu/~mason/Mason\\_f/FRICTman.pdf](http://www.aoe.vt.edu/~mason/Mason_f/FRICTman.pdf), [accessed October 2007].
- [19] Capone, Francis, J.. "Longitudinal Aerodynamic Characteristics of a Twin-Turbofan Subsonic Transport with Nacelles Mounted Under the Wings." NASA TN D-5971, October 1970.
- [20] Shevell, Richard, S.. Fundamentals of Flight. Prentice Hall: Upper Saddle River, 1989. Pg 177-185.
- [21] Drela, Mark and Youngren, Harold. "AVL 3.26 User Primer." April 2006, URL: [http://web.mit.edu/drela/Public/web/avl/avl\\_doc.txt](http://web.mit.edu/drela/Public/web/avl/avl_doc.txt), [accessed October 2007].
- [22] "Excrescence Drag Levels on Aircraft." ESDU, 94044, April 2006.
- [23] Tinoco, E., N., and Chen, A., W., "Transonic CFD Applications to Engine/Airframe Integration." Boeing Commercial Airplane Company, AIAA-84-0381, 1984.
- [24] Berry, Dennis, L. "The Boeing 777 Engine/Aircraft Integration Aerodynamic Design Process." ICAS-94-6.4.4, September 1994, pg. 1305-1320.
- [25] Liebeck, Robert, H. Personal Communication.
- [26] Hoerner, S.,F.. Fluid Dynamic Drag. Hoerner Fluid Dynamics: Bakersfield, 1965. Pg 13-16.
- [27] "Drag Increment Due to Rear Fuselage Upsweep." ESDU, 80006, April 2006.

- [28] “Vortex Drag Coefficient of Wing with Part-Span Flap and Central Cut-Out.” ESDU FLAPS 02.01.08, May 1999.
- [29] “Fuselage Interference Effects on Flap Characteristics.” ESDU 97003, March 1997.
- [30] “Conversion Factor for Profile Drag Increment for Part-Span Flaps.” ESDU Flaps 02.01.07, February 1993.
- [31] “Increments in Aerofoil Lift Coefficient at Zero Angle of Attack and in Maximum Lift Coefficient Due to Deployment of Various Leading-Edge High-Lift Devices at Low Speeds.” ESDU 94027, December 1994.
- [32] “Increments in Aerofoil Lift Coefficient at Zero Angle of Attack and in Maximum Lift Coefficient Due to Deployment of a Plain Trailing-Edge Flap, with or without a Leading-Edge High Lift Device, at Low Speeds.” ESDU 94028, December 1994.
- [33] “Increments in Aerofoil lift Coefficient at Zero Angle of Attack and in Maximum Lift Coefficient Due to Deployment of a Trailing-Edge Split Flap, with or without a Leading-Edge High-Lift Device, at low Speeds.” ESDU 94029, December 1994.
- [34] “Increments in Aerofoil lift Coefficient at Zero Angle of Attack and in Maximum Lift Coefficient Due to Deployment of a Single-Slotted Trailing-Edge Flap, with or without a Leading-Edge High-Lift Device, at low Speeds.” ESDU 94030, April 1995.
- [35] “Increments in Aerofoil lift Coefficient at Zero Angle of Attack and in Maximum Lift Coefficient Due to Deployment of a Double-Slotted or Triple-Slotted Trailing-Edge Flap, with or without a Leading-Edge High-Lift Device, at low Speeds.” ESDU 94031, April 1995.
- [36] “Undercarriage Drag Prediction Methods.” ESDU 79015, March 1987.
- [37] Morgan, Harry, L. Jr. et al. “Low-Speed Aerodynamic Performance of a High-Aspect Ratio Supercritical-Wing Transport Model Equipped With Full-Span Slat and Part-Span Double-Slotted Flaps.” NASA TP 1580, December 1979.
- [38] Davis, Robert A. “Technology in Commercial Airplane Design.” Global Air & Space Conference, Arlington: May 1995.
- [39] “Maximum Lift of Wings with Trailing-Edge Flaps at Low Speeds.” ESDU 91014, August 1995.
- [40] “Maximum Lift of Wings with Leading-Edge Devices and Trailing-Edge Flaps deployed.” ESDU 92031, November 1995.
- [41] “Lift Curve of Wings with High-Lift Devices Deployed at Low Speeds.” ESDU 96003, November 2003.

- [42] “Statistical Loads Data for the Boeing 777-200ER Aircraft in Commercial Operations.” DOT/FAA/AR-06/11, November 2006.
- [43] “Statistical Loads Data for the Boeing 737-400 Aircraft in Commercial Operations.” DOT/FAA/AR-98/28, August 1998.
- [44] United States Code of Federal Regulations, Title 14, part 25, §25.105-§25.119.
- [45] Olmstead, Jeffrey R. et al. “Integrated Noise Model (INM) Version 6.0 Technical Manual. FAA-AEE-02-01, January 2002.
- [46] Corning, Gerald. Subsonic and Supersonic, CTOL and VTOL Airplane Design. University of Maryland, College Park: 1974.
- [47] “777-200 Operations Manual” D632W001-TBC revision 2, The Boeing Company, September 1, 1994.
- [48] NTSB: LAX90LA122, December 14, 1992.
- [49] Yager, Thomas J. “Boeing 737 Aircraft Test Results from 1996 Joint Winter Runway Friction Measurement Program.” NASA TM 110482, IMAPCR '96, October 22-23, 1996.
- [50] Palladino, Joseph. Personal Communication.
- [51] “777-200/300 Airplane Characteristics for Airport Planning.” D6-58329, Boeing Commercial Airplanes, October 2004.
- [52] “747 Airplane Characteristics for Airport Planning.” D6-58326, Boeing Commercial Airplane Company, May 1984.
- [53] “Procedure for the calculation of Airplane Noise in the Vicinity of Airports.” SAE AIR 1845, March 1986.
- [54] Kerrebrock, Jack L. Aircraft Engines and Gas Turbines 2<sup>nd</sup> ed. The MIT Press, Cambridge: 1992.
- [55] Khorrami, Mehdi R. “Unsteady Flow Computations of a Slat with a Blunt Trailing Edge.” AIAA Journal Vol. 38, No. 11, November 2000.
- [56] Fink, Markin R. “Airframe Noise Prediction Method.” FAA-RD-77-29, March 1977.
- [57] Zorumski, William, E. “Aircraft Noise Prediction Program Theoretical Manual.” NASA TM 83199, February 1982.

- [58] Hubbard, Harvey, H. "Aeroacoustics of Flight Vehicles: Theory and Practice." NASA RP 1258, August 1991.
- [59] "Airframe Noise Prediction" ESDU 90023, June 2003.
- [60] United States Code of Federal Regulations, Title 14, part 36 Appendices A and B, §A36.1-§B36.8.
- [61] "Noise Levels for U.S. Certificated and Foreign Aircraft." AC36-1H, United States Department of Transportation, Federal Aviation Administration, November 15, 2001.
- [62] The Boeing Company. Jet Transport Performance Methods. The Boeing Company: Seattle, D6-1420, May 1969. Pg 0.15-0.17.
- [63] Salmi, Reino. J. "Effects of Leading-Edge Devices and Trailing Edge Flaps on Longitudinal Characteristics of Two 47.7° Sweptback Wings of Aspect Ratios 5.1 and 6.0 at a Reynolds Number of  $6.0 \times 10^6$ ." Langley Air Force Base, NACA RM L50F20, 1950.
- [64] Fischel, Jack, and Schneiter, Leslie. E.. "An Investigation at Low Speed of a 51.3° Sweptback Semispan Wing Equipped with a 16.7-Percent-Chord Plain Flaps and Ailerons Having Various Spans and Three Trailing Edge Angles." Langley Field, NACA RM L8H20, 1946.
- [65] "Aircraft Operating Costs and Statistics." Aviation Daily, June 26, 2006.
- [66] Aircraft Engine Emissions Database. April 2008. URL: <http://www.caa.co.uk/default.aspx?catid=702&pagetype=90>, [accessed, May 2008].
- [67] Martini, Bastien. Personal Communication.
- [68] Daggett, David L. "Water Injection Feasibility for Boeing 747 Aircraft" NASA CR 2005-213656, December 2005.